5-2018

APPLICATIONS IN VIBROARTHROGRAPHY: ASSESSMENTS OF INSTABILITY IN TOTAL HIP ARTHROPLASTY, CAM-POST ENGAGEMENT IN TOTAL KNEE ARTHROPLASTY, AND VISCOSUPPLEMENTATION IN OSTEOARTHRITIC KNEES

Trevor Ferdinand Grieco
University of Tennessee, tgrieco@vols.utk.edu

Recommended Citation

Grieco, Trevor Ferdinand, "APPLICATIONS IN VIBROARTHROGRAPHY: ASSESSMENTS OF INSTABILITY IN TOTAL HIP ARTHROPLASTY, CAM-POST ENGAGEMENT IN TOTAL KNEE ARTHROPLASTY, AND VISCOSUPPLEMENTATION IN OSTEOARTHRITIC KNEES. " PhD diss., University of Tennessee, 2018.
https://trace.tennessee.edu/utk_graddiss/4960

To the Graduate Council:

I am submitting herewith a dissertation written by Trevor Ferdinand Grieco entitled "APPLICATIONS IN VIBROARTHROGRAPHY: ASSESSMENTS OF INSTABILITY IN TOTAL HIP ARTHROPLASTY, CAM-POST ENGAGEMENT IN TOTAL KNEE ARTHROPLASTY, AND VISCOSUPPLEMENTATION IN OSTEOARTHRITIC KNEES." I have examined the final electronic copy of this dissertation for form and content and recommend that it be accepted in partial fulfillment of the requirements for the degree of Doctor of Philosophy, with a major in Mechanical Engineering.

Richard D. Komistek, Major Professor

We have read this dissertation and recommend its acceptance:

William R. Hamel, Mohamed R. Mahfouz, Harry L. Martin, Adrija Sharma

Accepted for the Council:
Dixie L. Thompson

Vice Provost and Dean of the Graduate School

(Original signatures are on file with official student records.)

APPLICATIONS IN VIBROARTHROGRAPHY: ASSESSMENTS OF INSTABILITY IN TOTAL HIP ARTHROPLASTY, CAM-POST ENGAGEMENT IN TOTAL KNEE ARTHROPLASTY, AND VISCOSUPPLEMENTATION IN OSTEOARTHRITIC KNEES

A Dissertation Presented for the

Doctor of Philosophy Degree

The University of Tennessee, Knoxville

Trevor Ferdinand Grieco

May 2018

DEDICATION

This dissertation is dedicated to my grandfather, my parents, my brothers, and Ashley.

Grandpa, I always told you I was going to be a doctor. Although this is not what either of us had in mind, I was constantly reminded of the fact that I was going to achieve for you. Everyone always tells me that I have a lot of you in me. It honestly means more than they can imagine. I hope this work would have made you proud. I miss you.

Mom and Dad, I do not even know where to start. The last two years spent living with you while working on this research were incredibly special to me. The convenience of being back home was so good for me, and I am willing to bet that for those two years I ate better than any grad student in history. Living with you as an adult truly made me appreciate how fortunate I was to have parents like you. Thank you for raising me with discipline and love and thank you for sacrificing more than I can imagine to provide our family the life we know. You have enabled me to become the man I am today, and in this moment of reflection, I am and will forever be unexplainably grateful.

To my brothers, I just want to start by saying thanks for putting up with me. I know I was an instigator growing up and it is a wonder you still even talk to me. Thank you for competing with me, thank you for fighting with me, and thank you for loving me. I cherish our countless experiences together and consider our brotherhood to be among the world’s most invaluable treasures. You are all remarkable men that I am proud to call my brothers.

Lastly, I dedicate this to Ashley. Through years of a long-distance relationship you never wavered. Your support in this endeavor was critical to its completion, and your love was and remains the most incredible pillar for me to rest my burdens on. Thank you for patiently waiting for this time. I am so excited to be closing the door on this chapter of our life. What we have started and continue to build, is the strongest relationship I have with anybody in the world. You are more than I deserve, and I consider myself genuinely blessed to embark on this life-long journey together.

ACKNOWLEDGEMENTS

Thank you, Dr. Richard Komistek, for enabling this graduate research experience. My education is priceless, and I am grateful to you for providing me the opportunity to pursue this doctoral degree. Thank you for your support and guidance in this research, without which it would not have been possible. Also thank you for being incredibly persuasive and deterring me from quitting on this. It personally means a great deal to me, and reflecting here at the end of it, I know that I would have regretted such a decision for the rest of my life.

Thank you Dr. Adrija Sharma, for developing me as an engineer and scientist. On a daily basis you pushed me to be better and to truly take pride in my work. Your mentorship has heightened my attention to detail and raised the overall quality of everything I do. Thank you for impacting my professional career so strongly.

Thank you, Dr. William Hamel, for exposing me to robotics and for providing me the opportunity to learn firsthand about human-robotic interactions.

Thank you, Dr. Lee Martin, for the entrepreneurial lessons and the commercial insight of academically rooted innovations.

Thank you, Dr. Ray Wasielewski, for providing the clinical perspective in review of this research that was required to ensure its quality and relevance. Also thank you for the opportunity to research vibrations on your osteoarthritic patients.

Thank you, Dr. Mohamed Mahfouz, for your expert knowledge in instrumentation, signals processing, and medical product development.

Thank you, Dr. Douglas Dennis, for giving me the opportunity to research vibrations on your total knee arthroplasty patients.

Thank you, Dr. Mazen Al-Hajjar and Professor John Fisher, for giving me the opportunity to research vibrations on the total hip simulator at the University of Leeds.

Thank you, Dr. Phillip Nobel, for providing me with an increased perspective in the field of orthopaedics and for advising me in multiple research endeavors.

Thank you, Dr. Henry Rocco for participating in the viscosupplementation research. Your kindness and generosity was tremendous, and I truly enjoyed spending time with you during my visits to Columbus. Thank you for the wisdom, stories, and memories that I will have forever.

Thank you, Rebecca Robertson, for helping me execute these investigations. I could have never launched these properly without your administrative expertise.

Lastly, I would like to thank my co-workers Sumesh Zingde, Matt Anderle, Brad Meccia, Ian Zeller, Michael LaCour, Duc-Manh Ta, Milad Khasian, Garett Dessinger, Jarrod Nachtrab, Lauren Crothers, Daniel Nalepa, Madison Kirk, Leyton Adams, Jan Brukbauer, Matthew Young, William Anderson, Logan McNeil, and Josh Penny for engineering and researching alongside me. I wish you all good luck in your future endeavors.

ABSTRACT

Measurement of joint sounds and vibrations for non-invasive orthopaedic diagnostic purposes has slowly advanced since the 1960s. Most work has been focused in the development of methods for screening of abnormal knees. To date the technique has not gained clinical traction as is it fraught with various obstacles and skepticism. This doctoral thesis is neither an argument in favor of nor against the clinical use of vibroarthrography for musculoskeletal diagnostics in humans, but rather an exploration of its potential in cases of orthopaedic interest. These areas include 1) instability in total hip arthroplasty, 2) cam-post engagement in posterior stabilized total knee arthroplasty, and 3) viscosupplementation in osteoarthritic knees. It was expected that each of these unique cases would be characterized by dynamic phenomena that could be measured in the form of surface vibrations at the skin.

Methods previously presented in various vibroarthrography research were adopted, modified, and expounded upon to best suit the needs of each experiment. In a mechanical hip simulator, it was found that vibroarthrography could be effectively used to distinguish the difference between 1 mm and 2 mm of hip separation. In posterior stabilized total knee arthroplasty subjects, it was found that multiple vibroarthrographic features may be used to approximate the occurrence of cam-post engagement, and that vibrations measured at the joint surface may be correlated to cam-post engagement velocity. In osteoarthritic knees, the relationship between clinical evidence, viscosupplementation, and vibroarthrography varied on a case by case basis.

To the knowledge of the author, all three of these experiments are the first of their kind. Ultimately, the methods and results presented within provide new foundations for vibroarthrography that may be used to further explore the clinical potential of this noninvasive diagnostic.

PREFACE

The skeletal system presents engineers with unique opportunities to advance technology. In the field of imaging X-ray, computed tomography (CT), ultrasound, and magnetic resonance imaging (MRI) techniques have enabled medical professionals to analyze the human body with unimaginable detail. Such innovations have increased diagnostic accuracies, improved treatment plans, and enhanced education leading to improved clinical outcomes. Unfortunately, these technologies can be expensive and may be associated with risks, (radiation exposure from X-ray and CT), thus its use may not be warranted if symptoms are tolerable. Furthermore, some of these techniques are limited in their assessment of soft tissue damage. These factors amongst others can lead to late detection of orthopaedic disease or trauma which is more effectively treated if detected early. In addition, repeated image-based assessment during recovery from orthopaedic trauma is minimized due to costs, convenience, and exposure. Thus, a gap in diagnostics and monitoring exists which is well suited for a fast, noninvasive, affordable, and reliable technology capable of assessing joint health.

Healthy synovial joints (most common type of joint in the human body) are mechanically ideal. The combination of joint fluid (synovial fluid) viscosity and bearing surface (articular cartilage) material properties creates a nearly frictionless environment in synovial joints that can be mechanically described as gliding, hinge, pivot, ellipsoidal, saddle, ball-and-socket and/or compound type joints. In an arthritic joint both the fluid and the bearing surface are compromised. Decreases in synovial fluid viscosity, cartilage degeneration, and abnormal bone remodeling are all associated with this disease. Like all mechanical systems, when damaged and/or functioning improperly, it can be assumed that a joint will emit distinctly different mechanical vibrations than when completely intact and functioning properly. With the appropriate sensor, these vibrations can be measured at the skin surface and used for assessment of joint health.

Vibroarthrography has often been used to denote the process of inspecting joint vibrations. The objective of the research presented here is to explore new applications of vibroarthrography at the knee and hip. These include:

1. An in vitro investigation of instability in a total hip arthroplasty
2. An in vivo investigation of cam-post engagement in posterior-stabilized total knee arthroplasty
3. An in vivo investigation of viscosupplementation in osteoarthritic knees

TABLE OF CONTENTS

LIST OF TABLES

LIST OF FIGURES

ACRONYMS

2D two-dimensional

3D three-dimensional

AI analogue input

AP anterior-posterior

CAD computer-aided design

CMR Center for Musculoskeletal Research

CoC ceramic-on-ceramic

CoP ceramic-on-polyethylene

CPR contact patch to rim

DAQ data acquisition

DKB deep knee bend

DWT discrete wavelet transform

EAA envelope amplitude average

EHL elastohydrodynamic lubrication

FF form factor

HA hyaluronic acid

IDWT inverse discrete wavelet transform

IEPE integrated electronic piezoelectric

GND ground terminal

LVDT linear variable differential transducer

ML medial-lateral

MoM metal-on-metal

MoP metal-on-polyethylene

MRI magnetic resonance imaging

NSAIDS nonsteroidal anti-inflammatory drugs

OA osteoarthritis

PAPR peak-to-average power ratio

PCL posterior cruciate ligament

PiP picture-in-picture

PT pelvic tilt

PS posterior-stabilized

RMS root mean squared

SI superior-inferior

TC-AT turns count adaptive threshold

TC-FT turns count fixed threshold

THA total hip arthroplasty

TKA total knee arthroplasty

VMS variance of means squared

CHAPTER 1. BACKGROUND AND INTRODUCTION

1.1. Vibroarthrography

The investigation of joint sounds dates to the 17th century when Robert Hooke suggested joint noise could be used for diagnostic purposes. Early investigations utilized stethoscopes, contact microphones, and cardiophones to listen to joint sounds. While this technology was capable of measuring joint sounds, it was recognized that signals of interest were surrounded by extrinsic nonstationary noise such as snapping tendons and hand tremor associated with holding the acoustic instrument [1]. Chu and his research group from the University of Akron, Ohio was the first to reduce unwanted noise by utilizing a double microphone assembly and a differential amplifier arrangement at the knee joint [1]. In a series of investigations, they reported signals could be classified into rheumatoid arthritis, degenerative arthritis, and chondromalacia patella [2]. Furthermore, they demonstrated that the peak magnitude of the frequency spectrum and signal power was correlated with the severity of cartilage damage [1, 2].

In the late 1970s Mollan and his research group inspected the efficacy of recording joint surface vibrations with piezoelectric accelerometers, and concluded that these accelerometers were superior to acoustic sensors available at that time because of their frequency response and small size as well as the fact that these sensors were unaffected by sources of background noise that plagued acoustic sensors (Figure 1.1) [3]. They demonstrated that the major frequency components of a pathological knee were less than 100 Hz [4]. It was also determined that activity speed affected the peak acceleration and root mean squared (RMS) vibration, but not the peak frequency [5]. Most importantly they found that meniscal injuries produced unique signals, and that arthroscopic repair of these injuries resulted in a significant reduction of signal strength [6]. The same group of researchers expanded the role of their vibration system to neonatal screening of hips [7]. In a longitudinal investigation they demonstrated that vibroarthrography

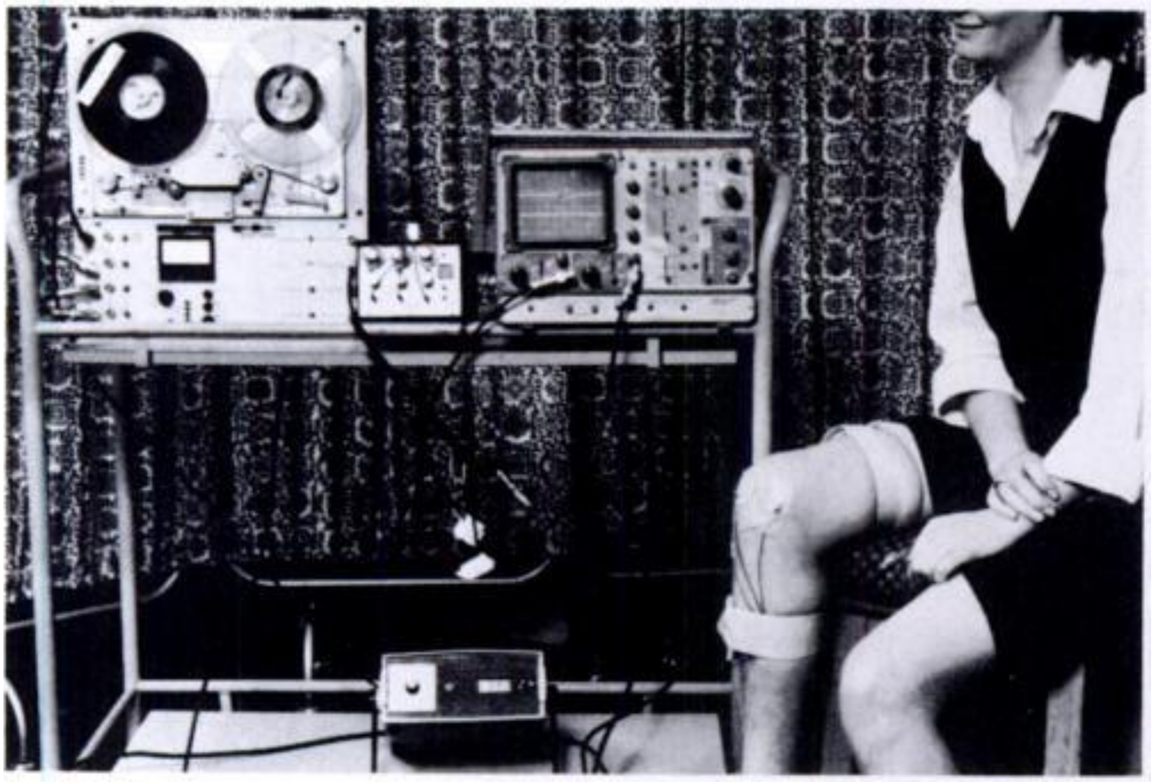

Figure 1.1. Vibration arthrography data collection by McCoy et al. in 1987 (Mollan research group) [6].

(interpretation of vibrations or sound signals emitted from a joint) could be used to provide information on the presence of developmental hip dysplasia otherwise not available to physicians, and that such a system could be implemented at little cost [7, 8]. Ultimately it appears that screening for developmental hip dysplasia has been left to physical examination followed by ultrasound inspection if deemed appropriate [9-11].

Rangayyan and his research institute at the University of Calgary further advanced the use of vibroarthrography at the knee through rigorous investigations of signal processing and pattern classification [12-29]. This group has made progress in adaptive cancellation of muscle interference [16], localization of the sound source and pathology [17], auditory mapping and display of signals [24], and parametric representation and screening of signals [18-20, 23, 25]. Using model parameters from least-squares models (autoregressive, all-pole, or linear prediction) as discriminant features in a set of 90 knee signals comprised of 51 normal knees and 39 pathological knees, the best normal-versus-abnormal classification accuracy was 75.6% [18-20]. More recently, wavelet decomposition and a modified local discriminant bases algorithm applied to 89 knee signals achieved a classification accuracy of 79.8% [25]. Using statistical parameters and radial-basis functions, classification accuracy of the same 89 signals was increased to 82% [26]. This last finding was important in demonstrating that simple signal statistics and a sophisticated classifier could be used in lieu of previously established classification techniques that required signal segmentation and knee flexion angle information. Investigation of novel signal processing and classification techniques by Rangayyan and his colleagues remains ongoing. This group’s contribution to vibroarthrography is unparalleled, and their detailed methods provide solid foundations for novel applications in vibroarthrography.

Reddy et al. also used accelerometers at the knee to characterize vibrations unique to osteoarthritis patients, rheumatoid patients, chondromalacia patients and normal subjects [30]. An additional investigation showed the accelerometer system was effective in distinguishing spondyloarthropathy (subset of arthritis) subjects from rheumatoid subjects [31]. The detected differences were based on a power spectral analysis of the average vibration signal power over a 100-500 Hz range.

In a novel series of experiments, Kawchuk's group at the University of Alberta, took a structural health monitoring approach [32-35]. Starting in porcine cadavers, they fixed triaxial accelerometers directly to the vertebrae and stimulated the joints with an electromechanical shaker [32, 33]. Experiments included analysis of intact vertebrae, fused vertebrae, and damaged vertebral discs (disc stab, ½ transection, and full transection). Differences in structural response as measured by the accelerometers were classified using a neural network. Success in classifying the damage led towards similar studies in human cadavers [34]. These investigations confirmed that uniaxial accelerometers mounted to the skin was adequate for collecting the desired data. Additionally, they demonstrated that signals exhibited high repeatability within an original placement, however, following removal and replacement of a sensor, signals changed significantly [34]. Recently this structural health monitoring technique was implemented on 10 pairs of identical twins to test its ability in detecting structural alterations in the spines of living human subjects (Figure 1.2) [35]. Significant differences in vibration signals agreed with structural differences reported by a blinded radiologist that utilized magnetic resonance imaging (MRI) to assess the twins' anatomy. Specifically, the peak frequency was significantly different in twins that were reported to be structurally discordant. None of the measured vibration features (peak frequency, area under the curve, and the

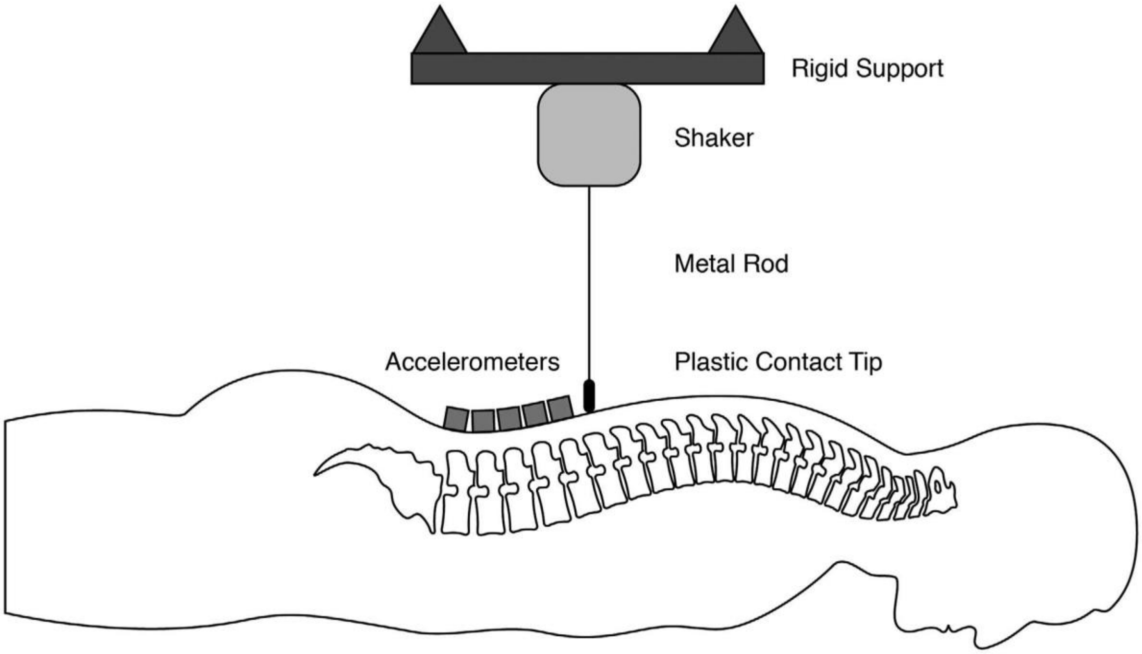

Figure 1.2. Structural health monitoring diagram illustrates the research methods described by Kawchuck et al. for the analysis of twin lumbar spines [35].

root mean square) were significantly different in concordant twins [35]. Additional research by this group is ongoing.

Synchronization of vibrations with fluoroscopically derived kinematics has been investigated previously at the Center for Musculoskeletal Research (CMR) at the University of Tennessee. Glaser et al. conducted an initial in vivo investigation on the correlation between sound and hip separation in different bearing surfaces of total hip arthroplasty (THA) [36]. This investigation utilized a single sound transducer at the hip and included 24 THA subjects. Within this sample of subjects, existed six different bearing types. It was reported that a knocking sound was observed when the femoral head contacted the acetabulum in all patients that experienced separation. In her doctoral thesis, Glaser established methods for correlating sound and vibration with fluoroscopically derived kinematics and concluded additional research was required to more thoroughly understand the correlation between hip joint sounds and potentially detrimental kinematic patterns [37]. More recently, Zingde conducted an initial investigation of vibration data as it related to cam-post engagement in posterior-stabilized total knee arthroplasty (TKA) [38]. It was suggested in this work that vibroarthrography could be used to determine the mechanics of cam-post engagement such that lower vibration content implied a smooth transition during initial contact, and that the presence of a significant impulse in a vibroarthrogram implied an irregular transition during initial contact [38].

Additional vibroarthrography research conducted at CMR consists of a classifier developed to screen for arthritic degeneration in the patellofemoral and the tibiofemoral compartments of the knee [38, 39]. This research utilized a control group of 23 healthy subjects and an investigational group of 52 arthritic subjects scheduled to have a primary total knee replacement. Two triaxial accelerometers were used to record vibrations at the knee. The accelerometers were positioned on the patella, the tibial tuberosity, and the medial femoral epicondyle. Subjects performed weight bearing and non-weight bearing maneuvers including a deep knee bend, chair rise, stair climb, stair descent, gait, and passive leg swings. A minimum-error-rate classifier was conditioned to achieve the highest accuracy in screening subjects into the appropriate groups (healthy or diseased). Numerous features were derived from each subject's vibroarthrograms to be used in the classifier. These included the mean, median, variance, skewness, kurtosis, 90th, 95th, 97th, and 99th quantiles, envelope integral, and the product of the envelope integral with the duration of the activity. All combinations of these features were tested to optimize the discriminant function. The highest classification rate reported was 96.1% [39]. This rate was achieved with 9 different sets of four features. The envelope integral and/or the product of the envelope integral with the duration of the activity was present in all of these sets [39]. In conjunction with this investigation, a methodology was presented to specify the compartmental location(s) and to grade the severity of the lesion(s) [38, 39]. Intraoperative inspection at the time of joint replacement was used to confirm the location and severity of disease. This clinical assessment served as the control to which vibroarthrograms were cross-referenced. Although it was suggested that vibroarthrography could be used to triangulate location and judge the severity of lesions in select cases, additional evidence is required for this diagnostic capability to be considered accurate and reliable.

1.2. Objectives

Previous investigations have utilized vibroarthrographic methods for various musculoskeletal related initiatives. Most notably is extensive research into the development of a classifier for normal and abnormal knees. Other research has investigated applications of vibroarthrography at the hip and the spine. Conclusions from these studies continue to suggest that vibroarthrography has clinical potential and research remains ongoing. This dissertation was conducted to provide unique evidence in the initiative to make vibroarthrography a clinically relevant tool. Three investigations were executed to assess the applications of vibroarthrography at the knee and hip. Although these investigations used similar instrumentation, the data collection methods, post-processing techniques, and the assessments conducted were distinctly different depending on the objectives. The primary objective of the first investigation was to quantitatively describe hip separation as it existed in a mechanical total hip simulator using features derived from vibration signals. Specifically, this research sought to determine 1) how increases in separation, edge loading, and subsequent femoral head reduction effect vibroarthrographic features, and 2) how vibroarthrographic features correlate to standardized periods of the gait cycle in the presence of a forced instability.

The objective of the second investigation was to use vibroarthrography to quantify the mechanics of cam-post engagement in a posterior stabilized total knee arthroplasty. The aims of this investigation were 1) determine how effective vibroarthrographic features are in estimating the time of cam-post engagement, 2) define the correlation between vibroarthrographic features and cam-post engagement velocity, and 3) define the correlation between the vibroarthrographic features and cam-post engagement height.

The final investigation was designed to determine if vibroarthrography could be used to assess the mechanical efficacy of viscosupplementation in osteoarthritic knees. The objectives of this research were 1) quantify the relationship between preoperative and postoperative vibrations emitted from a diseased joint that was treated with an intra-articular hyaluronic acid injection, 2) determine if viscosupplementation results in more a normal like vibroarthrogram, and 3) determine if vibroarthrography could be used to supplement the assessment of a non-surgical treatment’s success.

1.3. Contributions

To the best of the author’s knowledge, the three investigations presented here are the first of their kind. Previous vibroarthrographic investigations of hip separation have been conducted in vivo, but never has a well-controlled mechanical total hip simulator been used to study the incremental effects of increasing hip separation on the vibrations measured in close proximity to the joint. Similarly, although vibrations have previously been described in brief to relate to cam-post engagement, no robust quantitative analysis has ever been conducted to detail the relationships between vibrations and dynamic variables associated with this mechanism. Lastly, vibroarthrography has never been used to dynamically evaluate the effectiveness of a non-surgical treatment for knee osteoarthritis. In completion of these investigations the following contributions were made:

1. Vibroarthrographic data collection methods for a mechanical total hip simulator
2. Signal processing and denoising techniques for vibrations measured on a total hip simulator
3. Data segmentation strategy for the analysis of vibrations in relation to standardized gait cycle periods
4. Analysis that demonstrates the effects of increasing hip separation on vibroarthrographic features
5. Fully untethered, wearable data acquisition system for the monitoring and collection of vibrations synchronized with fluoroscopy
6. Methods for approximating the occurrence of cam-post engagement with vibroarthrography
7. Methods for measuring cam-post engagement velocity in vivo

8. Analysis that demonstrates correlations between vibroarthrographic features and cam-post engagement velocity
9. Analysis that demonstrates correlations between vibroarthrographic features and cam-post engagement height
10. Methods for measuring the vibroarthrographic effects of a non-surgical treatment for osteoarthritic knees
11. Methods for comparing vibroarthrographic features across multiple time points

All the algorithms used to conduct these analyses were incorporated into a custom designed MATLAB based software package that can be used by CMR personnel for the systematic and efficient analysis of vibroarthrography related data in the future.

CHAPTER 2. REDUCTION OF THE FEMORAL HEAD FOLLOWING HIP SEPARATION: AN IN VITRO VIBROARTHROGRAPHIC INVESTIGATION OF INSTABILITY IN A TOTAL HIP SIMULATOR

Raw data for this research was collected at the University of Leeds. Dr. Mazen Al-Hajjar and Trevor Grieco worked together to design the study and set up the experiments at the University of Leeds. All final data was collected by Trevor Grieco at the University of Leeds, and all analyses were conducted by Trevor Grieco at the University of Tennessee.

2.1. Abstract

Technologically objective diagnosis of instabilities in THA post-operatively is limited to invasive and/or static approaches. Because of this, orthopaedic’s most advanced diagnostic instruments tend to be used only in cases of gross instabilities. Thus, minor instabilities like edge loading and component loosening, may remain unnoticed for years until the instability has compromised the joint. Detecting and quantifying minor instabilities before maturation into gross instabilities can reduce clinical risk, as well, as, emotional and financial burdens on patients, physicians, and healthcare providers. Edge loading of femoral heads on acetabular liners has been observed under dynamic in vivo conditions, and in vitro simulations of edge loading have reproduced clinically relevant wear patterns when compared to implant retrievals. Such investigations have concluded that small malalignment of the joint centers can result in minor instabilities. These result in unintended wear patterns which may lead to premature implant failure. In vivo investigations have suggested that surface vibrations can be used to detect instabilities in total hip arthroplasty. This work investigated the technique in vitro for the first time to gain a more thorough understanding of discriminant vibration features that can potentially be used for diagnostic purposes.

During stance phase of the simulated gait cycle, significant impulse signals existed in correlation with the reduction of the femoral head following induced medial/lateral shifts that were less than 1 mm in magnitude. Additionally, controlled increases in the medial/lateral shift correlated with increases in the energy of the associated impulse signals. These findings suggest that when evaluated in relation to standard gait cycle periods, vibroarthrography has potential to provide valuable diagnostic information related to the presence of edge loading and subsequent femoral head reduction in a total hip arthroplasty. Additional research is required to test the methods in vivo.

2.2. Introduction

Since first introduced in the 1960s by Sir John Charnley, the modern THA has undergone decades of refinement that has positioned it amongst the most successful surgical procedures in modern medicine [40]. Despite its resounding success, design rationale; surgical technique; and component position theory continue to evolve as demand for more functional THA increases. Amongst issues that plague THA, is malalignment of the acetabular component. Malalignment can be both rotational and translational in nature. Rotational malalignment is characterized by excessive inclination and/or anteversion of the acetabular component while translational malalignment is due to improperly aligning the centers of the femoral head and acetabular cup [41]. Such malalignments may result in undesirable impingement, edge loading, accelerated wear, and dislocations.

Efforts to mitigate such instabilities and failure modes in THA can be categorized into 1) implant design rationale and 2) surgical technique. From the Charnley to the dual mobility hip, surgeons have been provided access to a range of THA geometries intended to restore hip functionality. Head size, cup diameter, neck length, neck angle, head-neck ratio, femoral stem angle, and femoral stem length may all affect patient outcomes [42, 43]. Numerous investigations have isolated various culprits and solutions for instabilities. For example, large femoral heads and constrained liners have been recommended and demonstrated to reduce THA instabilities such as dislocation and edge loading [44-46]. More recently the dual-mobility hip has been suggested as an alternative to large femoral heads citing its enhanced wear performance in the presence of third-body particles and microseparation [47]. Despite these solutions and others, mechanically speaking, the correct combination of selected components is required to truly optimize the stability of the total joint system. Therefore, provided with appropriate components, successful restoration of the joint mechanics still hinges upon proper surgical implementation. Despite the joint’s simplistic ball and socket geometry, a few degrees can make all the difference. The orientation of the acetabular cup is most often described by two angles – inclination and anteversion. In the 1970s, Lewinnek et al. proposed the “safe zone” pertaining to cup orientation in THA [48]. This zone suggested if cup inclination was 40° ± 10° and cup anteversion was 15° ± 10° the risk of dislocation was minimized [48]. For the last 30 years this safe zone has been recommended and accepted as the gold standard amongst most surgeons [49]. However more recently, fine tuning this concept has been of interest to further optimize THA mechanics. Reports of dislocation and abnormal wear despite appropriate positioning with regards to the “safe zone” [43] have fueled investigations of the reference frames and patient specific dynamics that affect hip replacement and function. Abdel et al. reported that in a group of 206 primary THAs that subsequently dislocated, 120 of them were within the Lewinnek safe zone. It was concluded that this majority demonstrated that THA stability is multifactorial and that for some patients, ideal acetabular component positioning is likely outside the Lewinnek safe zone. Inconsistencies in measuring and discussing anteversion and inclination has led to confusion amongst researchers and surgeons [42]. Indeed three reference frames (anatomic, radiographic, and operative) are used to describe these angles in practice and literature [42, 50], and not surprisingly, the choice of reference frame can have a substantial impact on the reported angles [42]. In addition to measurement technique, it is clear now that pelvic tilt (PT), which has been shown to have a pre-operative inter-subject range in excess of 35°, also affects the “functional” anteversion and inclination [51]. Additional investigations have demonstrated that proper target alignment needs to consider the patient specific dynamics so that cup positioning is more functional during activities of daily living [49, 52, 53].

Malalignment can result in inadequate coverage of the femoral head by the acetabular component during activities of daily living. This coverage relates directly to the elastohydrodynamic lubrication (EHL) of the joint and in cases of suboptimal coverage, the EHL is compromised resulting in increased wear [54, 55]. Therefore, mitigation of wear requires a technique by which coverage can be confidently measured through various ranges of motion. The calculation of the contact patch to rim (CPR) distance is one metric of coverage that accounts for component size, design, and acetabular orientation (Figure 2.1) [56-58]. CPR distance utilizes radiographs and data from Bergmann's telemetry investigation to measure functional coverage [59]. Multiple investigations have reported correlations of CPR distance to edge wear [56, 57] and CPR distance was recently described as the best calculation to assess functional coverage [58]. Currently surgical navigation that combines CPR distance theory with patient-specific anatomy and computational modeling is being utilized by early adopters in the operating room to optimize acetabular component positioning.

Despite guidelines intended to minimize instabilities in THA, instances of "separation" during gait and abduction/adduction maneuvers have been observed in vivo with fluoroscopic techniques [36, 37, 44, 60, 61]. The separation described within this work is not a complete dislocation of the femoral head, but rather a less severe loss in the coincident geometrical relationship of the femoral head center and the center of the acetabular cup. During such a scenario the femoral head may still be in contact with liner. Other works refer to the phenomenon as "microseparation" as it is usually on the magnitude of hundreds of microns. In cases for which the femoral head is known to maintain contact with the liner, the term lateralization may be used. Previous in vitro investigations have simulated microseparation through mechanical means by application of external forces. Millions of gait cycles that incorporate microseparation successfully reproduce

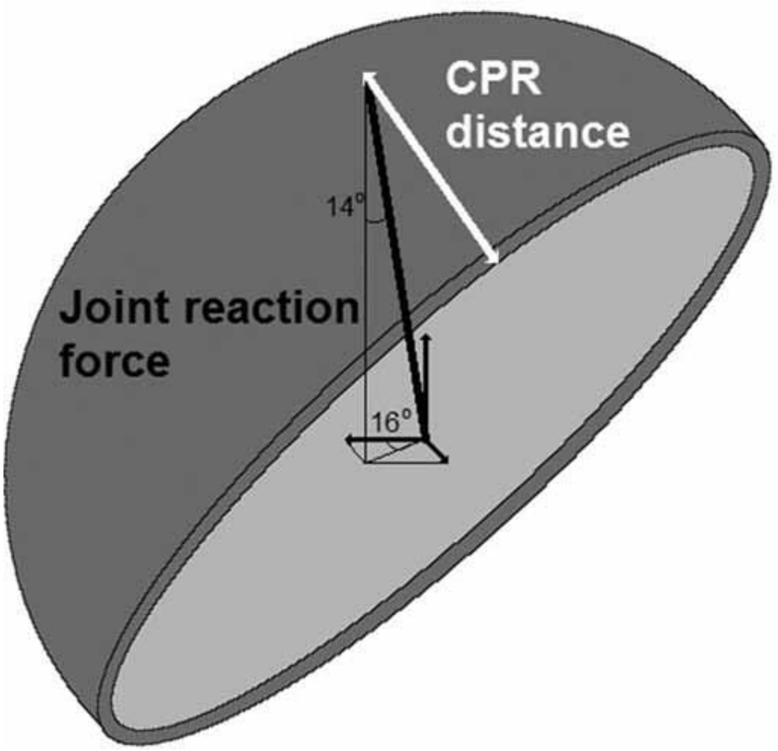

Figure 2.1. Schematic illustrating the contact patch to rim distance for the measure of functional coverage in THA as described and presented by Amstutz and Le Duff [58].

clinically relevant wear patterns when compared to failed acetabular components and femoral heads obtained through retrieval research [41, 62]. The separation of the femoral head with respect to the acetabular liner is most commonly reported to occur in an inferior-lateral direction such that when the leg is unloaded during swing phase, no compressive forces maintain the concentricity of the malaligned joint centers. Depending on alignment, position, soft tissue tension, and muscle forces [62], the joint may migrate to a position of equilibrium that compromises the contact mechanics of the hip. If the contact patch approaches the acetabular rim during swing phase, then unintended loading of the rim (edge loading) can be expected upon reloading the joint. Millions of steps later, this edge loading results in wear that that can lead to a costly revision.

Identification of the microseparation in vivo is not trivial. To date it has only been confirmed with fluoroscopic evaluation which is inconvenient and involves exposing subjects to ionizing radiation. Incidences of audible squeaking in hips has led to the investigation of joint sounds and vibrations at the skin surface in hopes of developing a noninvasive diagnostic tool for identification of microseparation and/or other instabilities in THA [36, 37]. Although the signals are corrupted by noise and require substantial post processing, preliminary investigations correlating fluoroscopically derived THA kinematics to sound and vibration signals suggest potential for this technology [36, 37]. Furthermore, as the hip joint is deep and often surrounded by substantial adipose tissue, deliberating the signal from noise is near impossible without some preexisting knowledge of characteristic signal features. To effectively begin validation of vibration as a diagnostic tool in hips, it is critical to start in a controlled environment such as a mechanical simulator that can effectively replicate instabilities of interest.

The Leeds Mark II Physiological Anatomical hip simulator has been utilized effectively to replicate clinically relevant wear rates and patterns when compared to retrieved implants. This simulator has been successfully deployed to study metal-on-metal (MoM), metal-on-polyethylene (MoP), ceramic-on-ceramic (CoC), and ceramic-on-polyethylene (CoP) THAs [47, 62-66]. Aside from material properties, experiments have demonstrated the simulator's role in discerning wear as it relates to component size and component alignment [66]. Most importantly with regards to the present study, the system has been modified to mechanically simulate the adverse conditions associated with edge loading during the swing phase of gait [62, 64, 65]. More recently, mathematical models have been validated with these experimental results from the simulator to provide additional insight with regards to the contact forces and wear mechanisms associated with the microseparation [41, 49, 67]. Considered a well validated in vitro test bed for THA investigations, this simulator was selected for the initial vibration assessment of THA instabilities in vitro.

Although rotational malalignment is of interest, this investigation focused solely on translational malalignment. In this research, it was hypothesized that the instability of microseparation in a MoP THA could be successfully measured and characterized by surface vibrations and that differences in magnitudes of microseparation could be clearly distinguished in features derived from the vibroarthrograms.

2.3. Materials and Methods

2.3.1. Experimental Configuration of the Simulator

All experiments used the Leeds Mark II Physiological Anatomical hip joint simulator at the University of Leeds Institute of Medical and Biological Engineering (Figure 2.2). A single station was prepped with DePuy Synthes (Warsaw, IN, USA) THA components (Table 2.1). This system has been described and modelled as two major parts – the cup holder and the femoral stem [67]. The cup holder used was designed such that the acetabular components were set at 45° of inclination and

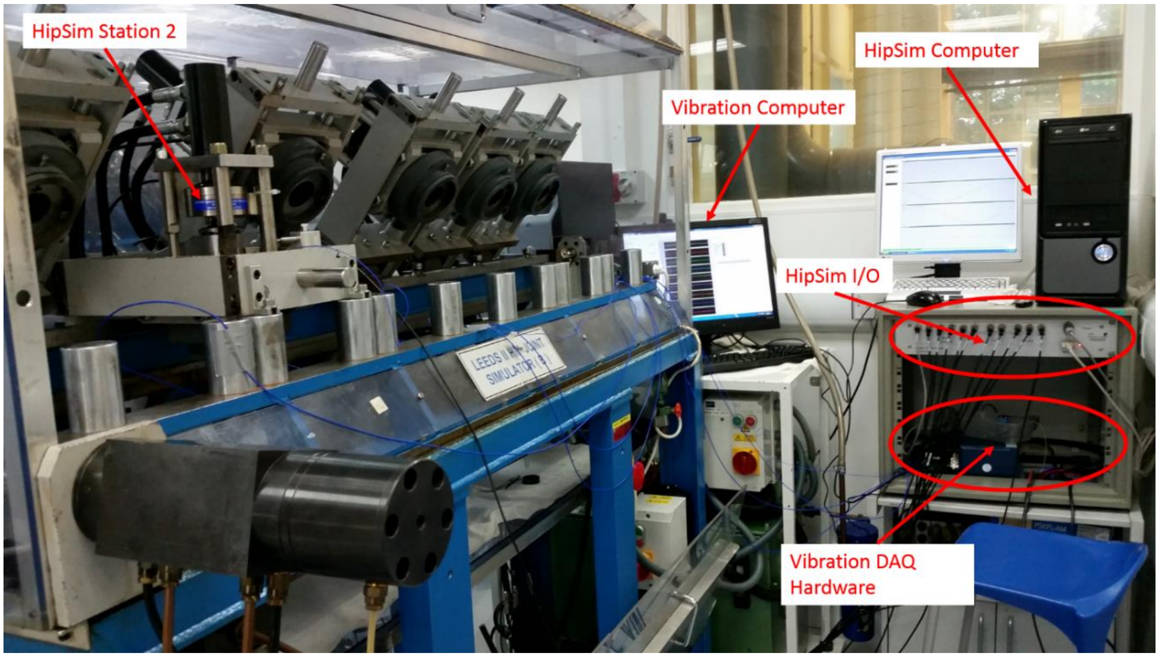

Figure 2.2. The experimental setup utilized a single station of the Leeds II Physiological Anatomical hip joint simulator along with hardware and software unique to collecting vibrations.

Table 2.1. DePuy Synthes Total Hip Arthroplasty Component Details

Component	**Size**
PINNACLE® POROCOAT® Acetabular Shell 100 Series	56mm outer diameter
PINNACLE® MARATHON® Polyethylene Acetabular Shell	36mm inner diameter, 56mm outer diameter
M-SPEC™ Metal Femoral Head	Ø36mm +5 12/14 Taper
C-STEM® AMT	Size 1

0° of anteversion. The acetabular shell was cemented into the cup holder and the liner was press fit into its appropriate position. It can be assumed that the liner is rigidly connected to the acetabular shell and that the acetabular shell is rigidly connected to the cup holder. The femoral stem was cemented into its respective stem holder. The cup holder, under conditions allowing for separation, exhibited three degrees of freedom (Figure 2.3). These included internal/external rotation (+/- 10°), superior-inferior (SI) translation, and medial-lateral (ML) translation. The femoral stem was limited to a single rotational degree of freedom – flexion/extension (-15° to +30°). Vertical loading was applied down through the acetabular component and the center of the femoral head to simulate body weight (Figure 2.3). The loading was characterized by a twin peak cycle with a peak load of 3 kN and a swing phase load of 0.07 kN. A spring was utilized to induce a medial/lateral shift of the acetabular components, as first described by Nevelos et al. [62], to simulate swing phase hip separation (Figure 2.3). All loading and rotations were driven by the same control algorithm to simulate 1 gait cycle per second.

2.3.2. Data Acquisition

Load profiles and rotations were provided as outputs of the software standard to the hip simulator. This data was sampled at 128 Hz. A separate data acquisition (DAQ) system utilized custom designed LabVIEW based software and a NI 6341-USB DAQ board (National Instruments, Austin, TX, USA) to acquire and log six signals. These included the signals from four accelerometers, a linear variable differential transformer (LVDT), and a sync signal. Four uniaxial accelerometers measured simulator surface vibrations during all experiments. These included three 352C68 accelerometers and one 352A24 accelerometer (PCB Piezotronics Inc., Depew, NY, USA). Both models are high sensitivity, miniature, integrated electronic piezoelectric (IEPE) accelerometers with the same performance

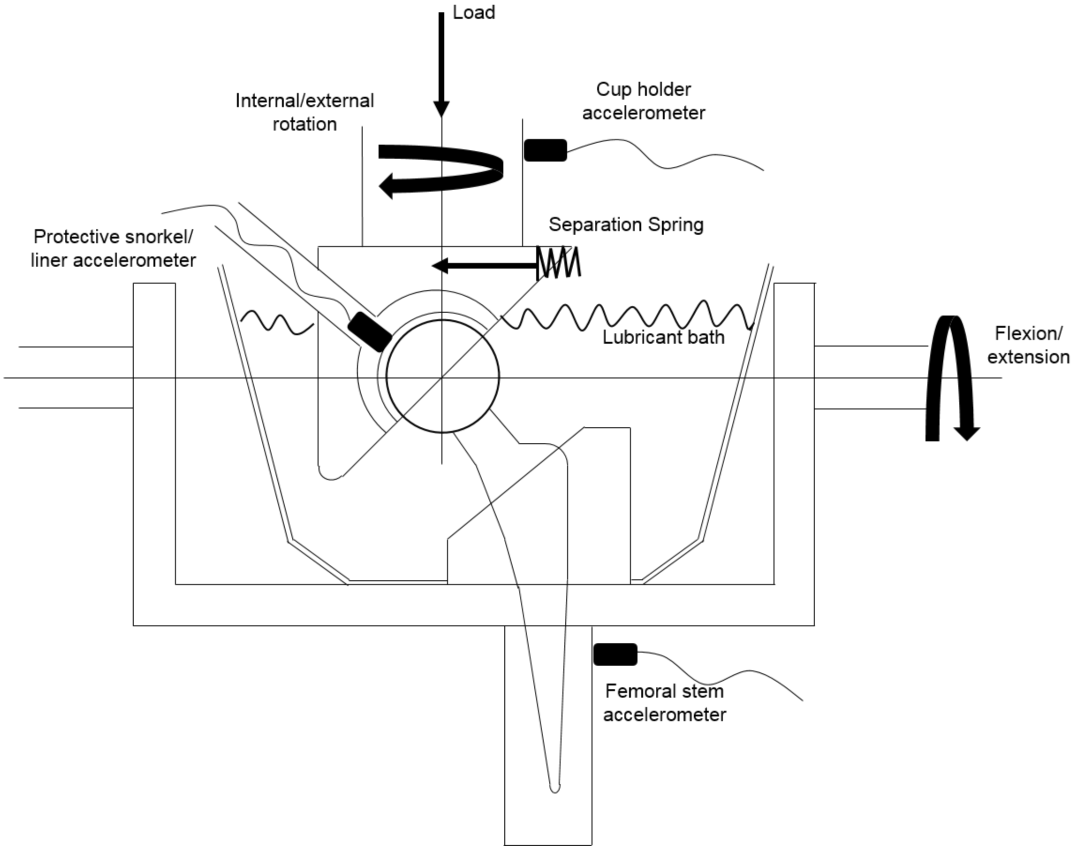

Figure 2.3. Schematic of the Leeds Mark II Physiological Anatomical hip simulator modified to induce a medial/lateral shift of the acetabular components and to measure the vibrations experienced at the hip joint with accelerometers.

specifications (sensitivity of 100 mV/g, a measurement range of ±50 g pk, and a frequency range of 0.5 to 10000 Hz (±5%)). The models differ in physical specifications which allowed for the accelerometers to be most effectively utilized in certain locations of interest on the simulator. All accelerometers were connected to the input terminals of an IEPE signal conditioner (482C16, PCB Piezotronics, Depew Inc., NY, USA) which was configured to amplify all incoming signals by a factor of 10 (Figure 2.4). Positive leads (red) from the signal conditioner outputs were connected to positive analogue inputs (AI) 0-3 on the DAQ board. Negative leads (black) were connected to respective AI ground (GND) terminals on the DAQ board (Figure 2.4). One LVDT (D6/02500A-L10, RDP Electronics Ltd. Wolverhampton, UK) was used to measure the medial/lateral displacement of the cup holder. This sensor had its own respective signal conditioner and was calibrated to 4 V/mm. The positive lead of the LVDT output was connected to AI 4+, and the negative lead was connected to its respective AI GND on the DAQ board (Figure 2.4). Due to the uncoupled nature of the two data acquisition systems (HipSim and LabVIEW), a simple circuit was created to synchronize outputs. This circuit consisted of a 9 V battery, a switch, and two parallel branches with LED indicators and output terminals. One branch connected to AI 5+ and AI 5- on the DAQ board (Figure 2.4). The other branch connected to the Load Cell 1 input on the HipSim system. Specifically, an extra load cell cable was cut at one end, and the cable was stripped back to expose the 5 wires. The white wire was connected to the positive terminal and the green wire was connected to the negative terminal of the sync circuit output. Using the switch to open/close the circuit provided a sync signal in the form of a voltage drop/gain that could be identified in both the HipSim and LabVIEW data files.

All incoming signals from the DAQ board were sampled at 10 kHz in LabVIEW. Channels AI 0:4 were configured as reference single-ended inputs, and channel

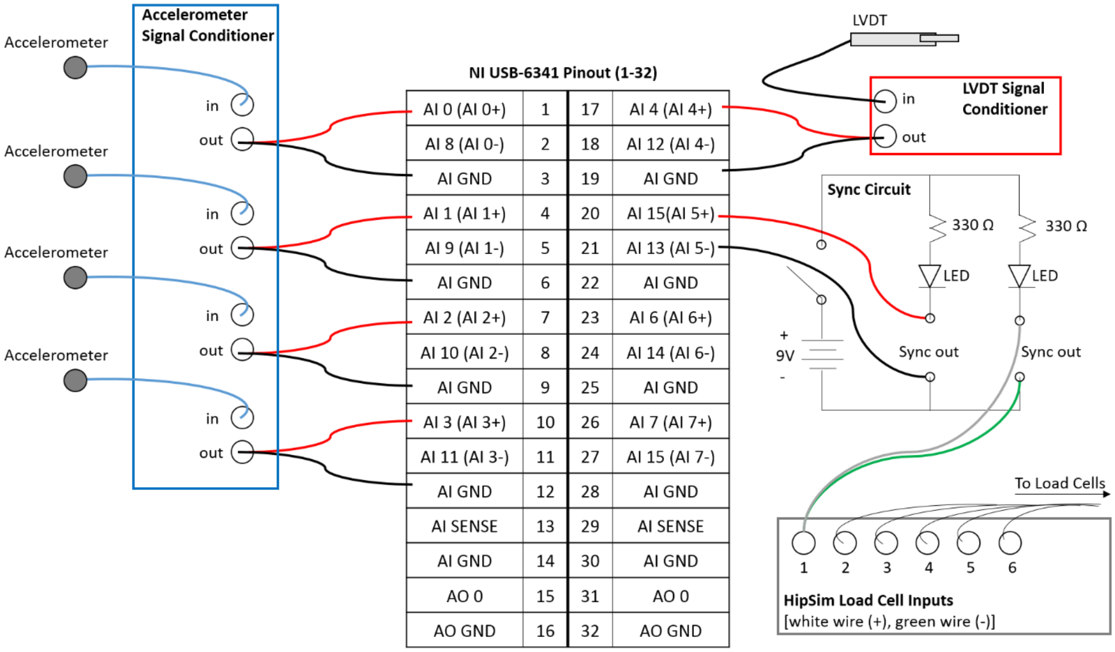

AI 0 (AI 0+)	1	17	AI 4 (AI 4+)
AI 8 (AI 0-)	2	18	AI 12 (AI 4-)
AI GND	3	19	AI GND
AI 1 (AI 1+)	4	20	AI 15(AI 5+)
AI 9 (AI 1-)	5	21	AI 13 (AI 5-)
AI GND	6	22	AI GND
AI 2 (AI 2+)	7	23	AI 6 (AI 6+)
AI 10 (AI 2-)	8	24	AI 14 (AI 6-)
AI GND	9	25	AI GND
AI 3 (AI 3+)	10	26	AI 7 (AI 7+)
AI 11 (AI 3-)	11	27	AI 15 (AI 7-)
AI GND	12	28	AI GND
AI SENSE	13	29	AI SENSE
AI GND	14	30	AI GND
AO 0	15	31	AO 0
AO GND	16	32	AO GND

Figure 2.4. Accelerometers and the LVDT were connected to analog inputs of the NI USB-6341 DAQ board. The sync circuit was connected to both the NI USB-6341 DAQ board and an unused load cell input for the hip simulator so that signals from the two systems could be synchronized during post processing.

AI 5 was configured as a differential input. Data was collected from all simulations in the same systematic manner. This involved the following steps: 1) Start LabVIEW program, 2) turn on hip simulator pump and filter, 3) start gait simulation, 4) start LabVIEW recording after a minimum 15 gait cycles, 5) flip sync circuit switch and allow for a minimum 30 more gait cycles, 6) flip sync circuit switch, 7) stop LabVIEW recording, 8) Stop simulator.

2.3.3. Simulating and Measuring Hip Separation

The cyclical loading of the hip simulator coupled with the appropriate positioning and tensioning of a spring induces a medial/lateral shift of the cup holder that can be measured with the LVDT (Figure 2.5) [62]. More specifically when the vertical loading was reduced the spring would force the cup holder to shift medially. As loading was reintroduced to the system the spring would be forced back into tension allowing the cup holder to return to its original position. Depending on the amount of separation, this return may be notably characterized by the acetabular liner impacting the femoral head. The motion in this experimental setup has been previously modelled as four distinguishable phases: 1) lateral separation, 2) edge loading, 3) relocation, and 4) centered conditions (Figure 2.6) [67]. The peak-to-peak voltage (V_{pp}) of the LVDT signal was used to assess the physical magnitude of separation. Three simulations with increasing magnitudes of medial/lateral shift were conducted. These included a control (0 mm of separation), approximately 1 mm of separation, and approximately 2 mm of separation. During standard gait with no separation the spring was not under any tension, and the femoral head was assumed to maintain concentric contact with the acetabular liner (Figure 2.7A). For 1 mm and 2 mm separation trials the spring was iteratively tensioned to achieve peak-to-peak voltage measurements that were as close to the target value (4 V_{pp} and 8 V_{pp} respectively) as possible before recording data. A small medial/lateral shift was present in the control scenario gait cycles (average

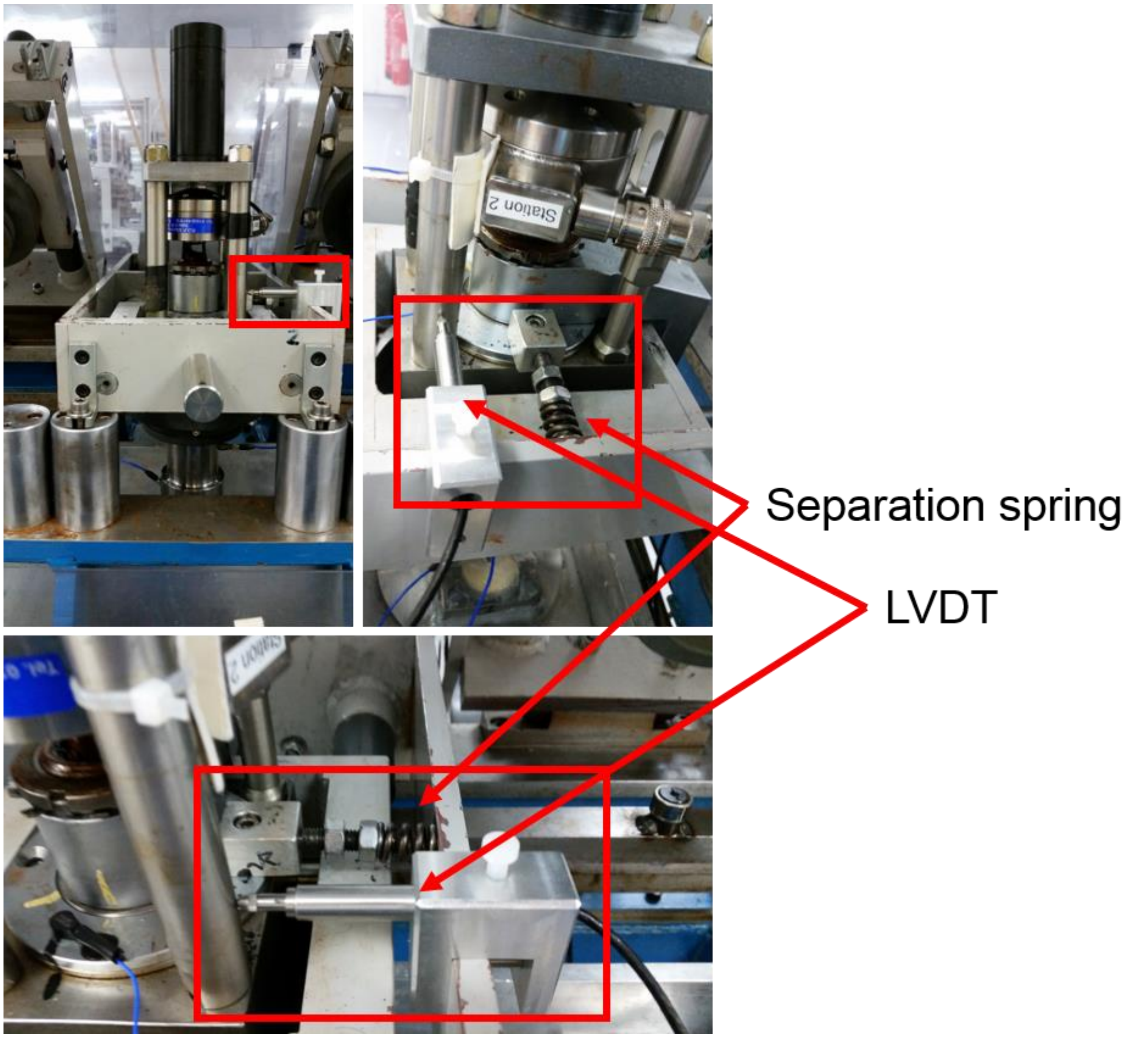

Figure 2.5. A linear variable differential transducer (LVDT) was used to measure the medial-lateral separation that was induced by a spring during swing phase of the loading cycle.

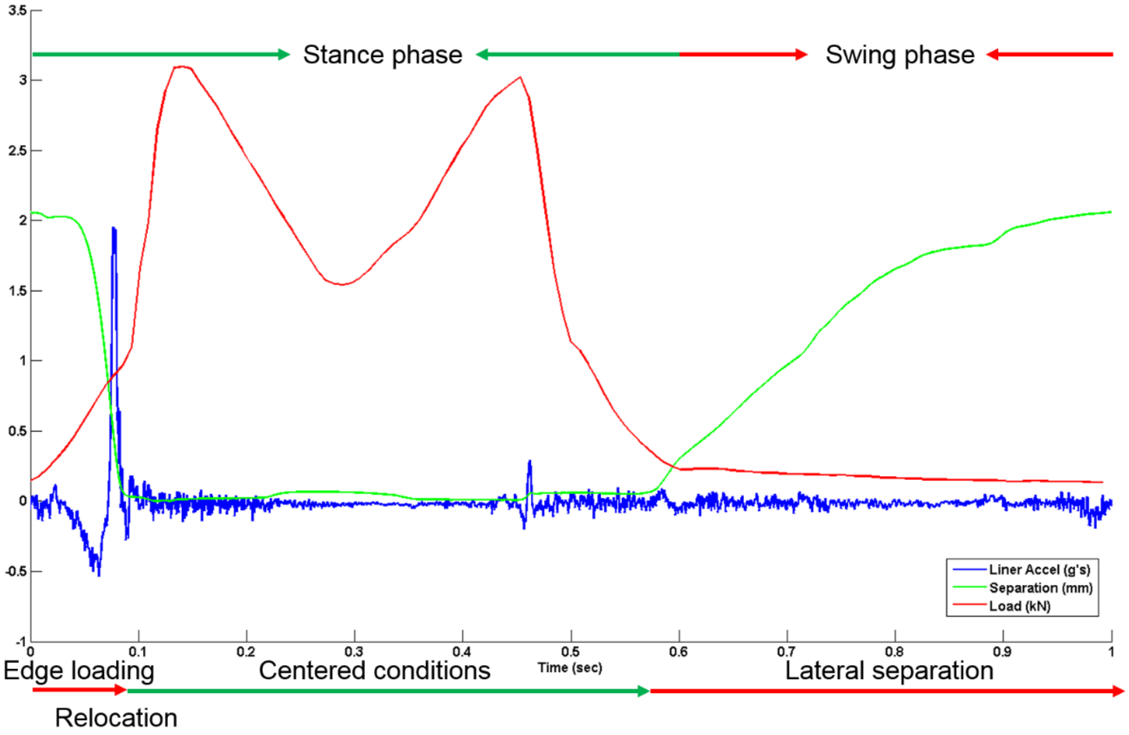

Figure 2.6. During swing phase, the vertical load (red line) on the joint is negligible and lateral separation (green line) gradually increases. When loading is reintroduced at the beginning of stance phase, edge loading occurs. As the load overcomes the spring force, the separation decreases sharply and the accelerometer (blue line) experiences a pronounced impulse associated with the abrupt reduction of the femoral head with respect to the liner as it relocates to centered conditions.

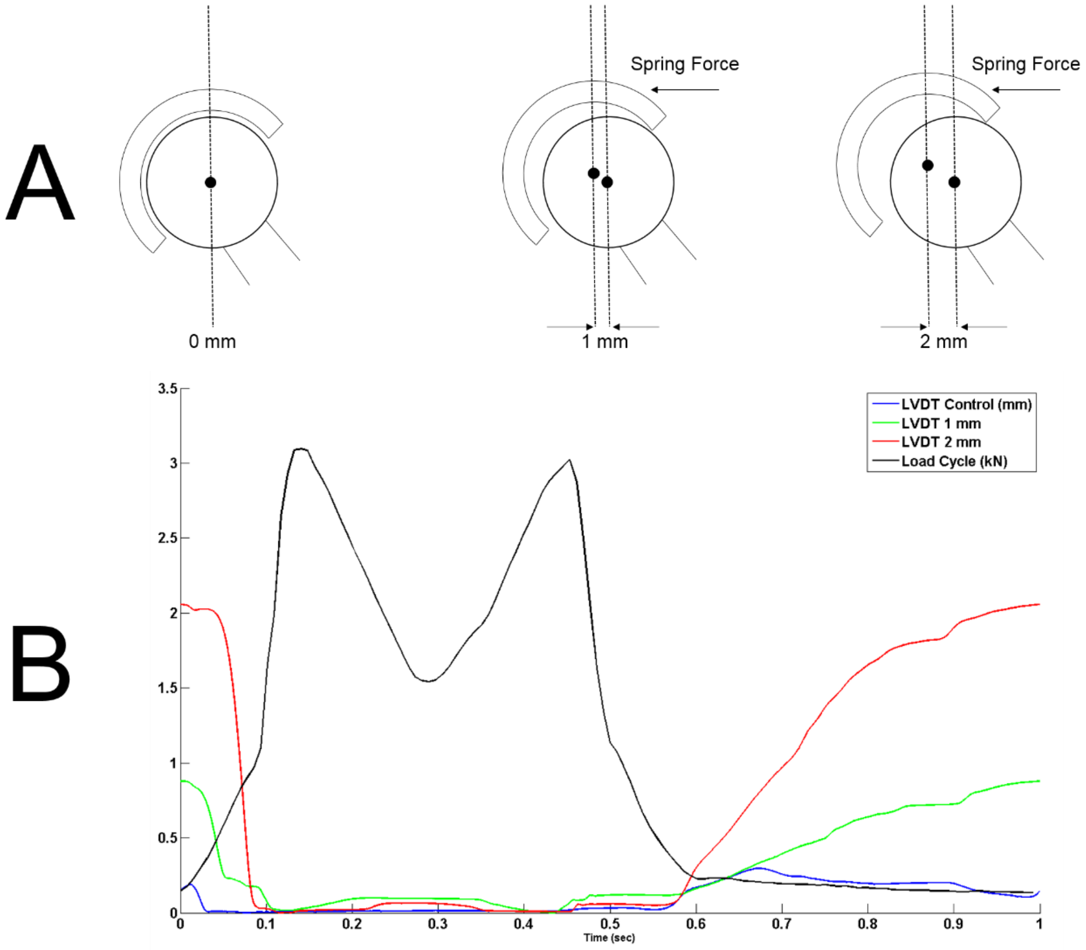

Figure 2.7. (A) Translational instability was forced by increasing tension in a spring to induce a superior-medial shift of the of the acetabular components with respect to the femoral head. (B) The average LVDT data and load cycle illustrates the difference in medial/lateral shift that was induced by the spring experimentally.

maximum = 0.2975 mm) (Figure 2.7B). The average maximum medial/lateral shift for the 1 and 2 mm gait cycles was 0.8789 mm and 2.0586 mm respectively (Figure 2.7B). Although, the medial/lateral shifts are not exactly at the target value the trials will be referred to as 0 mm, 1 mm, and 2 mm for the remainder of this report.

A series of trials were undertaken for three unique configurations of the hip simulator. These configurations were characterized by the lubricant used at the joint. Lubrications included Vaseline, water, and diluted bovine serum. The Vaseline and water-based experiments were merely conducted to ensure progression in complexity of the hip simulator configuration was warranted. The vibration data from these preliminary experiments does not offer additional insight, but rather is subject to inferior anatomical representation of the hip joint as vibrations will be amplified due to increased friction resulting from the lack of adequate EHL. Therefore, the data collected from serum-based experiments was used for final analyses as it is considered the most well-defined experiment with regards to simulating human gait. Two accelerometers were mounted as close to the center of the joint as possible on the acetabular components (Figure 2.3). One of these was screwed into the cup holder, and the other was mounted directly to the acetabular liner (Figure 2.8). The cup holder site was prepared by tapping a hole to match the mounting thread of the accelerometer (5-40) such that the sensor was essentially flush with the surface of the cup holder after being screwed into position. The liner site was prepared by machining a tunnel into the medial aspect of the cup holder. This tunnel was aligned with the retrieval hole that is present on the acetabular shell, thus exposing a small circular region of the acetabular liner on which the accelerometer could be directly mounted with an adhesive. Since this site was below the surface of the lubricant bath, the following steps were taken to protect the accelerometer from damage that may have occurred if it were to come in contact with the fluid. First the circumferential area between the liner and the

Figure 2.8. (Left) An accelerometer was screwed directly into the cup holder. (Middle) A tunnel was machined into the cup holder to expose the acetabular liner through the insertion hole present on the acetabular shell. (Right) An accelerometer was mounted directly to the acetabular liner.

cup holder was filled with silicone to prevent serum from seeping through any gaps present between the acetabular liner and the shell (Figure 2.9). Second a snorkel was created for the tunnel; a plastic tube with a diameter slightly smaller than that of the tunnel was selected to ensure a tight fit inside the tunnel. Before installing the snorkel, the accelerometer was passed through the snorkel and mounted into position on the liner with super glue. Once dry, the snorkel was put into position and surrounded with silicone (Figure 2.9). The lubricant bath was contained by a gaiter that encapsulated all suitable mounting sites on the femur near the joint center (Figure 2.10). Therefore, the femoral accelerometers had to be positioned further from the joint center than the acetabular accelerometers. One was positioned on the cylindrical stem holder (Femur ML), and the other was mounted on the cross beam of the femoral frame that supports the femoral components (Femur SI) (Figure 2.10). Femoral accelerometers were mounted to these locations with petro wax (080A24, PCB Piezotronics, Depew Inc., NY, USA).

All analyses of vibration data were conducted at the University of Tennessee using MATLAB (MathWorks, Natick, MA, USA). Three datasets (0 mm, 1 mm, and 2 mm of separation) were processed in the following manner. First raw data acquired by the two systems (LabVIEW and HipSim) within each simulation was synchronized using the two sync signals that existed in each data set. Next, the synchronized data was cropped at the front end so that the first sample of each gait cycle corresponded to the first reloading sample (physiologically this sample can be considered heel strike) (Figure 2.11). The data was cropped again at the end of 25 complete gait cycles. The 25 gait cycles (each of which contained 10000 samples aligned in time) were averaged to obtain a single mean gait cycle. Prior to any further processing, the accelerometer data was assessed for noticeable signs of impact. Inspection focused on the edge loading and relocation segment of the gait cycle for 1 mm and 2 mm of separation. The medial/lateral velocity of the cup

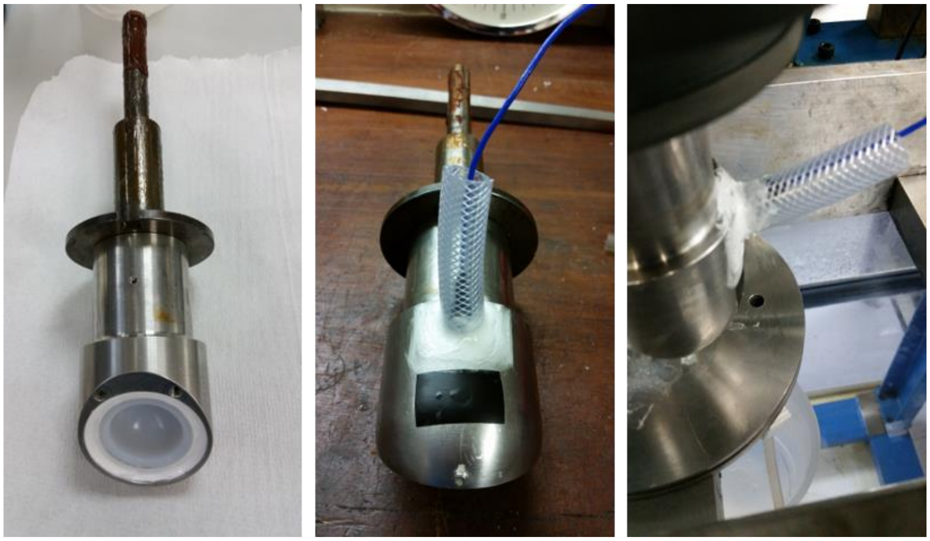

Figure 2.9. (Left) Silicone was applied to the area between the acetabular liner and the cup holder to prevent serum from seeping through the backside where the accelerometer was mounted. (Middle and right) The snorkel was positioned in the tunnel and surrounded with silicone to protect the accelerometer from serum.

Figure 2.10. (Left) The “Femur ML” accelerometer was mounted below the simulator on the femoral stem holder such that its axial direction was medial/lateral. (Right) The “Femur SI” accelerometer was mounted on the cross beam of the femoral frame such that its axial direction was superior/inferior. A silicone gaiter was used to encapsulate the joint in a lubricant bath (diluted bovine serum).

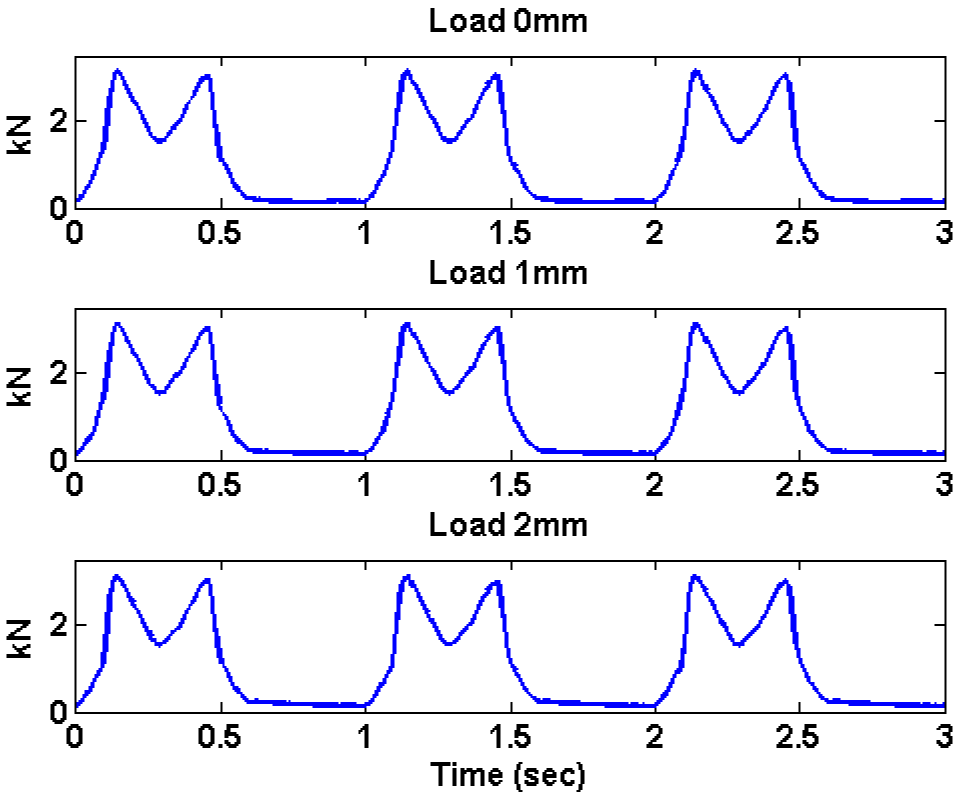

Figure 2.11. The load cycle was used to synchronize the different simulations for analysis. A three second segment of the twin peak load profile from each simulation illustrates the alignment of common characteristics with respect to time.

holder was calculated as the time-based derivative of the LVDT data. The maximum velocity and acceleration experienced by the system was noted for each average gait cycle. Prior to any additional analyses, the signals needed to be processed to eliminate simulator noise.

2.3.4. Discrete Wavelet Transform and Signal Denoising

The discrete wavelet transform (DWT) is a multiresolution technique that uses finite asymmetric functions to approximate a signal. These functions can be dilated (scaled) in space and translated (shifted) in time to obtain a unique decomposition. This localized decomposition enables the transform to isolate singularities and irregularities in a non-stationary signal [68]. This is ideal for naturally occurring signals that tend to have slowly varying components punctuated with transients of interest and are often buried in noise. The DWT involves convolving the signal with filters and dyadic decimation. It can be implemented by passing a signal through an iterated two-channel filter bank that uses unique low and high pass filters to split the signal into course approximations and fine details [69, 70]. These filters can be used to iteratively divide approximation sub-bank data until the desired level of detail is obtained (Figure 2.12). The decomposition can then be used to selectively denoise or process the signal as desired by thresholding coefficients. After processing, the signal can be reconstructed using the inverse discrete wavelet transform (IDWT). As the DWT incorporated two decomposition filters and downsampling, the IDWT incorporates two reconstruction filters and upsampling. These reconstruction filters are quadrature mirror filters of their respective decomposition filters [69, 70].

Since the end of the 1980’s wavelets have been implemented in various biomedical applications including magnetic resonance imaging, computerized tomography, radiography, respiratory-related evoked potential, electromyography, electrocardiography, and electroencephalography [68]. For the present work, the

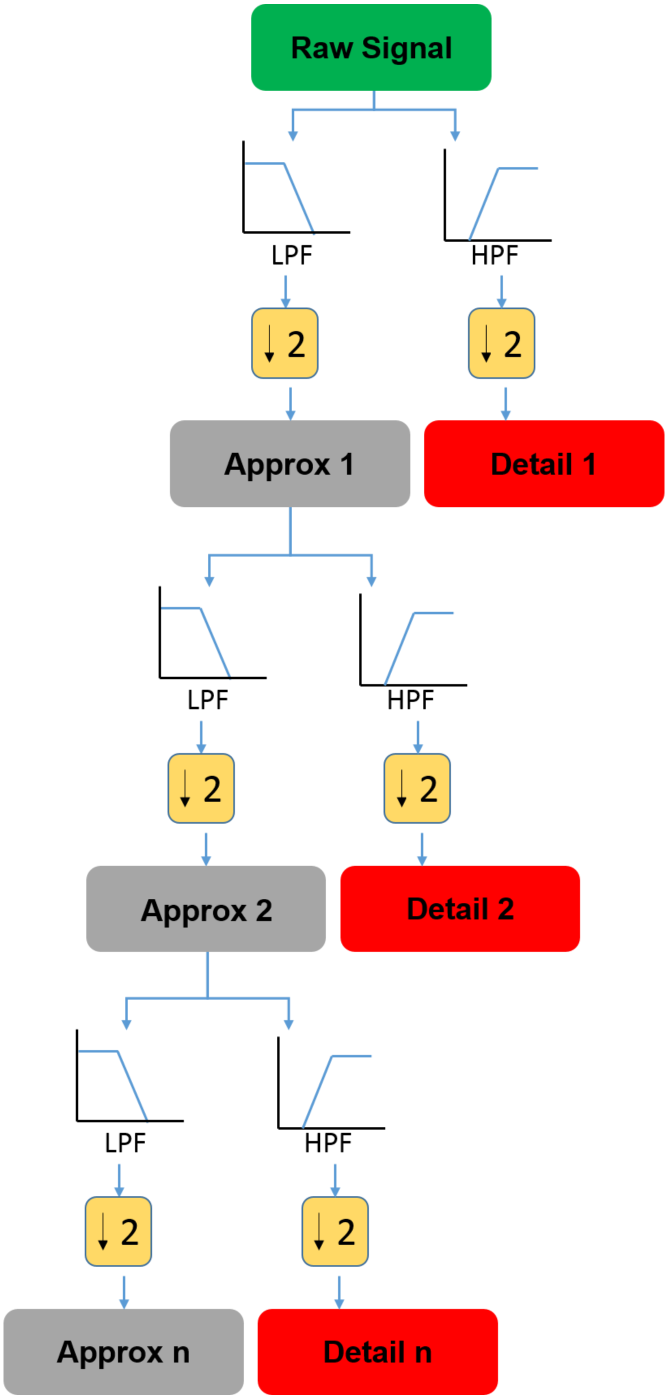

Figure 2.12. The discrete wavelet transform illustrated as a two-channel filter bank with dyadic decimation.

Daubechies 4 (db4) wavelet was selected as the mother wavelet function as it is considered an efficient wavelet for biomedical signal analysis (Figure 2.13 and Figure 2.14) [71]. This mother wavelet has previously been utilized to analyze vibrations emitted from the knee joint [25, 71], and in the present work it demonstrated exceptional correlation with raw signals in regions of interest (primarily the reduction of the femoral head following separation). For each level of a wavelet decomposition a scaled wavelet is translated and convolved with the raw signal to obtain coefficients. To understand the shape of the scaled wavelet at each level, the concept of the wavelet center frequency can be used. The center frequency of a wavelet is the frequency maximizing the Fourier transform of the wavelet modulus [72-74]. For db4, the normed (sampling rate = 1) center frequency is 0.7143 Hz [73] (Figure 2.15). A center-frequency for each scale used in the decomposition can be calculated with the following relationship

$$F_a(j) = \frac{F_c}{2^j \cdot dt}$$

In which

- j is the decomposition level
- dt is the signal sampling period
- F_c is the normed center frequency of a wavelet in hertz
- F_a is the scaled center frequency in hertz corresponding to the level of decomposition, j, and the signal sampling period, dt

The approximations and details have octave bandwidths starting with the Nyquist frequency (Table 2.2) [75]. The average gait cycle from each simulation were decomposed. A level 10 decomposition was performed resulting in detail subbands that ranged from approximately 5 Hz to 5000 Hz (Figure 2.16 and Figure 2.17). Inspection of each level for each unique trial of separation yielded the following

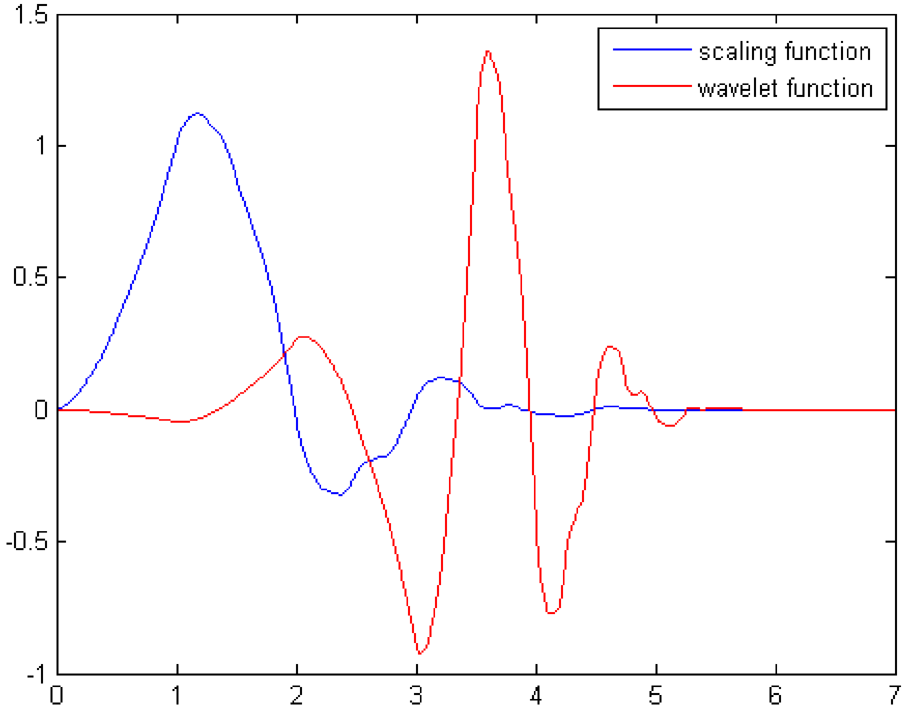

Figure 2.13. Daubechies 4 scaling and wavelet function coefficients for dyadic grid values.

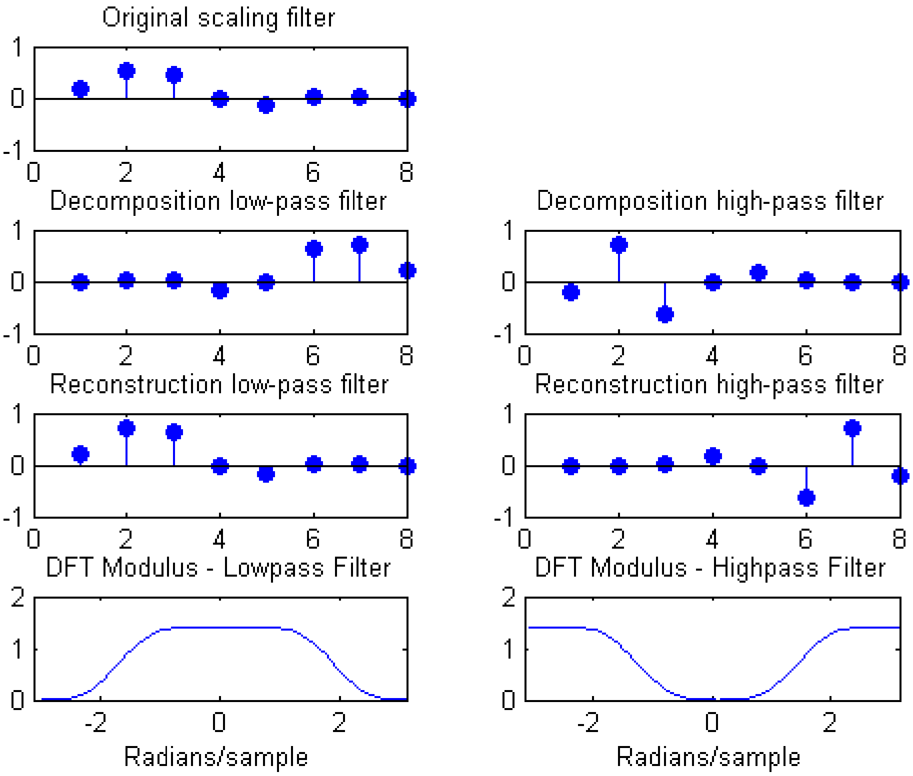

Figure 2.14. Impulse response and discrete Fourier transform (DFT) of Daubechies 4 filters.

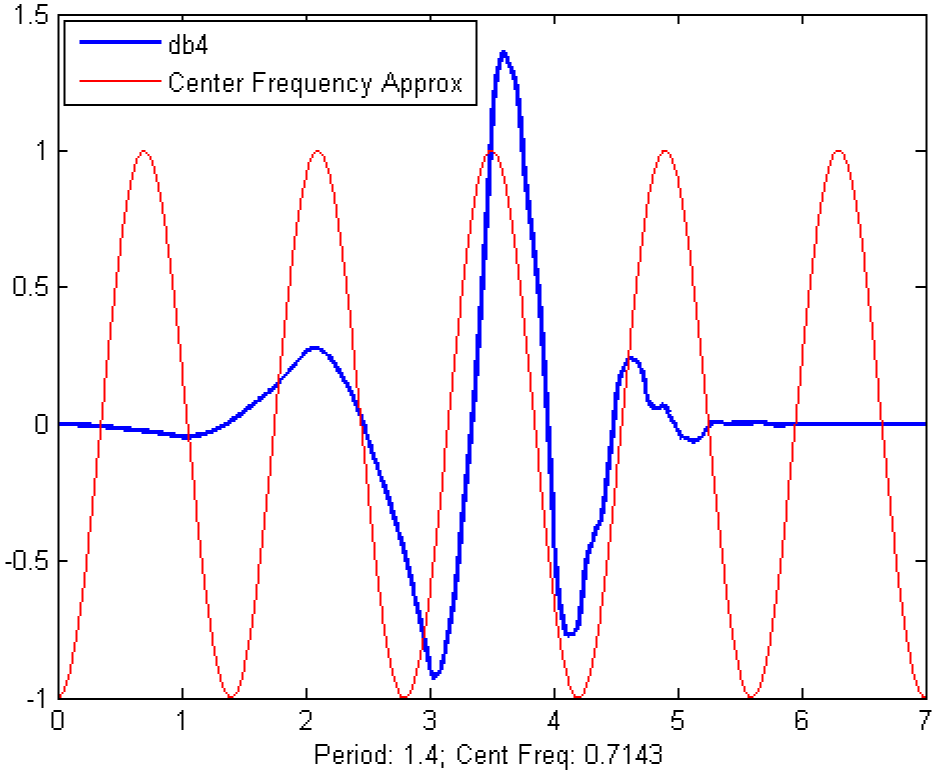

Figure 2.15. The most prominent feature of the db4 wavelet is comparable to a cosine function that oscillates at 0.7143 Hz.

Table 2.2. Center Frequency and Decomposition Bandwidths for a Level 10 db4 Wavelet Decomposition of a Signal Sampled at 10,000 Hz

Level	db4 Scaled Center Frequency (Hz)	Approximation Bandwidth (Hz)	Detail Bandwidth (Hz)
0	7143	0-5000	N/A
1	3571.4	0-2500	2500-5000
2	1785.7	0-1250	1250-2500
3	892.86	0-625	625-1250
4	446.43	0-312.5	312.5-625
5	223.21	0-156.25	156.25-312.5
6	111.61	0-78.125	78.125-156.25
7	55.804	0-39.063	39.063-78.125
8	27.902	0-19.531	19.531-39.063
9	13.951	0-9.766	9.766-19.531
10	6.9754	0-4.883	4.883-9.766

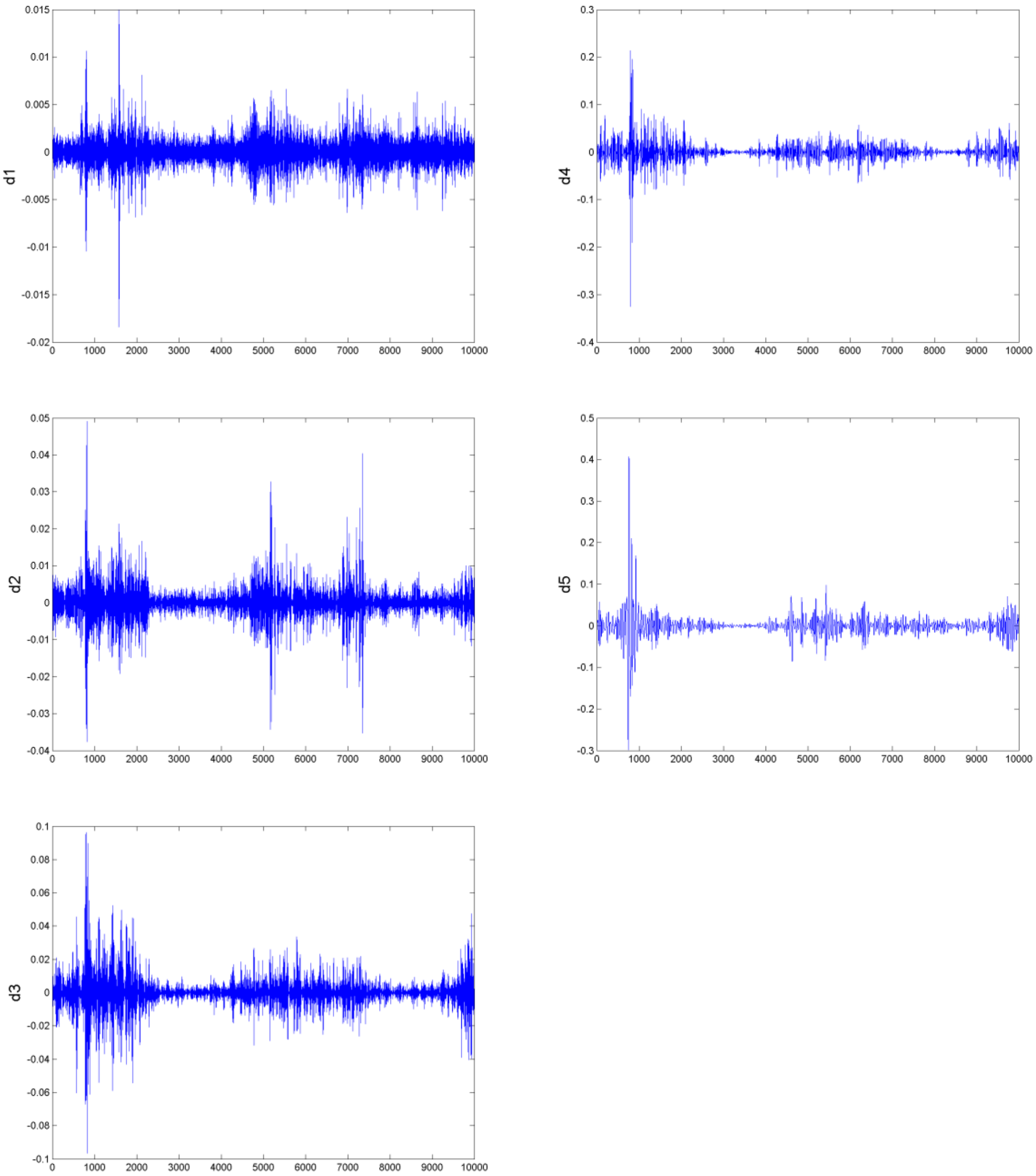

Figure 2.16. Details 1-5 (d1-d5) illustrate bandwidths in which substantial simulator noise corrupted the signal.

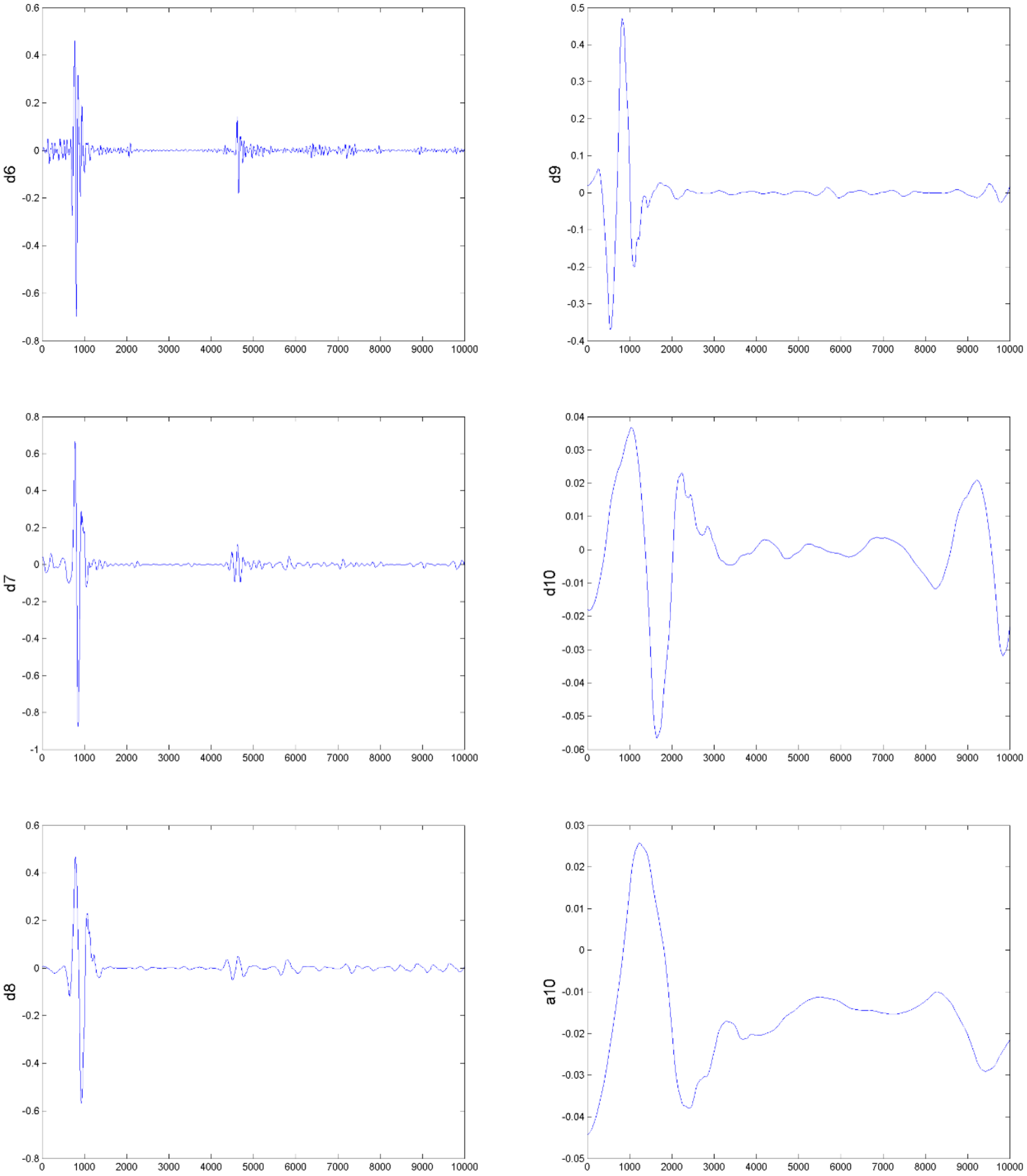

Figure 2.17. Details 6 and 7 (d6 and d7) illustrate bandwidths in which the signal is relatively clear of simulator noise. Details 8-10 (d8-d10) and approximation 10 (a10) illustrate low frequency bandwidths that were not used in signal reconstruction.

conclusions that were eventually used to denoise the signal. Levels 1-5 were similar for all three echelons of separation primarily because these levels were highly corrupted by simulator induced noise. Level 6 and 7 coefficients were distinctly different for each unique amount of separation and exhibited the strongest correlation with the signal during times associated with edge loading and relocation. Levels 8 and 9 exhibited mild correlation in regions of interest but did not provide additional discriminant information. Level 10 detail and approximation coefficients provided no useful information. For each magnitude of separation, levels 6 and 7 detail coefficients were used to reconstruct the signal (Figure 2.18). Reconstructed signal coefficients, C_i, were used to calculate the energy, $E^{(k)}$, in seven commonly described periods, k, of the gait cycle according to Neumann [76]. The seven periods included: 1) loading response, 2) mid stance, 3) terminal stance, 4) pre swing, 5) initial swing, 6) mid swing, and 7) terminal swing. The boundaries, b_k, of these periods were defined as a percentage of the gait cycle coinciding with one of eight events described by Neumann [76]. The energy for each period, k, was calculated as

$$E^{(k)} = \sum_{i=b_k}^{b_{k+1}} C_i^2$$

and the total energy, E_{tot}, for the averaged gait cycle was calculated as

$$E_{tot} = \sum_{i} C_i^2$$

The relative energy, $p^{(k)}$, for each period was calculated as

$$p^{(k)} = \frac{E^{(k)}}{E_{tot}}$$

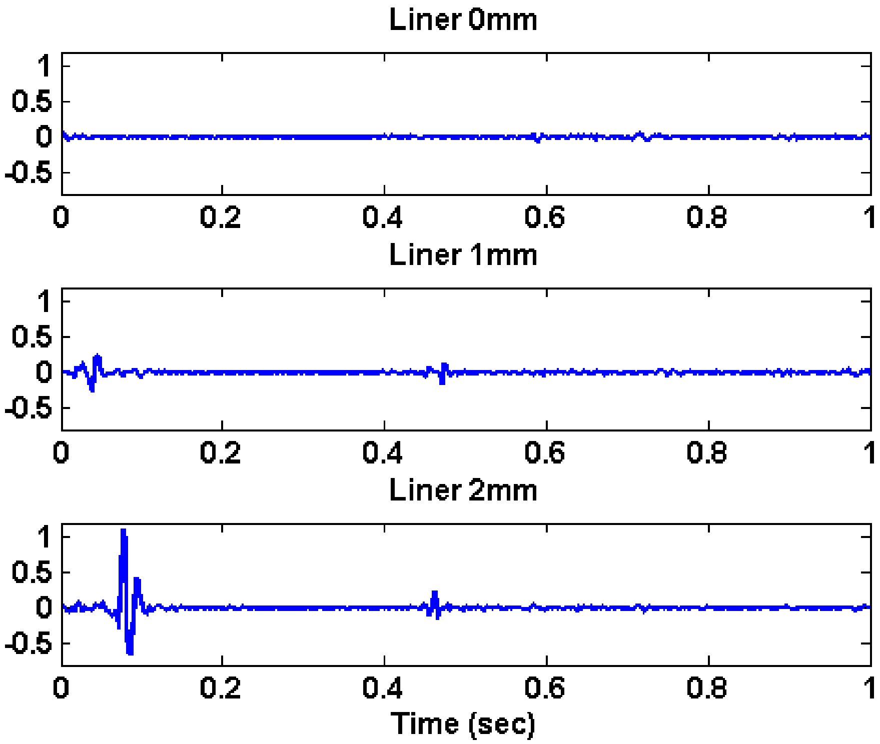

Figure 2.18. The denoised and reconstructed signals from the liner accelerometer enable discriminant features associated with separation to be more clearly identified.

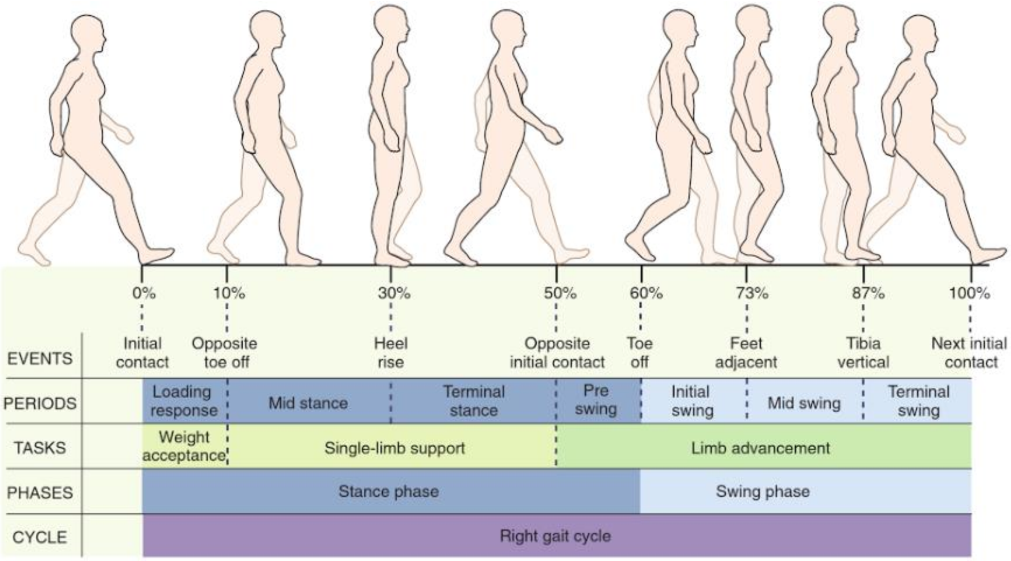

Figure 2.19. Commonly discussed events and periods of a gait cycle were used to segment the vibration data for analysis (illustration courtesy of Neumann's *Kinesiology of the Musculoskeletal System* [76]).

2.4. Results

2.4.1. Dynamic Descriptors of Average Gait Cycles

The average gait cycle was first analyzed for basic dynamic descriptors (

Table 2.3). Distinct impulses were identified during the loading response (0%-10% of gait cycle) on both the liner and the cup holder accelerometers. The liner accelerometer experienced the greatest accelerations due to its proximity to the joint center. This data was used for maximum acceleration (a_{max}) measurements. The maximum velocity (v_{max}) and maximum acceleration occurred during the loading response period for all scenarios. In 1 mm and 2 mm trials, v_{max} and a_{max} occurred within 5 milliseconds of each other and a_{max} occurred after v_{max}. In the 0 mm experiment, 14.8 milliseconds separated v_{max} and a_{max}, and a_{max} occurred before v_{max}. The maximum acceleration data and maximum medial/lateral shift measured experimentally with the LVDT was used to perform a linear regression. The resulting line illustrates the effect that increasing medial/lateral shift has on the maximum acceleration (Figure 2.20). The equation of the line fit to the data is

$$a_{max}(d_{max}) = 10302d - 2470.8$$

In which a_{max} is the maximum raw acceleration logged in a gait cycle, and d_{max} is the maximum shift measured in a gait cycle. This model has a correlation coefficient (R^2) of 0.9848.

2.4.2. Total Energy

All reconstructed signals were analyzed holistically and in segments that commonly describe periods of a gait cycle. Inspection of the total energy as a function of accelerometer position and amount of separation reveals some expected and unexpected patterns. The characteristic pattern is well defined in the liner signal due to its proximity to the joint. The total energy measured at this position increases with increasing amounts of separation (Table 2.4). The same

Table 2.3. Average Maximum Velocity and Accelerations for a One Second Gait Cycle

Measurement	**0 mm**		**1 mm**		**2 mm**	
	Time (sec)	*Magnitude*	*Time (sec)*	*Magnitude*	*Time (sec)*	*Magnitude*
Maximum Velocity (mm/sec)	0.0239	17.235	0.0409	33.452	0.0743	78.283
Maximum Acceleration (mm/sec^2)	0.0091	1464.8	0.0451	5284.5	0.0769	19166

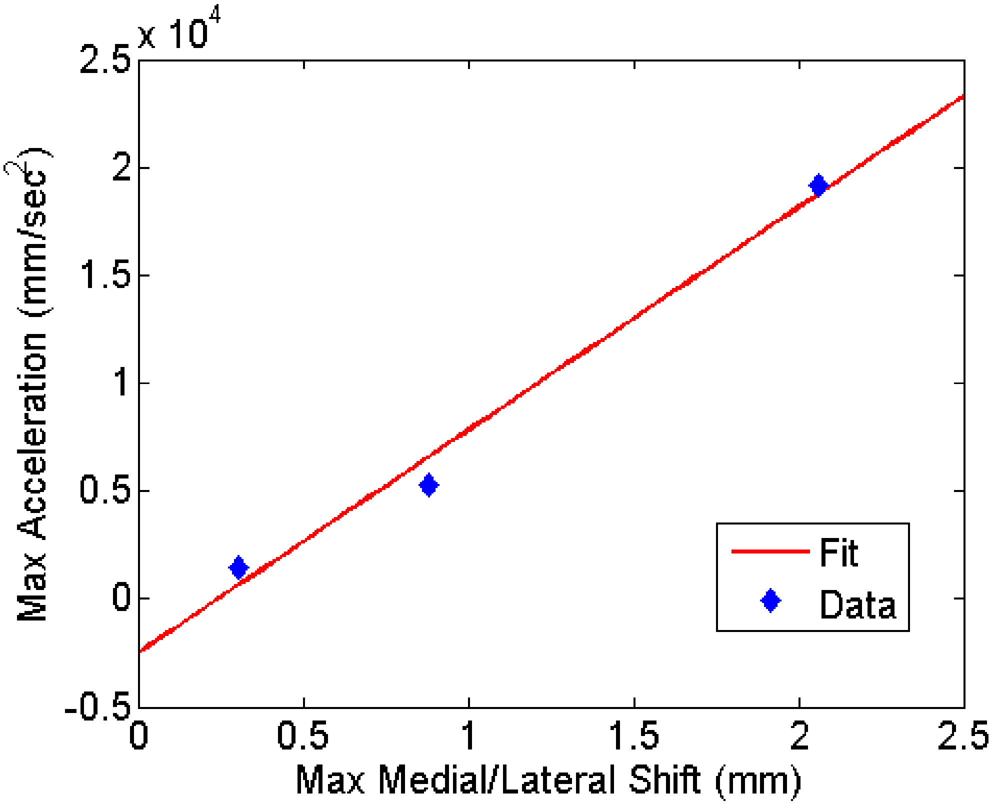

Figure 2.20. The maximum acceleration increases as the maximum medial/lateral shift increases ($R^2 = 0.9848$).

Table 2.4. Total Energy in Average Gait Cycles Measured at Four Locations

Separation	Liner	Cup Holder	Femur ML	Femur SI
0 mm	1.57	1.86	4.37	4.36
1 mm	9.24	4.16	8.19	9.69
2 mm	78.42	12.36	6.90	8.54

pattern is also present in the signal measured at the cup holder although to a lesser extent. The total energy measured at the cup holder for the control is slightly higher than the total energy measured at the liner for the same trial. Total energy measurements conducted at the femur locations do not contain the same characteristic patterns with respect to increasing amounts of separation.

2.4.3. Energy by Gait Cycle Period

To gain a more physiological understanding of the signals, the gait cycle was dissected into seven periods. In these seven periods, the energy was calculated and used to study how the gait cycle and the location of the accelerometer affected vibrations in the presence of an instability (Figure 2.21, Figure 2.22, Figure 2.23). The most extreme scenario (2mm) provides the best insight to the patterns (Figure 2.23, Figure 2.24). The loading response (0-10%) contained the greatest amount of energy for each of the four locations. The following period, mid stance (10%-30%), contained substantially less energy. After mid stance, the liner, cup holder, and femur SI location, experienced increased energy in the terminal stance period (30%-50%). The energy at the liner and cup holder decreased in pre swing (50%-60%), and then remained relatively unchanged for the remainder of the gait cycle. Both femur locations increased energy in the pre swing phase, after which their relative energy fluctuated by smaller amounts through swing phase. Formally, swing phase spans 60% to 100% of the gait cycle and includes three phases (initial swing, mid swing, and terminal swing). During these three phases and the preceding pre swing phase, the energy measured at both femur locations was greater than the energy measured at the liner and the cup holder location (Figure 2.24).

For the control experiment (0 mm) the energy of the reconstructed signal did not exceed 2 units in any period at any of the four locations (Figure 2.21). The energy profiles of the four 1 mm signals (Figure 2.22) were very similar in pattern to their

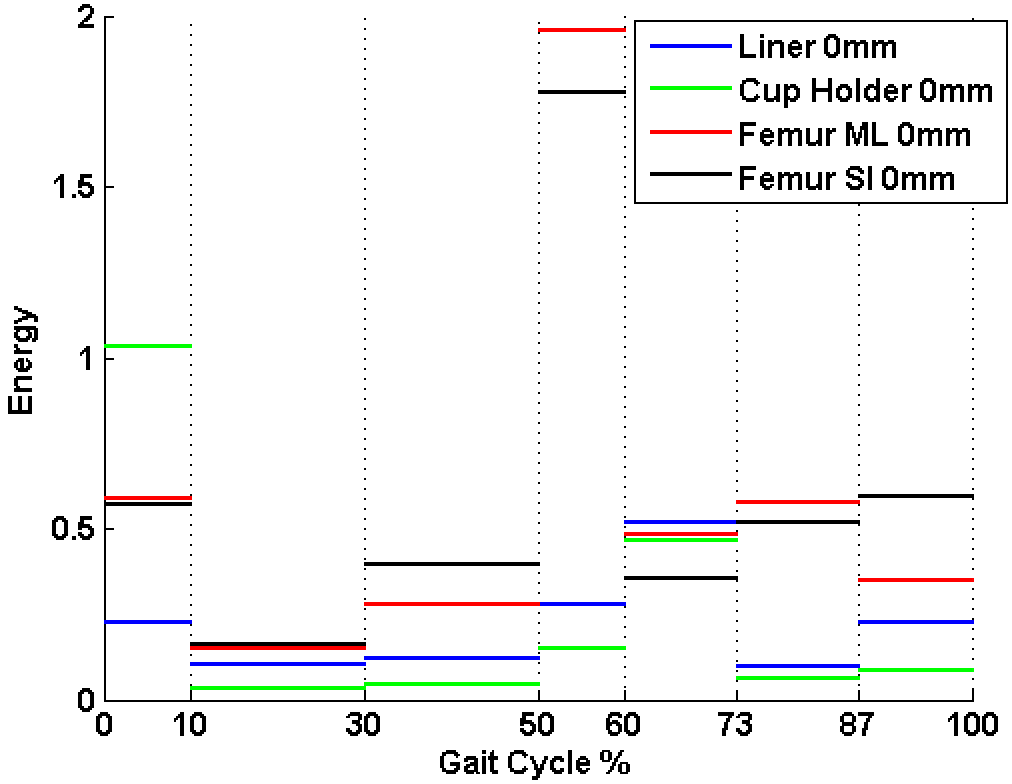

Figure 2.21. The energy measured at four locations in each period of the gait cycle for control conditions.

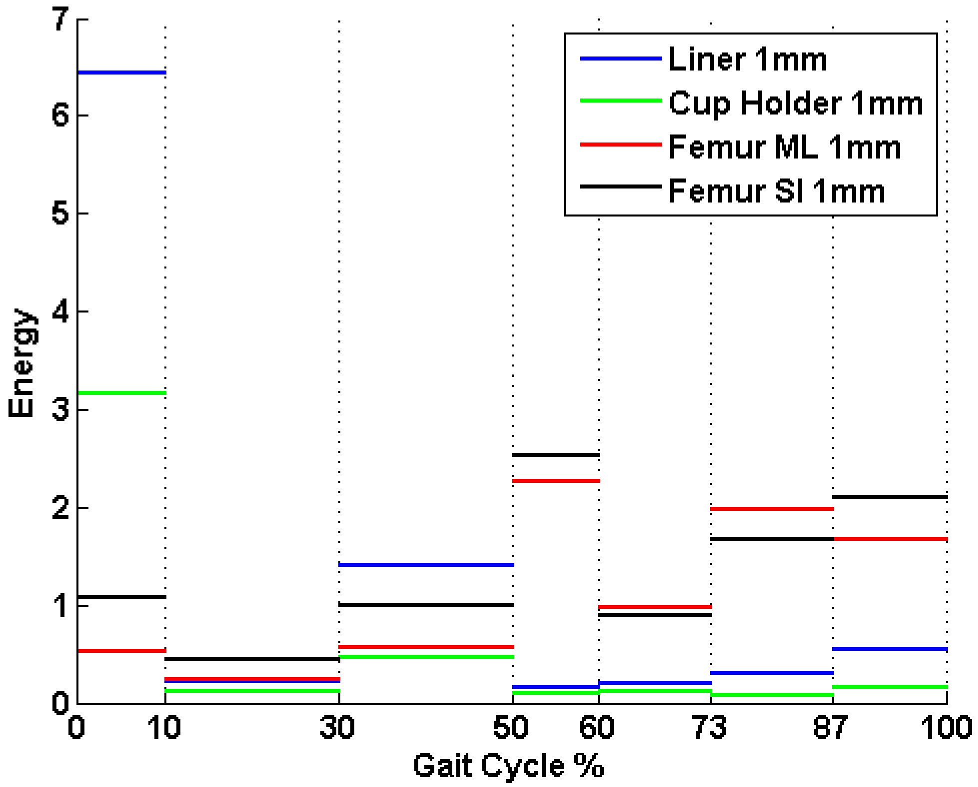

Figure 2.22. The energy measured at four locations in each period of the gait cycle for 1 mm conditions.

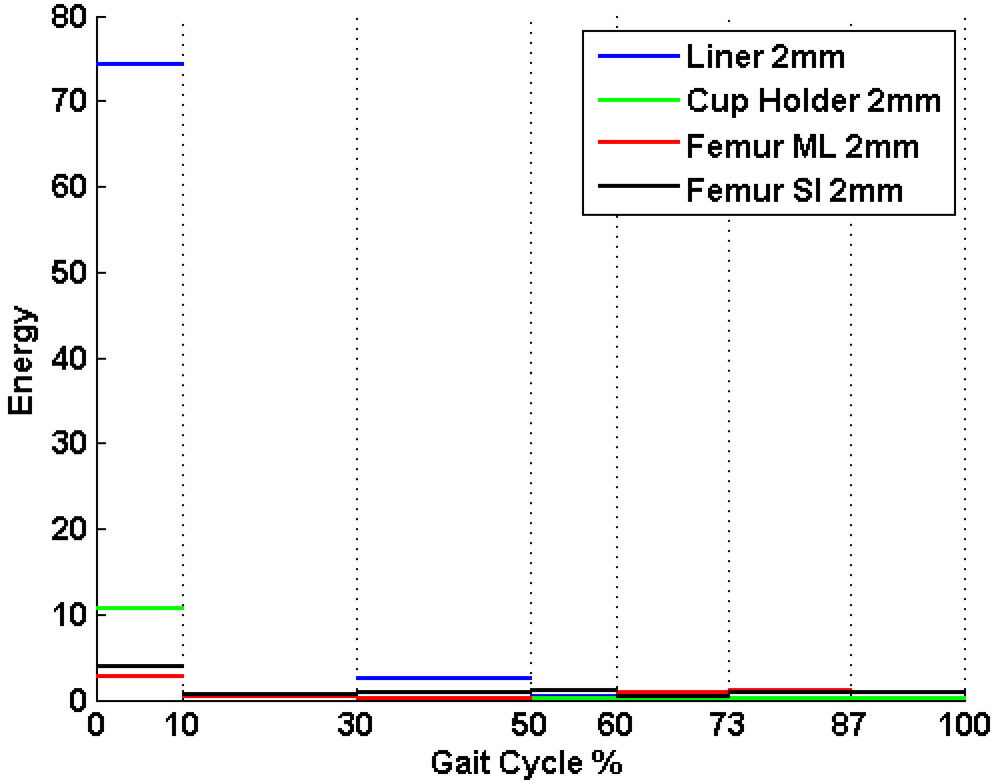

Figure 2.23. The energy measured at four locations in each period of the gait cycle for 2 mm conditions.

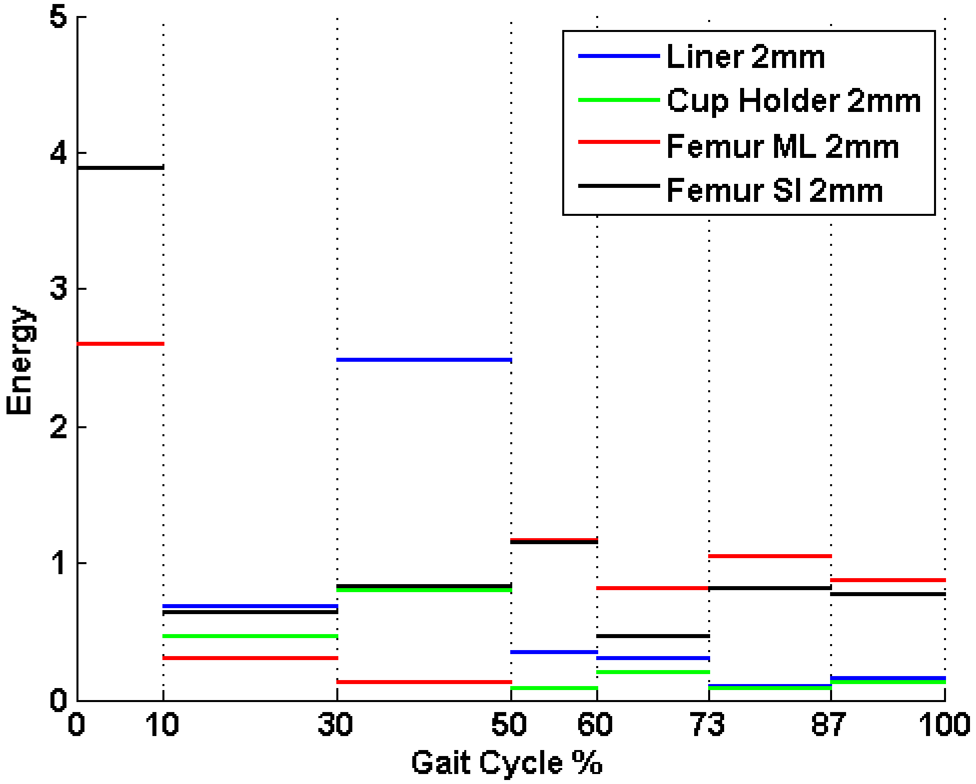

Figure 2.24. The energy measured at four locations in each period of the gait cycle for 2 mm conditions (same data as Figure 22 with zoom applied to energy axis for illustrative purposes).

respective 2 mm signals. As expected, the 1 mm signals were significantly less than the 2 mm signals.

2.4.4. Relative Energy by Gait Cycle Period

The relative energy of each gait cycle period was calculated as a fraction of the total energy measured at each location for the duration of the gait cycle. This metric was used to gauge the differences in energy among experiments for a given transducer location. At the liner, the energy is well distributed across most periods for the control (0 mm) scenario. The initial swing period contains 32.8% of the gait cycle energy while all other periods contain between 6.3% and 17.9%

(Figure 2.25). In cases of separation (1 mm and 2 mm) the energy is more heavily concentrated in the loading response of the gait cycle. At the liner, the loading response contains 69.6% and 94.8% of the 1 mm and 2mm gait cycle energy respectively. After this phase, the relative energy for separation trials remains below 20%. One other period of interest at this location is the terminal stance phase which contains noticeably more energy than its two surrounding periods. During swing phase, the relative energy of the liner is minimal in cases of separation.

Similar to the liner, the cup holder energy is concentrated in the loading response period of the gait cycle for cases of separation (Figure 2.26). For 1 mm and 2 mm of separation the loading response contains 75.9% and 86.0% of the gait cycle energy respectively. One difference for this location, is that more than 50% of the energy for the control experiment is also distributed in this period. After the loading response, the relative energy for the control decreases significantly and only rises above 10% in the initial swing period (60-73%). For cases of separation the relative energy at the cup holder experiences the same rise in energy seen at the liner during terminal stance before reducing again to a minimum in swing phase.

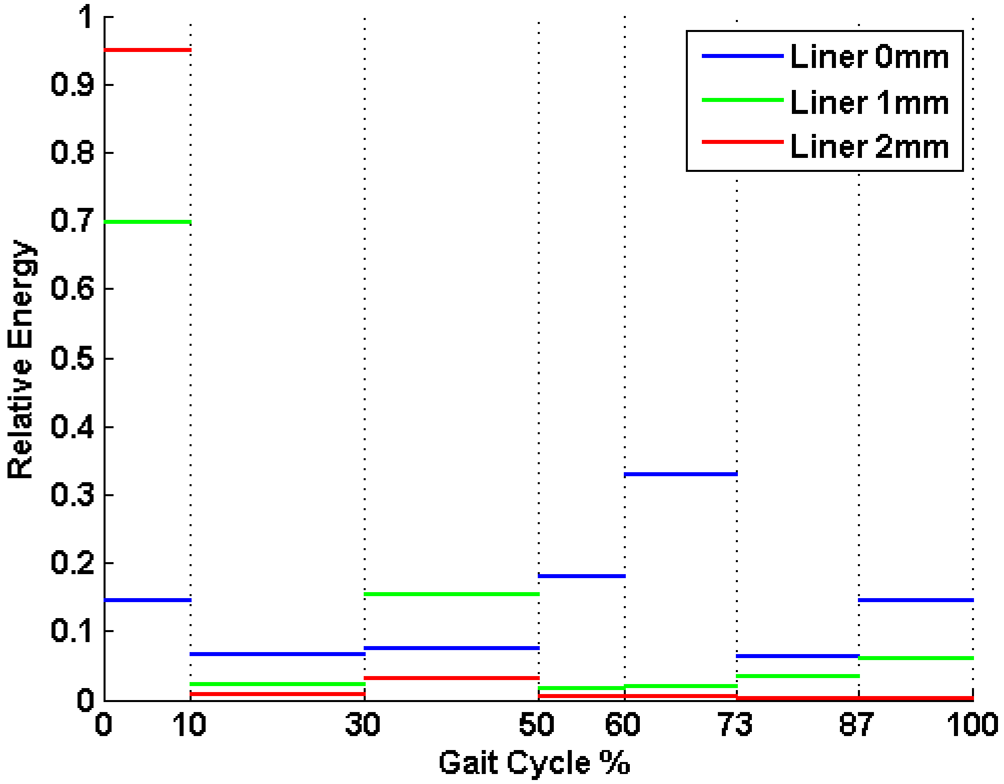

Figure 2.25. The relative energy at the liner illustrates the effects of separation across the gait cycle.

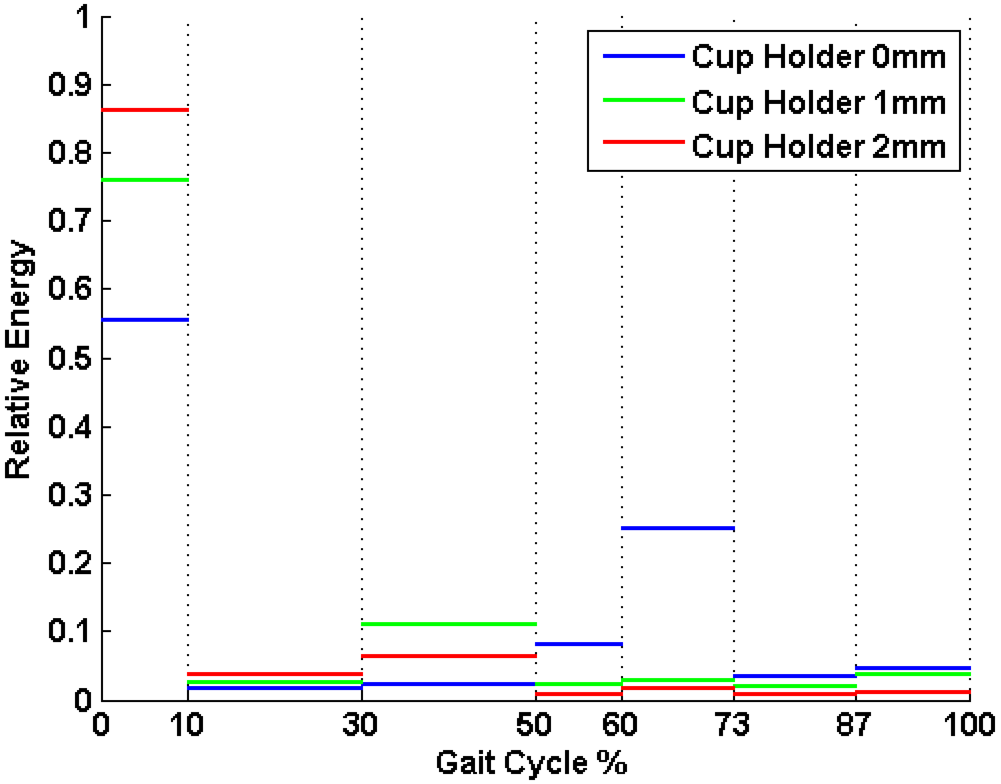

Figure 2.26. The relative energy at the cup holder illustrates the effects of separation across the gait cycle.

In agreement with the liner and cup holder locations, the femur locations registered maximum relative energy in the loading response in the presence of 2 mm of separation (Figure 2.27 and Figure 2.28). The loading response relative energy for 1 mm of separation was actually less than the control for both femur locations. No gait cycle period contained more than 50% of the total energy at either femur location. For 2 mm of separation the relative energy at Femur SI decreased in mid stance, then increased in terminal swing and pre swing (Figure 2.28). The same trend was present in 1 mm of separation and the control scenario. The amount of relative energy between terminal stance and initial swing was characteristic feature of both femur locations for all experiments including the control. The relative energy in this pre swing period is a local maximum for all locations. After pre swing the relative energy decreased, before rising again in mid swing and again in terminal swing period. In the Femur ML location more than 50% of the energy was contained in the pre swing and swing phase periods (50-100%) of the gait cycle for all experiments (Figure 2.27). At the Femur SI location nearly 75% of the energy was contained in the second half of the gait cycle for the control and 1 mm of separation (Figure 2.28).

2.5. Discussion

Total hip arthroplasty is considered a highly successful surgery. However, the increased demand for more functional implants continues to drive innovation. Years of research have demonstrated that instabilities in modern THA do exist, and these instabilities can lead to unintended wear patterns that reduce the longevity of the prosthesis. Diagnosing such instabilities before they compromise the joint may allow for treatments that correct for or mitigate the instability. Currently examination and diagnoses of such minor instabilities is relatively nonexistent. No objective techniques are readily available to physicians and observation of such instabilities is less than convenient. Considering that the

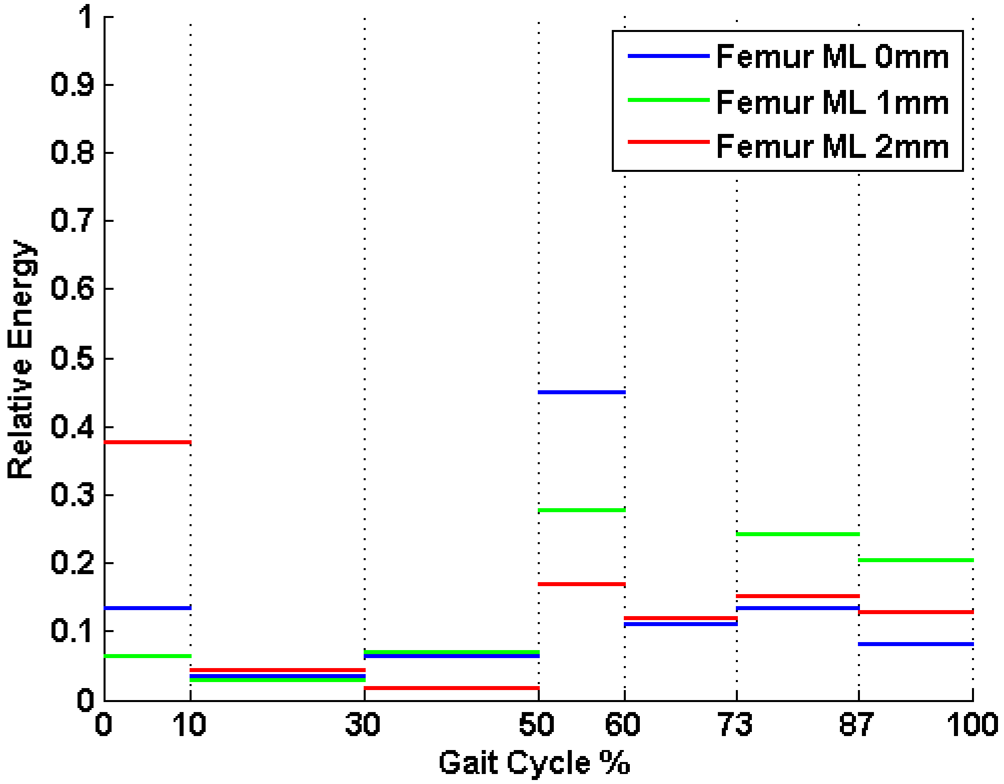

Figure 2.27. The relative energy at Femur ML illustrates the effects of separation across the gait cycle.

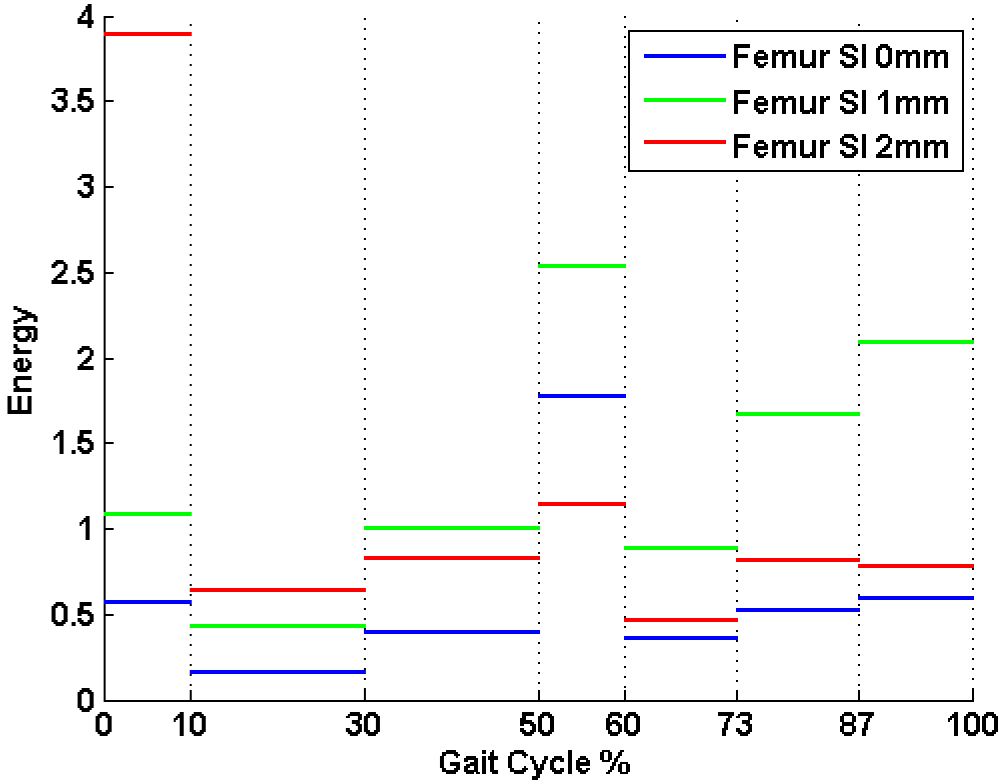

Figure 2.28. The relative energy at Femur SI illustrates the effects of separation across the gait cycle.

instabilities are dynamic in nature, an ideal diagnostic system must monitor the joint through full ranges of motion under various loading circumstances. To date such instabilities have only been accurately identified in patients using fluoroscopy and 3D-to-2D registration techniques for kinematic assessment [44, 60, 61, 77]. In conjunction with such techniques, preliminary investigations of joint sounds or vibrations has been conducted in vivo using laboratory grade instrumentation [36, 37]. Findings suggest that vibrations measured at the skin surface can provide discriminatory data that correlate with translational instabilities in THA. Specifically, Glaser et al. reported the presence of characteristic transients that correlated with relocation following instances of separation in different types of THA [36]. Before proceeding any further with in vivo work, it is essential to characterize the phenomenon in a more controlled environment. Such an environment enables comparison of vibrations as they relate to magnitudes of separation and transducer location. The current work examines the vibrations associated with hip separation in a mechanical hip simulator. Through this work, the characteristic features associated with hip separation were assessed with respect to standard periods of a gait cycle. The results provide metrics and patterns that can be included in future research methodologies, thus advancing the orthopaedic community’s capability to noninvasively diagnose THA instabilities.

In the current work accelerometers positioned at four different locations on the hip simulator for three different magnitudes of separation were used to log raw vibrations during gait. The simulator itself, induced substantial noise in the signals that was removed through wavelet decomposition, coefficient thresholding, and reconstruction. A previous in vivo investigation on THA sounds and vibrations describes thresholding detail coefficients based on the detail level variance [36]. Unlike in vivo experiments, in the present work, multiple levels of the wavelet decomposition were highly corrupted by simulator noise. The present methods committed to a more absolute thresholding technique in which only coefficients from the level 6 and level 7 details were used for signal reconstruction. Together these levels are associated with a bandwidth that ranges from approximately 39 Hz to 156 Hz (Table 2.2). Previous work suggests that the characteristic vibrations associated with micro-separation may exists in this frequency band [67]. Sariali et al. constructed a computational model of the Leeds II hip simulator under normal and micro-separation conditions. They reported that in the presence of 500 μm of separation a distinct chatter existed between the femoral head and the acetabular cup during swing phase. The main frequency of this chatter was 65 Hz [67]. Although the work here more distinctly characterized the reduction of the femoral head following separation, certain features do point towards correlations of the vibrations with the occurrence of separation in swing phase. As previously mentioned in the methods, a measurable medial/lateral shift of the cup holder (0.2975 mm) was logged by the LVDT in the control experiment. This shift initiated during the pre swing period at approximately 56% of the gait cycle and peaked towards the end of the following period (initial swing) at ~68% of the gait cycle (Figure 2.29). The primary shift in 1 mm and 2 mm experiments also initiated during the pre swing period. The energy in this period of the gait cycle is quite distinguishable for both femur locations during all experiments. For the control experiment, Femur ML and Femur SI register more energy in this period than any other period. Furthermore, because the control does not experience an aggressive reduction of the femoral head in the loading response, these energy magnitudes at the femur are greater than all liner and cup holder values (Figure 2.21). For 1 mm of separation the energy at these sites during pre swing increases, and similarly it is a local maximum. Aside from the liner and cup holder energy in the loading phase (associated with reduction of the femoral head), these femur energy levels are greater than all other energy measurements (Figure 2.22). In the presence of 2 mm of separation the femur sites experience maximum energy in

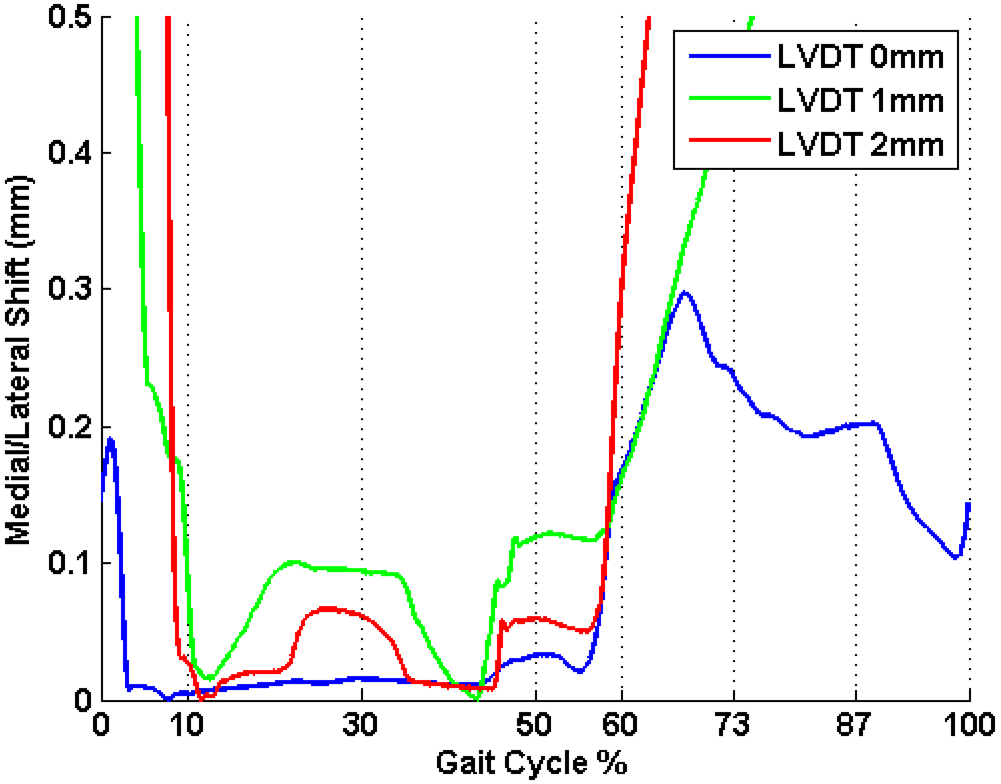

Figure 2.29. The medial/lateral shift recorded by the LVDT (zoomed in for illustration purposes).

the loading response. The next highest energy for the femur sites is in the pre swing period. The maxima and local maxima in energy experienced at the femur locations in conjunction with the shifts present in the LVDT data demonstrate that vibrations associated with the shift can be measured and recognized. It is likely that these vibrations are similar to the chatter between the femoral head and cup previously described by Sariali et al. [67].

As the amount of medial/lateral shift increases, the liner and cup holder signals become dominated by the large transient associated with relocation of the femoral head in the loading response (Figure 2.30, Figure 2.31, Figure 2.32, Figure 2.33). As expected, the energy at the liner during the loading response is substantially greater than the absolute energy at the cup holder for 1 mm and 2 mm of separation (Figure 2.22 and Figure 2.23). This can be attributed to two factors: 1) proximity to the joint center and 2) axial orientation of the accelerometer. Although the first is obvious and requires no additional discussion, the second is worth describing in further detail. The accelerometer on the liner is mounted at an angle such that its axial direction has both medial/lateral and inferior/superior components. As loading is reintroduced to the system, the cup holder moves inferiorly and laterally to relocate at centered conditions. The axial direction of the liner accelerometer is nearly identical to the direction of relocation and impact. Thus, it is more adequately oriented to measure the vibrations than the cup holder accelerometer which is positioned such that its axial direction is purely medial/lateral. Aside from the transient associated with relocation of the femoral head following separation, the liner and cup holder signals are characterized by a second smaller transient in the terminal stance phase of the gait cycle (30-50%) (Figure 2.30, Figure 2.31, Figure 2.32, Figure 2.33). During this period, there is a preliminary medial/lateral shift present in the LVDT data for all experiments (Figure 2.29). For 1 mm and 2 mm experiments, the end of this shift coincides with a

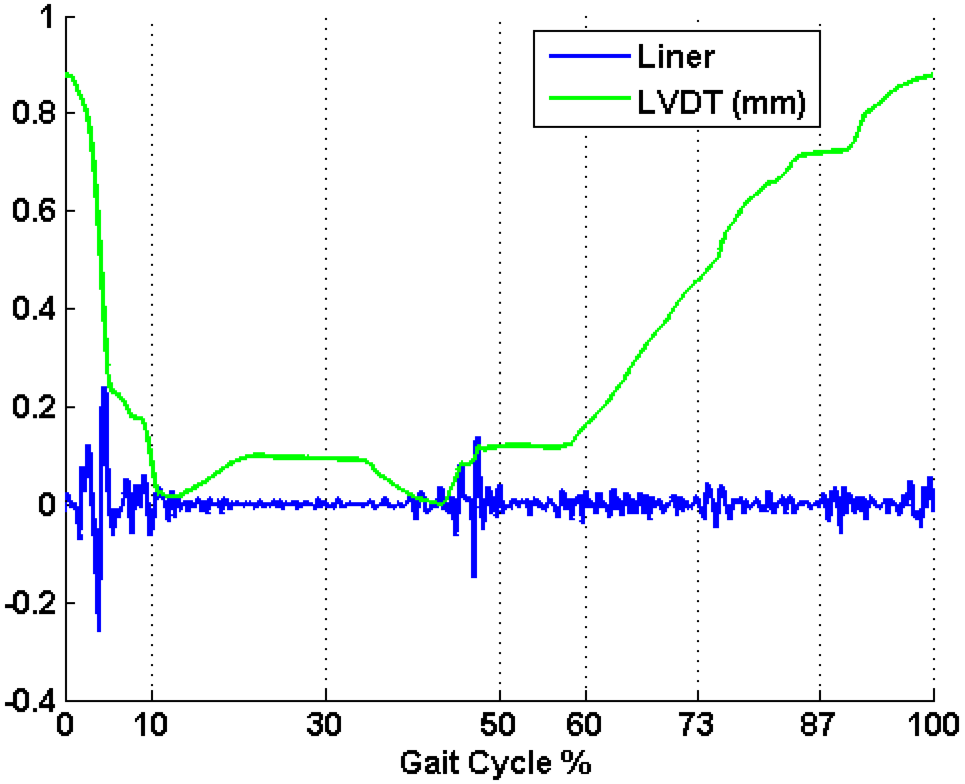

Figure 2.30. The reconstructed liner signal for 1 mm of separation is characterized by two distinct transients in the loading response (0-10%) and terminal stance (30-50%) periods of the gait cycle.

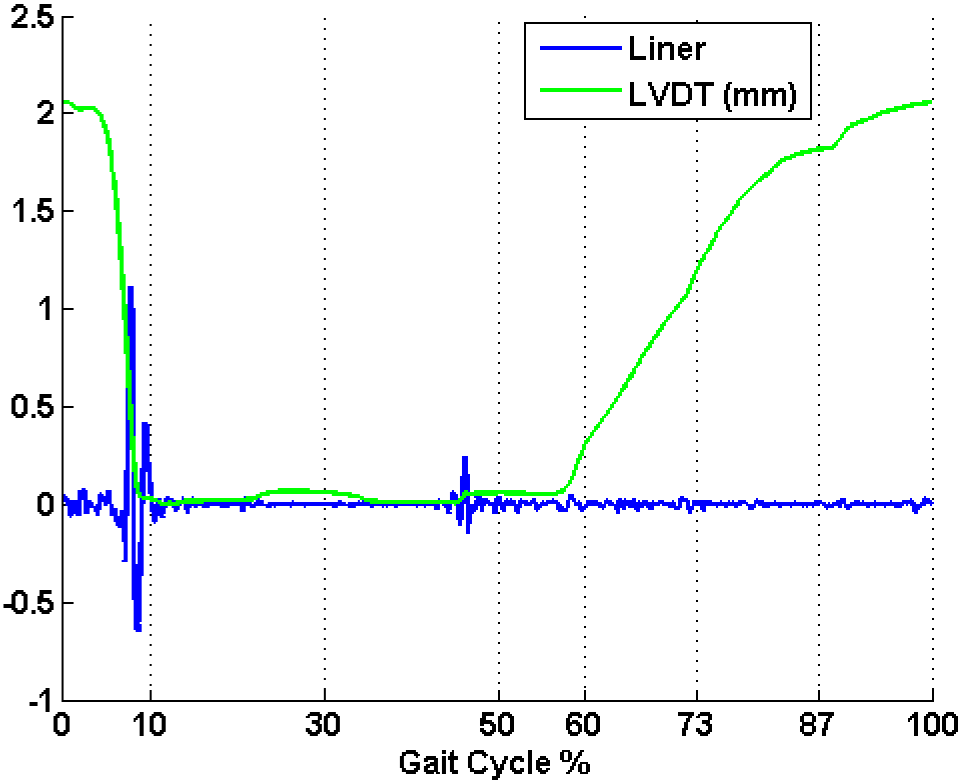

Figure 2.31. The reconstructed liner signal for 2 mm of separation is characterized by two distinct transients in the loading response (0-10%) and terminal stance (30-50%) periods of the gait cycle.

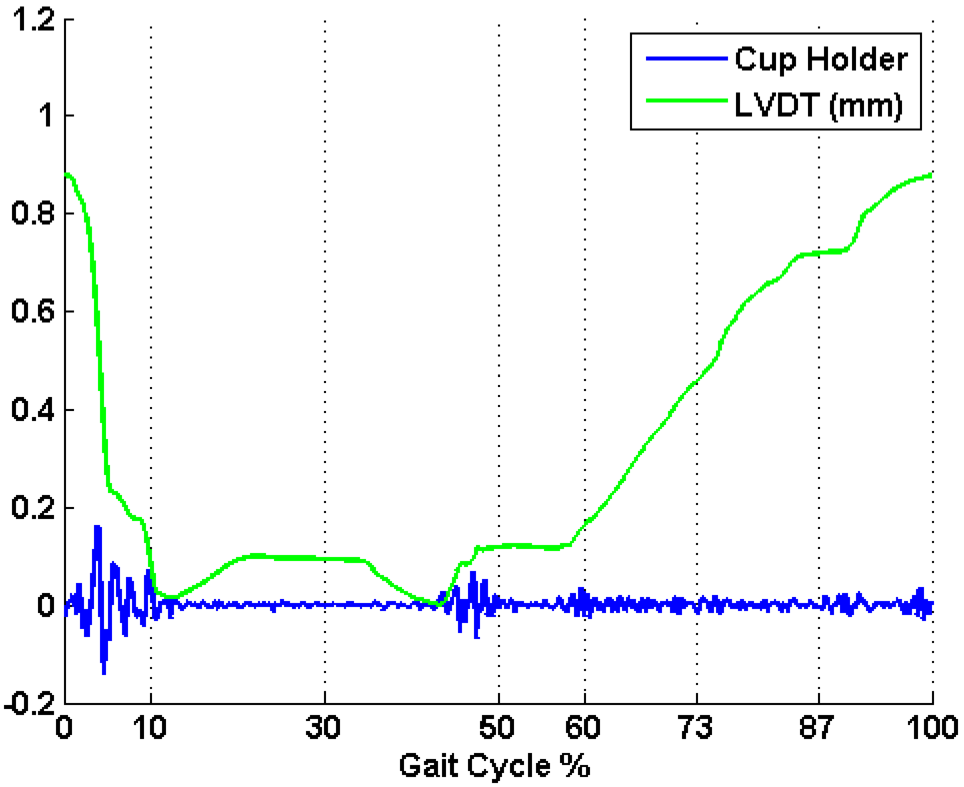

Figure 2.32. The reconstructed cup holder signal for 1 mm of separation is characterized by two distinct transients in the loading response (0-10%) and terminal stance (30-50%) periods of the gait cycle.

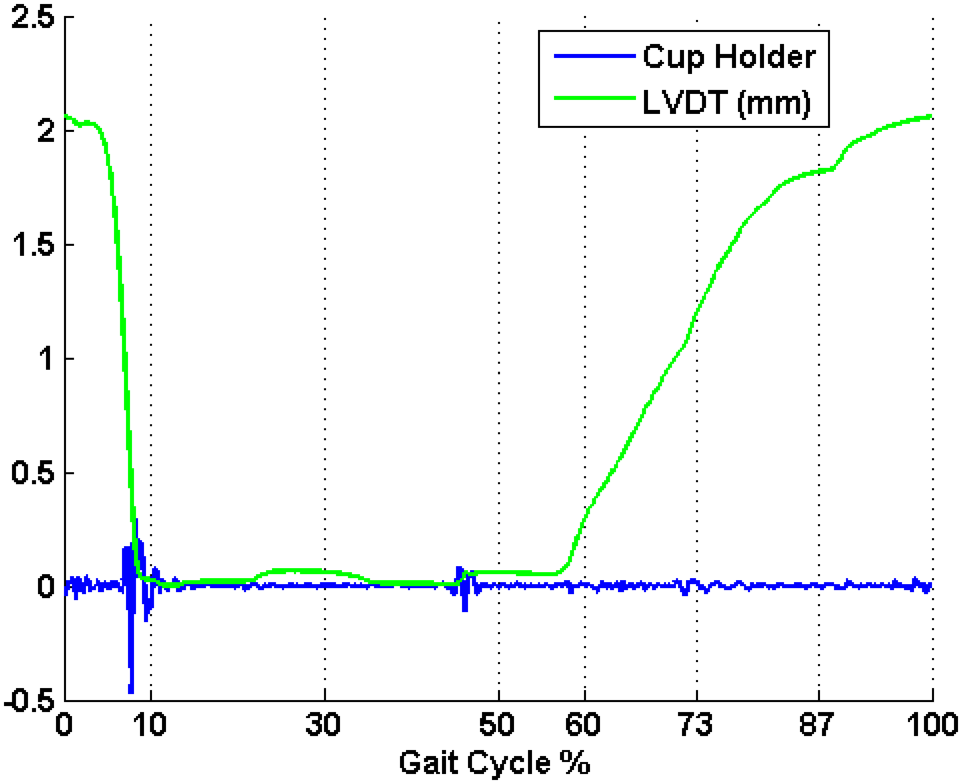

Figure 2.33. The reconstructed cup holder signal for 2 mm of separation is characterized by two distinct transients in the loading response (0-10%) and terminal stance (30-50%) periods of the gait cycle.

distinct transient of interest. This suggests that as the load on the cup holder begins decreasing, a small abrupt shift occurs that results in some type of impact between the femoral head and the acetabular liner. It is believed that the spring force in combination with the load and kinematics of this period causes the femoral head to slip with respect to the acetabular liner resulting in a dynamic singularity that is punctuated by a measurable impact. The existence of this transient is further highlighted by a local maximum in the relative energy profiles of the respective liner and cup holder signals Figure 2.22 and Figure 2.24.

Despite the existence of this preliminary shift in the 0 mm LVDT data, the transient vibration is nonexistent. The absence of a distinguishable transient in both the loading response and terminal stance phase of the 0 mm experiment provides valuable insight to the sensitivity of the instrumentation as intended for diagnostic purposes. In the presence of ~300 μm of medial/lateral shift the impacts are not measurable in the current set up, and thus, such a small instability cannot be detected with this instrumentation.

Comparison of the energy with respect to the two major aspects of the simulator (acetabular region vs femoral region) further demonstrates the importance of accelerometer positioning. As previously mentioned the two most distinct characteristics associated with impacts following medial/lateral shifts were easily identified in the liner and cup holder signals. The prominence of these patterns caused most of the acetabular region (liner and cup holder) energy to be concentrated in the stance phase of the gait cycle. Indeed, swing phase energy was relatively negligible for the signals originating from the acetabular region of the simulator. This was not the case for the two femur accelerometers. On the contrary, the signals from the femur locations concentrated more energy in the swing phase of the gait cycle than in the stance phase. This suggests that the femur accelerometers registered signals associated with the gradual separation itself, but not as much with the relocation. Such signals are lower in magnitude and more dispersed over consecutive periods of the gait cycle as coverage of the femoral head decreases. The decrease in coverage results in decreased EHL of the joint. This causes increased friction that manifests itself in chatter-like vibrations as the femoral head articulates against the rim of the acetabular liner. It appears that having accelerometers on each body (femur and acetabulum) is important as they provide distinctly different characteristics that can be used together to confirm the presence of a translational instability similar to that simulated here.

There are numerous limitations associated with this work. Most importantly, the results presented are subject to the representation of the hip simulator, and although it has been validated to reproduce relevant wear rates and patterns, it is not a human joint. This fact allowed for accelerometers to be positioned closer to the joint than possible in vivo. Additionally, this rigid simulator allowed for enhanced transmissibility of vibrations that cannot be expected in vivo. Adipose tissue, muscles, and the ligamentous sheathe surrounding the hip joint will all attenuate and likely alter the signal of interest such that the methods presented here may not be perfectly tuned for detecting instabilities in such an environment. Lastly, these experiments were conducted in a single configuration. They do not account for changes in loading, cadence, or other variables that are different patient to patient and they do not test the effect of surgical variables that are known to affect coverage such as inclination and anteversion.

2.6. Conclusion

This initial investigation provided an excellent opportunity to define a set of methods that can be used in the future to investigate the vibrations emitted from a hip joint simulator and/or native hips with more focus. This work demonstrated the feasibility of using surface-based vibrations to quantify translational instabilities with respect to periods of the gait cycle. It was found that a medial/lateral shift less than 1 mm results in at least one, if not two, measurable impacts during stance phase. It was also found that increases in medial/lateral shift can be detected and differentiated from each other. Lastly it confirmed the importance of monitoring both femoral and acetabular components separately as they provide distinctly different characteristics that can be used to confirm the presence of an instability. Future simulator investigations should study the effects that load, cadence, implant configuration, and implant type has on vibration signatures. In vivo investigations of this nature still require fluoroscopy to validate any suspected findings present in vibration data. Accelerometer positioning and fluoroscopic frame selection are critical factors for an in vivo investigation of THA instability. Ideally accelerometers would be positioned at bony landmarks to optimize transmissibility. The greater trochanter of the femur and the medial anterior aspect of the iliac crest are appropriate candidates for mounting sites. Fluoroscopic frames should be selected at the eight standard events of the gait cycle, and the kinematics of the femoral head with respect to the femur should be defined within the standard gait cycle periods. Using the analysis methods presented here, correlations between observed kinematics and signal energy may further demonstrate the potential of vibroarthrography for diagnosing THA instabilities.

CHAPTER 3. MEASURING CAM-POST ENGAGEMENT IN POSTERIOR STABILIZED TKA WITH VIBROARTHROGRAPHY

Raw data for this research was collected at the Porter Adventist Hospital in Denver, Colorado by Trevor Grieco and Mathew Anderle. All final analyses were conducted by Trevor Grieco at the University of Tennessee. Computer aided design models of the Attune® Posterior Stabilized Fixed Bearing total knee arthroplasty system were provided by DePuy Synthes for analyses. Annotated images of these models are presented in multiple figures throughout this chapter for illustrative purposes.

3.1. Abstract

In a posterior stabilized TKA, a cam-post mechanism is used to substitute for the posterior cruciate ligament. This mechanical substitute can heavily dictate the dynamics of a replaced knee and thus its performance is of interest to manufacturers, surgeons, and patients alike. Unfortunately, it is difficult to quantitatively assess cam-post engagement under in vivo conditions. Current techniques are strictly limited to fluoroscopic analyses. While accurate, such analyses are not easily conducted and expose subjects to ionizing radiation. A previous qualitative investigation has suggested that the cam-post engagement confirmed under fluoroscopy may be associated with characteristic vibrations that can be measured at the knee surface. Additionally, it appeared that the differences in contact mechanics resulted in differences in the vibrations. The present work was designed to explore the quantitative relationships between fluoroscopically confirmed cam-post engagement and features derived from mechanical vibrations to determine if vibroarthrography could be used as a reliable noninvasive tool for assessment of this mechanical interaction.

Three assessments were conducted in 9 total knee arthroplasties to determine if 1) vibration features could predict the time of cam-post engagement, 2) vibration features were correlated to cam-post engagement velocity, and 3) vibration features were correlated to cam-post engagement height. Envelope amplitude and variance outperformed all other features in predicting the time of engagement. The median error for both features was 0.630 seconds. Variance, mobility and form factor all demonstrated considerable correlation to cam-post engagement velocity. Variance, crest factor, peak-amplitude-to-power ratio, and envelope amplitude demonstrated mild correlation to cam-post engagement height.

The vibration features and dynamic variables assessed in this pilot research highlight the shortcomings and the potential of vibroarthrography for the

assessment of cam-post engagement in posterior stabilized total knee arthroplasty.

3.2. Introduction

The posterior cruciate ligament (PCL) is one of the primary anatomic structures that contributes to the anterior-posterior (AP) stability of the tibiofemoral joint. It originates from an area along the medial femoral condyle within the intercondylar notch and inserts on the posterior aspect of the proximal tibia [78]. The PCL is the largest of the intra-articular ligaments and biomechanically functions to prevent posterior tibial translation. Its contribution to the rotational stability of the joint remains unclear and is a point of contention amid the biomechanics community [78]. During a posterior cruciate sacrificing TKA, the surgeon elects to excise the PCL. This may be done because the ligament is compromised, or because of surgical preference. In fact, supporters of this technique argue that the PCL in a degenerative knee is histologically compromised and that properly balancing the PCL in a manner that will preserve its ideal biomechanical characteristics is difficult [79]. In such a case, the ligament is mechanically substituted for by design features of the TKA. Two common methods of PCL substitution include 1) the cam-post mechanism and 2) highly congruent, deep dish bearings with anterior buildup [80]. These designs are similar in that they both effectively prevent anterior translation of the femur on the tibia and encourage posterior positioning of the femoral component. In the cam-post design, the reaction forces associated with engagement of the mechanism facilitate rollback of the femoral component. In the deep dish design, no such forces exist, but the dwell points are positioned 4-6 mm posterior to the tibial midline which results in a posterior femoral resting position [80]. The advantages and disadvantages of these two designs are well documented in the literature, and exploration of these is outside the scope of the present research. What is of interest, is the nature of cam-post engagement and its correlation to vibrations measured at the skin surface.

PCL substitution via a cam-post mechanism, commonly described as *posterior stabilized*, was first implemented in 1976 by John Insall and Al Burstein [79]. The prosthesis they designed, the Insall-Burstein prosthesis (IB I), was intended to address posterior subluxation and instabilities observed in other prosthesis at that time. The IB I consisted of an intercondylar femoral cam that engaged with a centralized tibial post at approximately 70 degrees of knee flexion. With increasing knee flexion, the femoral cam essentially climbed the tibial post which promoted posterior motion of the tibiofemoral contact points [79]. First implanted in 1978, the IB I effectively substituted for the PCL and demonstrated exceptional success and durability [79].

Today, posterior-stabilized (PS) TKAs are offered by most manufactures and include differences in cam-post geometry intended to optimize the biomechanical performance of the prosthesis. Some primary variables at the tibial post include AP position, post height, ML width, ML symmetry, and curvature associated with mechanism conformity (Figure 3.1). At the femur the dimensions of the box and post cutout as well as the position and curvature of the cam are may affect the biomechanics of the mechanism (Figure 3.2). These features will directly affect the knee flexion angle at which the mechanism engages, as well as the nature of the initial contact and the mechanism's subsequent interaction. Additionally, inappropriate design of these features may lead to dislocation of the joint, unintended wear, and even breakage of the tibial post [79].

Cam-post kinematics and kinetics have been studied via combinations of in vitro, in vivo, and in silico techniques [81-89]. Dynamic variables of interest specific to the mechanism include the knee flexion angle at engagement, SI and ML position

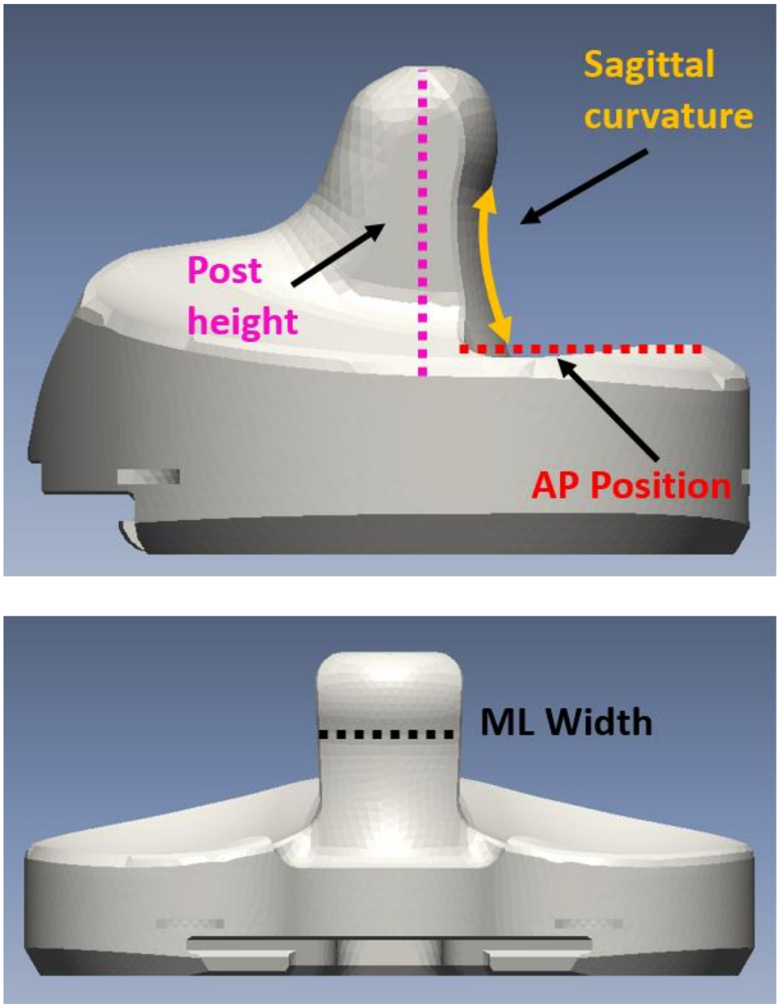

Figure 3.1. Design features of the tibial post in a posterior stabilized TKA.

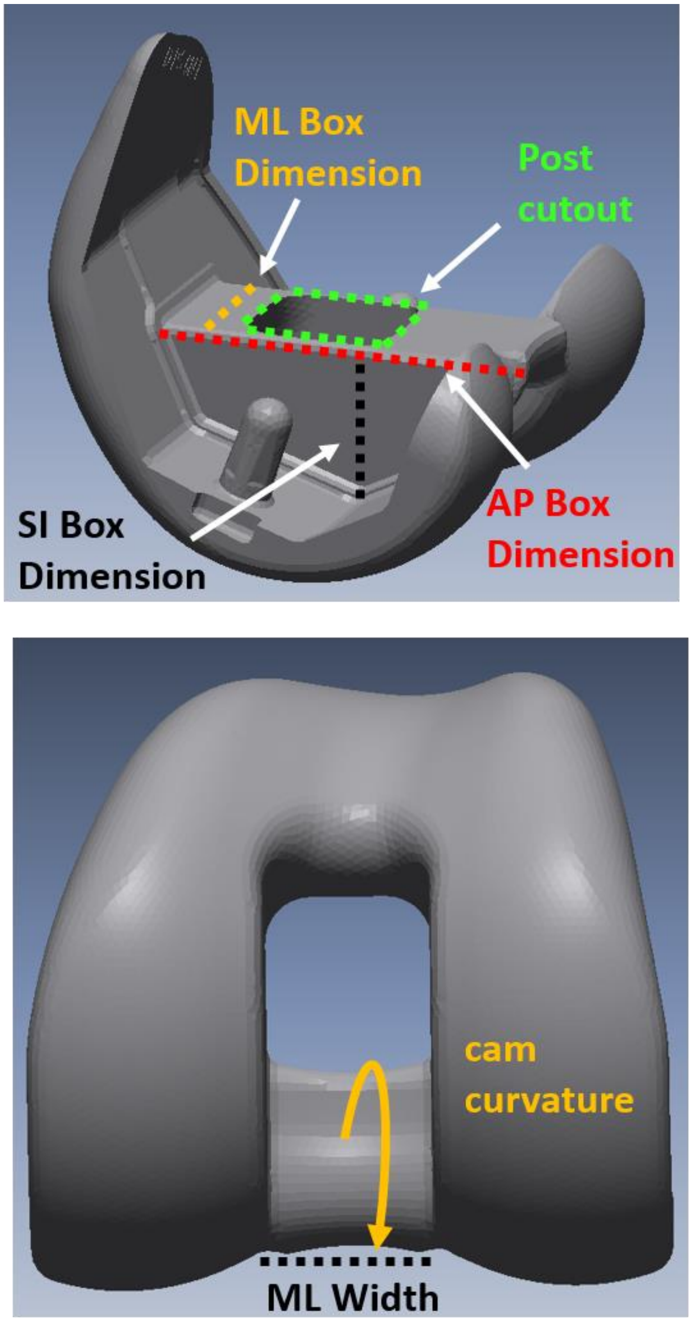

Figure 3.2. Design features of the femoral box and cam in a posterior stabilized TKA.

of the cam on the post, contact area between the cam and post, contact stress (or pressure), impact velocity, and resulting tibiofemoral kinematics such as axial rotation and AP translation of the medial and lateral tibiofemoral contact points. Cam-post contact area and contact pressure have been reliably reported during in vitro simulations using digital pressure sensors [82, 89]. These variables have also been evaluated using validated finite element models [84, 86]. In vivo investigations of cam-post engagement to date have been limited to fluoroscopic evaluations coupled with 3D-to-2D registration techniques [81, 83, 85, 87, 88]. These evaluations typically utilize a threshold to approximate contact between the cam and post as kinematics are interpolated between overlaid frames of interest. Most recently a distance between the cam and post that was less than 0.5 mm has been utilized to define contact [85, 88].

It is mechanically reasonable to consider that some of these dynamic characteristics may be correlated to the vibrations produced as the cam engages with the post. In particular, the impact velocity and nature of the contact area at impact can be expected to affect the magnitude and frequency of vibrations. Relationships between cam-post engagement and vibrations has previously been presented and described in a qualitative manner [38], but no quantitatively significant data has yet been reported. Therefore, the nature of this investigation was to compare relationships between vibrations measured at the skin surface and cam-post mechanics measured in vivo via fluoroscopy and 3D-to-2D registration. The methods and results provide guidance for the future use of vibroarthrography in the determination and quantification of cam-post engagement mechanics.

3.3. Materials and Methods

3.3.1. Patient Demographics

This pilot investigation sought to evaluate the in vivo dynamics of cam-post engagement in posterior-stabilized TKAs in relation to surface vibrations measured at the knee. Subjects implanted with a modern PS fixed bearing TKA (Attune®, DePuy Synthes, Warsaw, IN, USA) were recruited for this study. All subjects were implanted by a single surgeon using a gap balancing technique. To meet eligibility requirements enrolled subjects were at least six months post-operative, had a BMI of less than 30, demonstrated passive flexion greater than 100°, and had Knee Society Functional Scores greater than or equal to 90. Nine knees were evaluated, and appropriate institutional review board approval was obtained along with the informed consents for all subjects participating in the study.

3.3.2. Vibroarthrography Configuration

Three uniaxial accelerometers (352A24, PCB Piezotronics Inc., Depew, NY, USA) were used to measure the vibrations at the knee. These accelerometers are high sensitivity, miniature, integrated electronic piezoelectric (IEPE) accelerometers with a sensitivity of 100 mV/g, a measurement range of ±50 g pk, and a frequency range of 0.5 to 10000 Hz (±5%). The accelerometers were connected to a battery powered signal conditioner (480B21, PCB Piezotronics Inc., Depew, NY, USA) that provides constant-current power to connected sensors. The signal conditioner was configured to amplify all incoming signals by a factor of 10. Signal conditioner outputs were connected to a portable data acquisition device (DataLOG MWX8, Biometrics, Ltd. UK) that was used to log analogue inputs. An electrogoniometer (SG 150, Biometrics, Ltd. UK) and a custom-made synchronization light box (sync light) were also connected to the data acquisition device. The electrogoniometer was used to measure knee flexion/extension (this data was not relied on as a primary feature but more as a high-level indicator of the activity motion). The synchronization light box was used to synchronize fluoroscopy data with the analogue signals logged by the portable data acquisition device. This light box housed a small battery powered circuit with a radio frequency receiver and an LED light that was remotely triggered at the start and end of data collection to effectively mark the activity within a data acquisition file and in a live video. The accelerometer signals were each sampled at 10,000 Hz. The electrogoniometer and sync light were sampled at 1000 Hz. All data was saved onboard the data acquisition device to a micro SD card. The signal conditioner, data acquisition device, and light box are all stored in/on a pack that is worn around the subject's waist. Signals were transferred via Bluetooth to a laptop at a reduced sampling rate for visualization purposes during data collection. This setup is entirely wearable/portable and leaves the patient free to perform the research activity without being tethered to a workstation (Figure 3.3). All subjects were asked to wear shorts to ensure that no noise was introduced to the signals from clothing brushing against the sensors. Shorts were provided if necessary. The waist pack containing the data acquisition instrumentation was then secured to the subject, and the knee was cleaned with an alcohol swab to remove any residue/lotion that may have compromised the adhesion of the sensors to the skin. Accelerometers were then mounted to the patella, tibial tuberosity, and medial femoral epicondyle with hypoallergenic medical tape (Figure 3.4). The sensor cables were also taped above the knee. The entire knee was then wrapped with foam underwrap from below the knee to above the knee to minimize sensor movement and reduce signal artifact that may have occurred during the research activity. Next, the digital goniometer was zeroed using a straight edge and attached to the lateral side of the knee using double sided hypoallergenic tape. Best efforts were made to align the distal end block with the ankle joint and proximal end block with the hip joint to best approximate the anatomic hip-knee-ankle angle. A test was then conducted in which all signals were inspected in real time at the laptop workstation while the subject flexed and extended the knee. Any oddities or signal overloads resulted in inspection of connections/instrumentation and additional testing to ensure data was being appropriately captured prior to collecting data for the primary research activity.

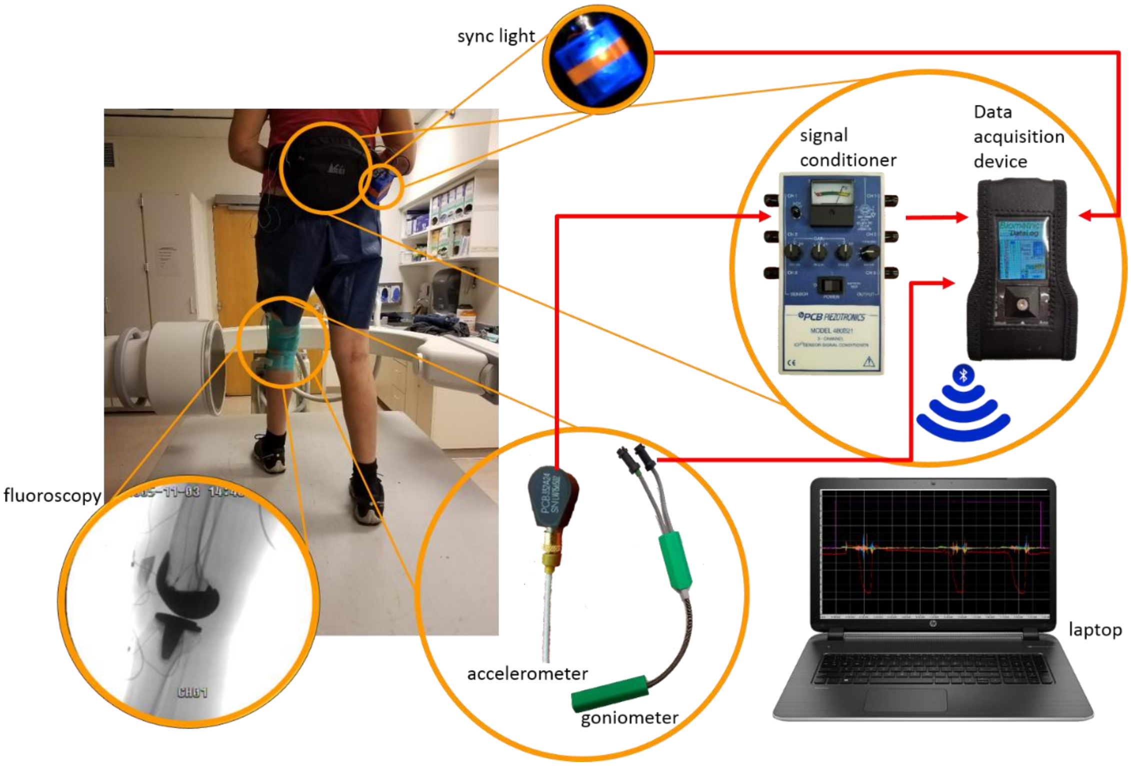

Figure 3.3. Data collection instrumentation and configuration for the analysis of fluoroscopy and vibration signals.

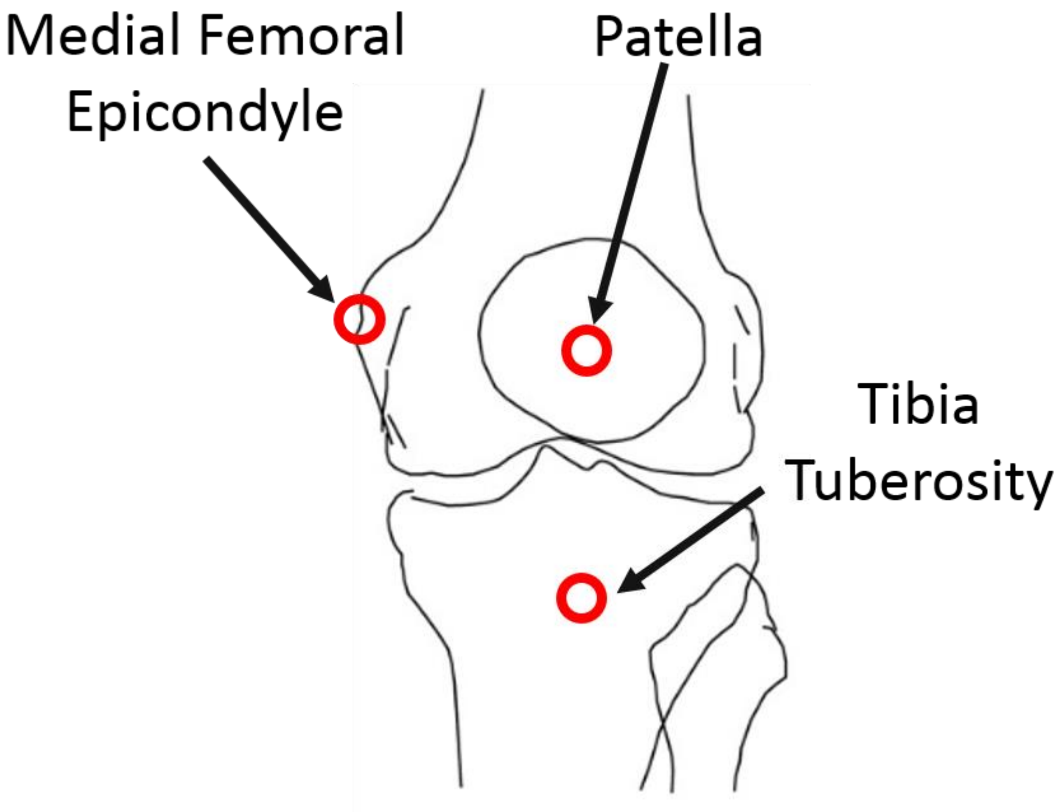

Figure 3.4. Accelerometers (denoted by red circles) were mounted at the medial femoral epicondyle, the patella, and the tibial tuberosity.

3.3.3. Fluoroscopy and Vibroarthrographic Data Collection

A c-arm fluoroscopy unit was used to image the subject's index knee while performing a weight-bearing deep knee bend (DKB). During this activity subjects flex the knee from maximum extension to maximum flexion. The activity was performed on a raised platform to ensure that the entire range of motion could be captured by the c-arm fluoroscopy unit. Two researchers were at the subject's side during the activity to instruct the subject and provide a hand for balance if necessary. The fluoroscopic output was connected to a picture in picture (PiP) box. A live video of the subject was similarly connected to the PiP box. The PiP box was configured to overlay a scaled down version of the live video input on top of the fluoroscopy input. The PiP configuration was output to a recording device and serves as the raw video data for this research. This PiP video configuration is necessary to synchronize fluoroscopy data with vibration data. The switching of the sync light provides a visual indicator in the PiP video (Figure 3.5) and a voltage step in the data acquisition file (Figure 3.6). During analysis these two events can be aligned in the time domain to synchronize the vibration data with fluoroscopy data. The live video caption input to the PiP was disabled while the subject performed the DKB to ensure that anatomy of interest in the fluoroscopy video was not occluded by the live video. It was re-enabled after DKB trials were completed.

Subjects were positioned with the index leg in front of the contralateral leg. The c-arm was aligned to acquire lateral imaging of the index knee. Once positioned, the following steps were executed:

1. Start recording PiP video with live video input enabled
2. Start recording analogue data inputs
3. Switch the sync light on (ensure it is visible in the PiP video)
4. Disable live video input
5. Switch the fluoroscopy on

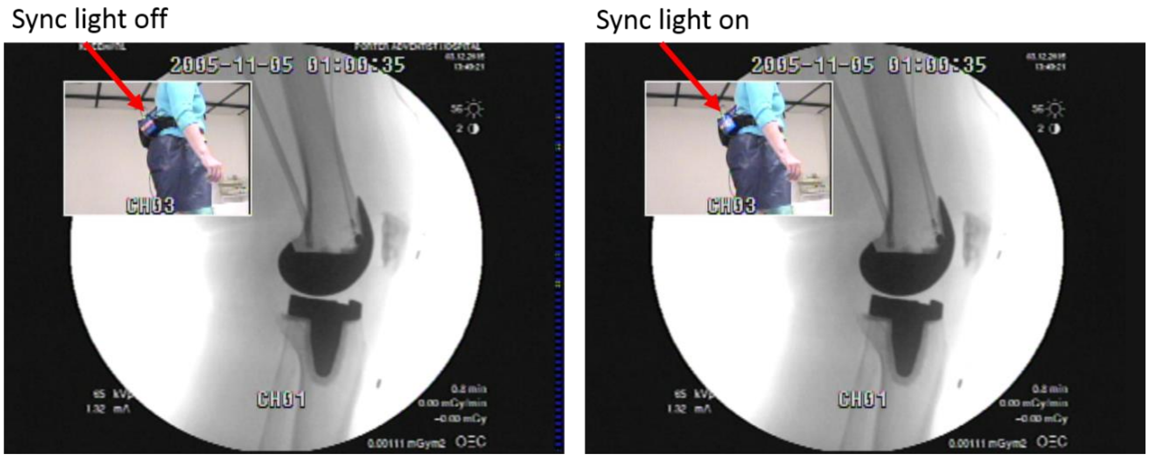

Figure 3.5. A picture-in-picture (PiP) video configuration was used to capture the sync light being switched from off (left) to on (right).

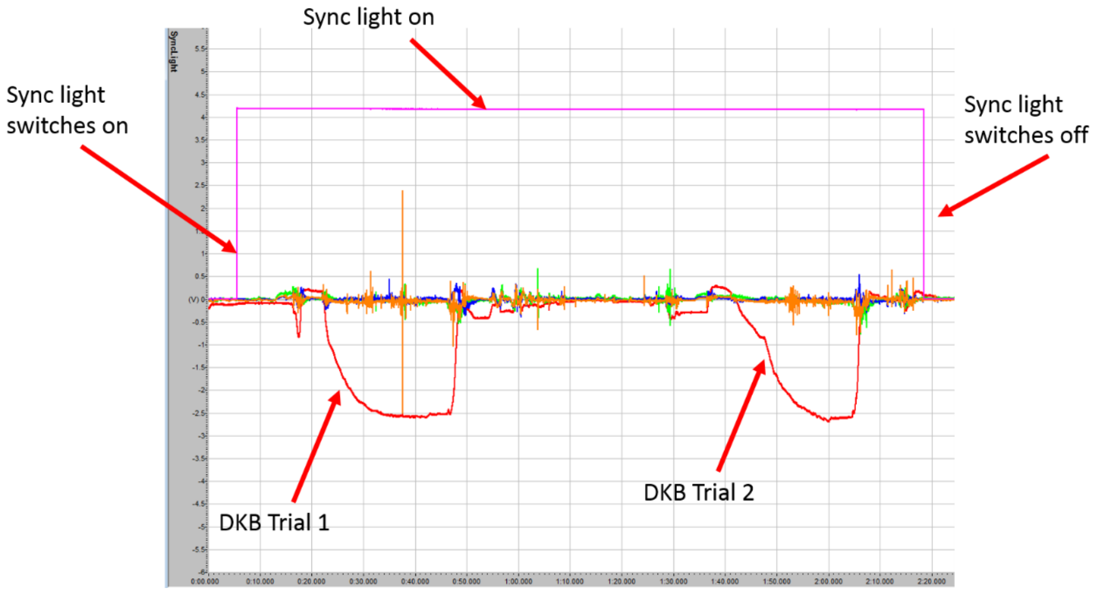

Figure 3.6. Raw data illustrating the sync light (purple signal) switching on and off during data collection. The goniometer (red signal) is used to reference the DKB trials. Accelerometer signals (green, blue, and orange signals) fluctuate during the activity.

6. Perform the deep knee bend
7. Switch the fluoroscopy off
8. Reposition subject and repeat steps 4-6 (second deep knee bend)
9. Re-enable the live video input
10. Switch the sync light off (ensure it is visible in the PiP video)
11. Stop recording analogue data inputs
12. Stop recording PiP video

Fluoroscopy and vibration data was successfully collected in nine deep knee bends. There were two trials captured for each of the five knees. One trial was not able to be used due to video data corruption.

3.3.4. Fluoroscopic Data Processing

Frames from the PiP video selected for analysis were corrected for pincushion distortion and imported into custom-designed software used for three-dimensional (3D) to two-dimensional (2D) registration. In this technique 3D computer-aided design (CAD) models of the femoral and tibial components are overlaid onto their respective silhouettes in the 2D fluoroscopy image (corrected for distortion) to obtain 3D position data of the implanted components (Figure 3.7). This registration technique used on the femoral component and tibial baseplate has previously been validated to provide an accuracy of 0.5 mm for in plane translations and 0.5° for in plane rotations [90]. Since the polyethylene tibial insert is nearly invisible in fluoroscopic images, it cannot be overlaid like the femoral and tibial components. Instead it was assumed to be rigidly fixed to the tibial baseplate. This was achieved by aligning the unique geometries of the distal tibial insert and proximal tibial baseplate in 3D space prior to overlaying (Figure 3.8). Once the tibial baseplate was overlaid onto its silhouette, the transformations were copied to the tibial insert. Next a body-to-body contact detection algorithm was executed to determine contact between the femoral component and the tibial insert (Figure 3.9).

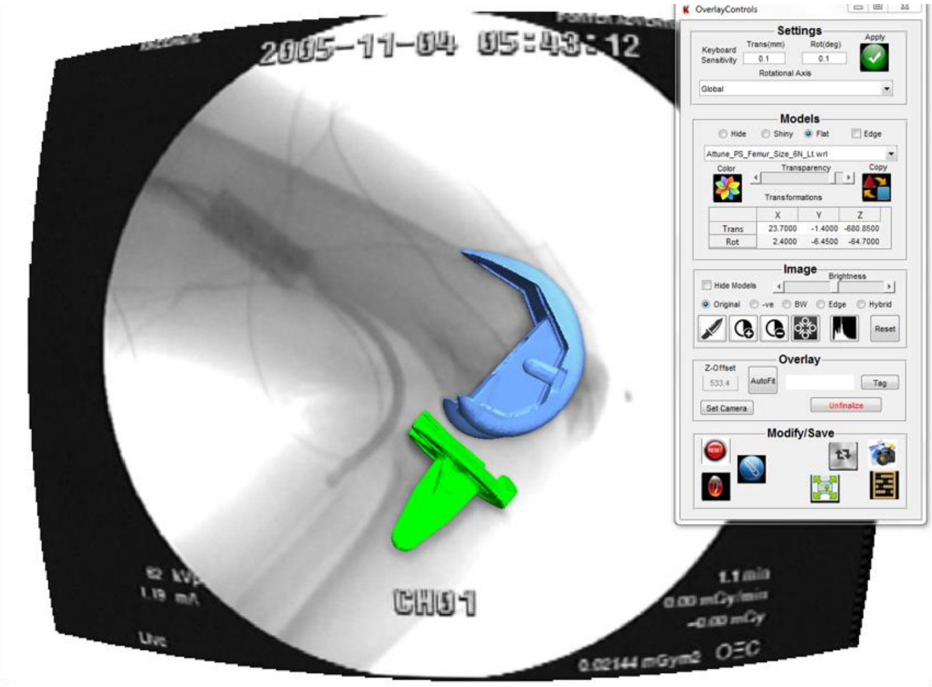

Keyboard Sensitivity: Trans(mm) 0.1, Rot(deg) 0.1

Rotational Axis: Global

○ Hide ○ Shiny ● Flat ☐ Edge

Attune_PS_Femur_Size_6N_Lt.wrl

Transparency

Transformations

	X	Y	Z
Trans	23.7000	-1.4000	-680.8500
Rot	2.4000	-6.4500	-64.7000

☐ Hide Models

● Original ○ -ve ○ BW ○ Edge ○ Hybrid

Z-Offset: 533.4

Keyboard Sensitivity: Trans(mm) 0.1, Rot(deg) 0.1

Rotational Axis: Global

● Hide ○ Shiny ○ Flat ☑ Edge

Attune_FB_Tibia_Size_4.wrl

Transparency

Transformations

	X	Y	Z
Trans	-1.7500	-55.6000	-675.4000
Rot	5.9000	177.4500	-39.8500

☐ Hide Models

● Original ○ -ve ○ BW ○ Edge ○ Hybrid

Z-Offset: 533.4

Figure 3.7. (Top) Femoral component and tibial baseplate CAD models overlaid on respective silhouettes. (Bottom) CAD model edges demonstrate the quality of fit.

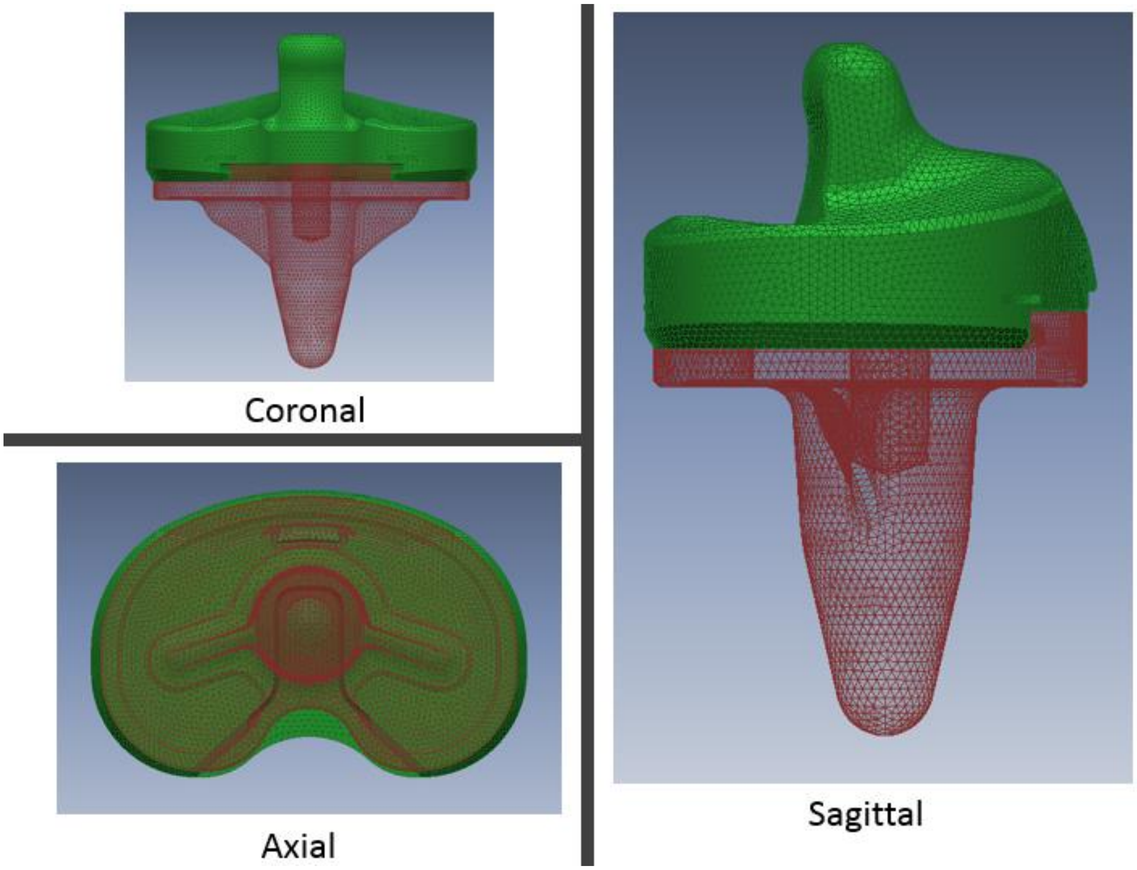

Coronal

Axial

Sagittal

Figure 3.8. The unique geometries of the distal tibial insert (green) and the proximal tibial baseplate (red) were mated in three-dimensional-space.

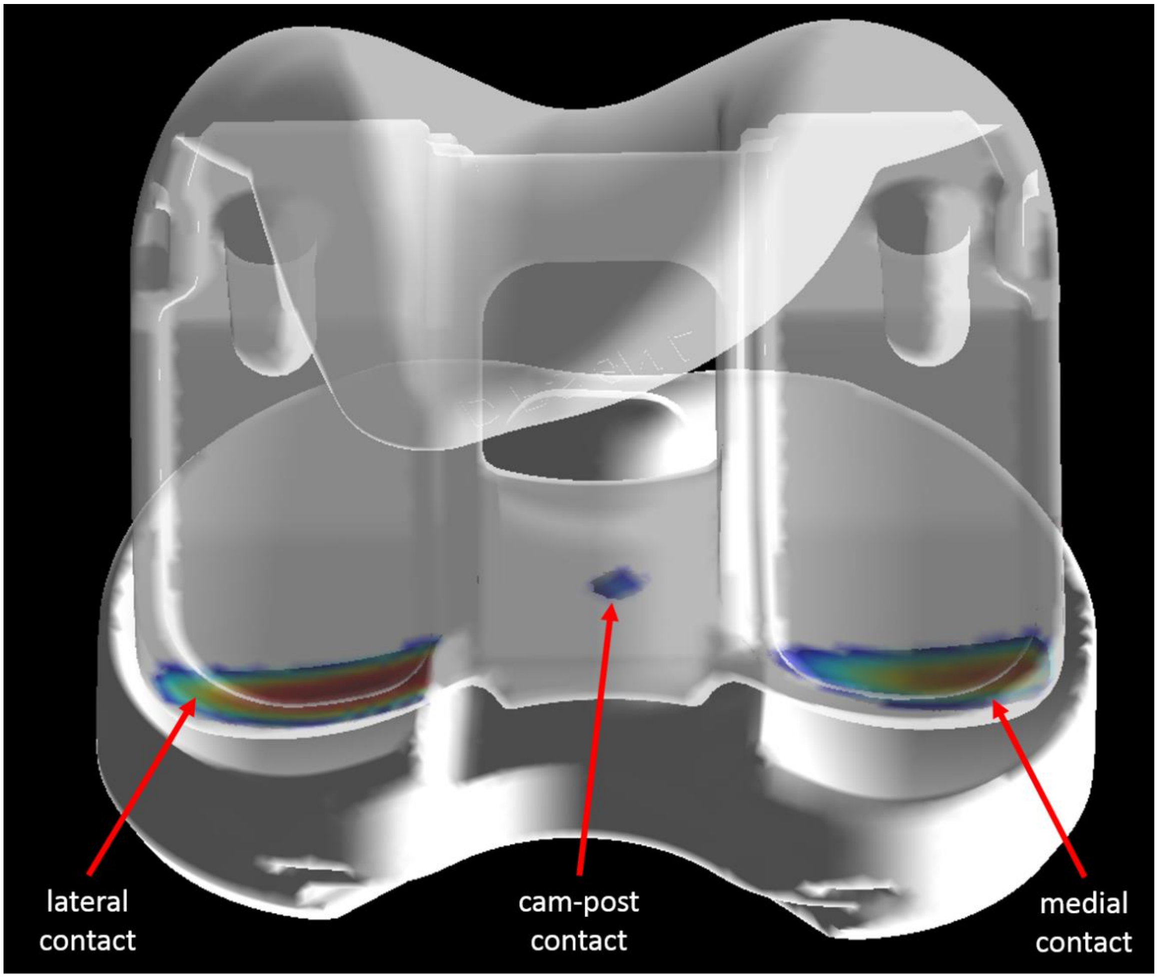

Figure 3.9. Body-to-body contact map between the femoral component and tibial insert.

Areas of contact were defined only by faces that were truly contacting faces on the opposing body (no threshold was applied). Inspection of contact (or lack of contact) at the cam-post interface served as a basis for additional frame selection. These frames were selected at 5° increments. If contact was not observed, a fluoroscopic frame with 5° more tibiofemoral flexion was selected. If contact was observed, the next frame selected was 5° less flexion. This guess and check process was repeated until three primary frames were overlaid – 1) *engagement minus 5°*, 2) *engagement*, and 3) *engagement plus 5°*. The first frame of the DKB (maximum extension) and the final frame of the DKB (maximum flexion) were also overlaid (Figure 3.10). The initial frame was selected based on preliminary inspection of vibration signals and published information on the Attune® engagement angle [86]. The vibrations signals were inspected for sharp transients between 80° and 100° of knee flexion. The time at which the most prominent transient appeared within this range of motion was used as the time of the initial frame.

3.3.5. Kinematic Model of Deep Knee Bend

Transformations of the overlaid frames were used to create a kinematic model of the implanted components on which additional analyses were conducted. First surfaces were defined on the cam and the post (Figure 3.11). Then a surface-to-surface contact detection algorithm was executed for each overlaid frame of the kinematic model. In agreement with the body-to-body contact detection previously described, the contact patch in this surface-to-surface analysis was comprised only of faces that were truly contacting faces on the opposing body. Specifically, for each face existing on the surface, true contact was said to exist if the distance from the base face to an opposing face along the path of the base face's normal vector was less than or equal to zero. The contact patch was used to evaluate the impact velocity of the cam with respect to the post at the *engagement* frame. A derivative of the technique described by Fitzpatrick et al. was used for this measurement [86].

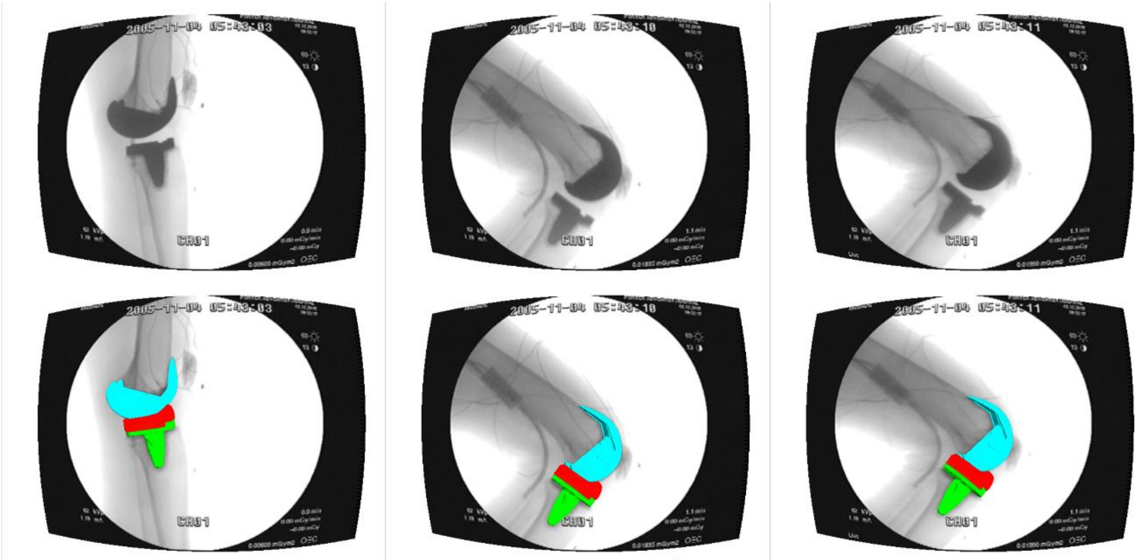

Maximum Extension

Engagement Minus 5°

Engagement

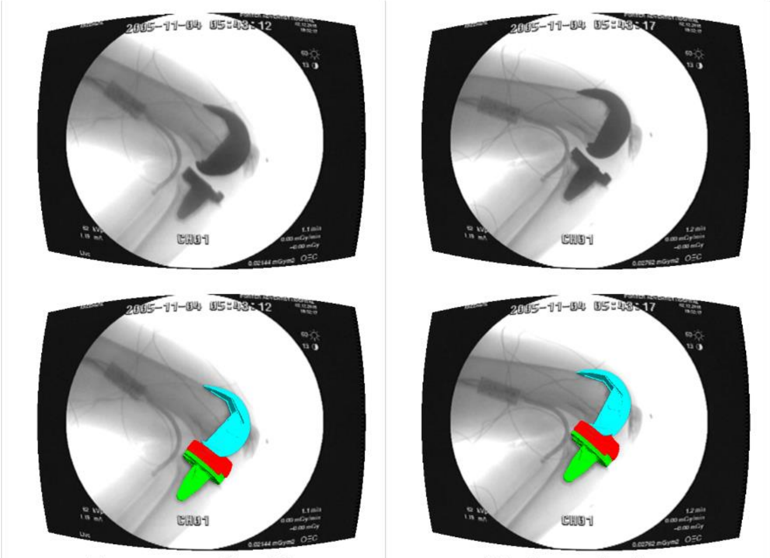

Engagement Plus 5°

Maximum Flexion

Figure 3.10. Fluoroscopy frames were selected and overlaid at maximum extension, engagement minus 5°, engagement, engagement plus 5°, and maximum flexion (*engagement* refers to engagement of the cam-post mechanism).

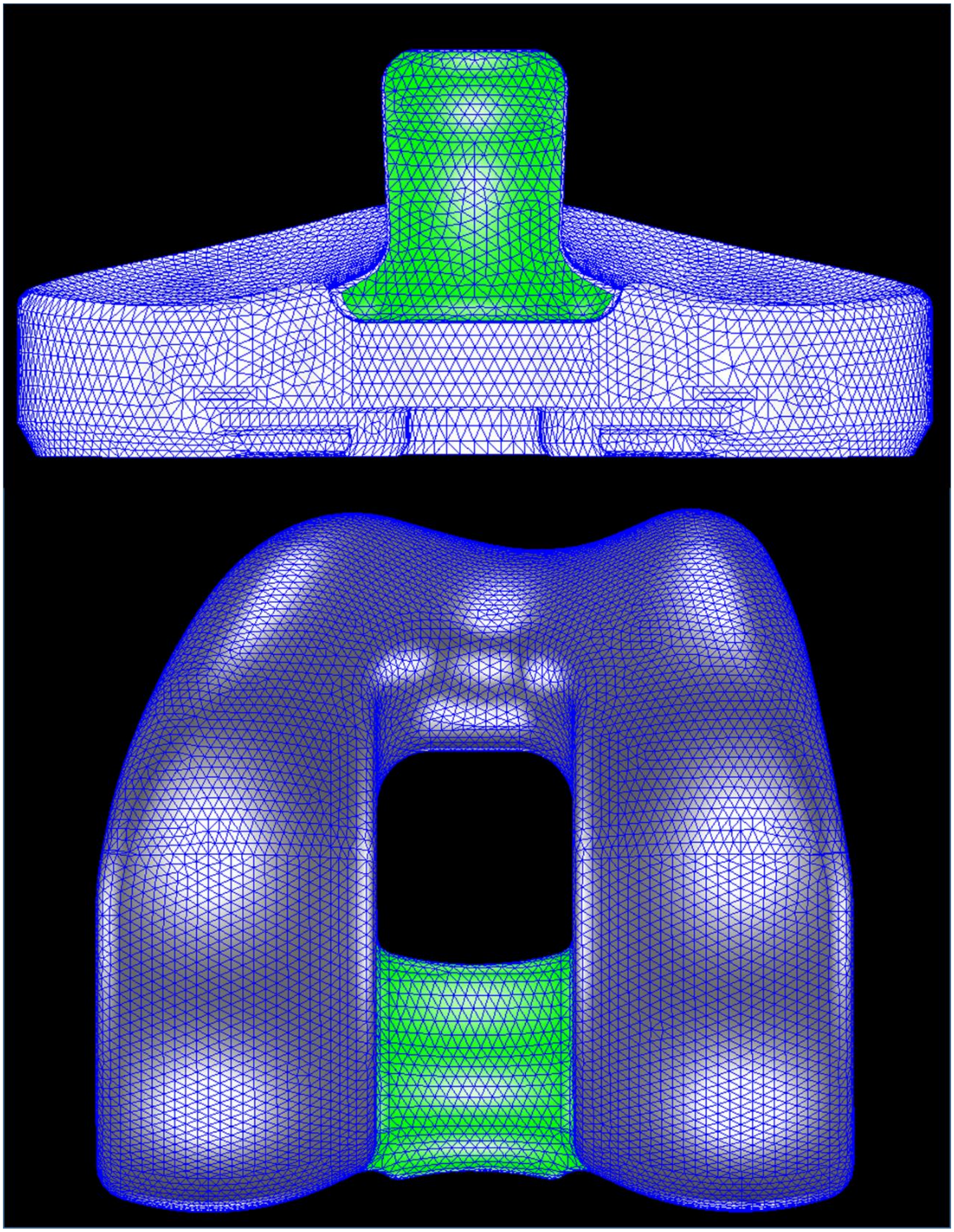

Figure 3.11. (Top) The post surface (green) was defined on the tibial insert, and (bottom) the cam surface (green) was defined on the femoral component.

In the present research, the contact point on the cam was defined as the center of the contact patch that existed on the cam surface at the *engagement* frame (Figure 3.12). The position of this point was then tracked for each overlaid frame with respect to the tibial bearing. The relative coordinates of the point at the *engagement* frame were used to define a second point on the post. Then the distance between the contact point on the cam and the contact point on the tibial post was measured for each overlaid frame up to the *engagement* frame (Figure 3.13). The change in this distance from the *engagement minus 5°* frame to the *engagement* frame was measured with respect to time and flexion to obtain the impact velocity in millimeters per second and millimeters per degree of knee flexion. Measuring with respect to knee flexion effectively normalizes the data to account for the different speed at which subjects perform the deep knee bend [86].

The height of the contact point on the tibial post was also assessed. Since the implant sizes varied from subject to subject, the SI coordinate of the contact point on the tibial post was normalized by the SI distance from the top of the post to the dwell point of the tibial insert (Figure 3.14). These two points were programmatically extracted from surfaces defined on the top of the post and the medial dish to ensure that the dimension used for normalization was consistently specified across all subjects.

3.3.6. Vibration Signals Processing

Raw vibroarthrograms were first synchronized with the fluoroscopy video. This was done using the sync light. Specifically, all analogue signals (three accelerometers, goniometer, and sync light) were cropped up to the time at which the light is switched on. This instance in time was distinguished in the data file as a prominent voltage step on the sync light channel (Figure 3.6). Once synchronized, the relative time of each overlaid frame with respect to the light being switched on was used to navigate the vibration signals. The start time and end time of each DKB was

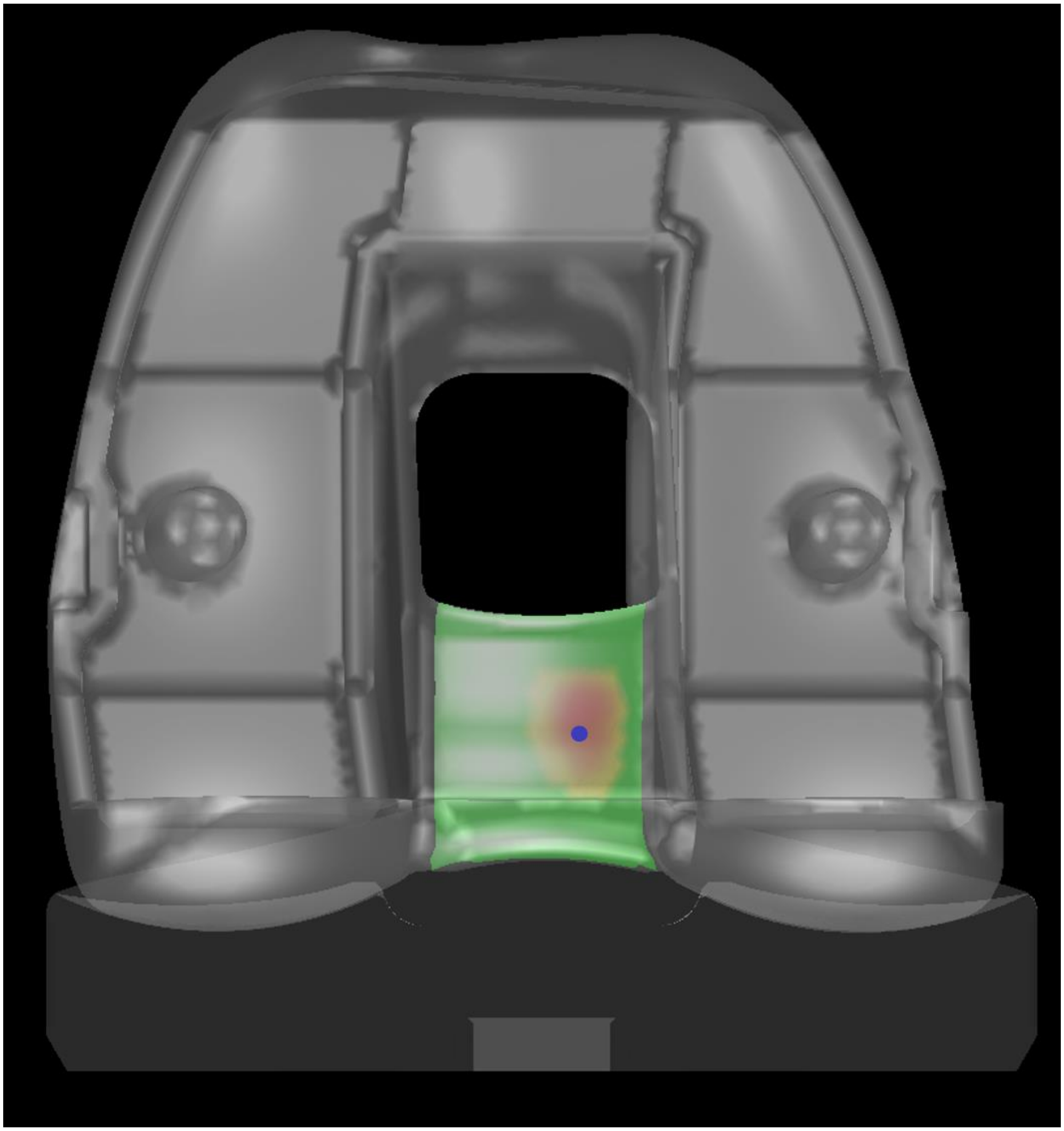

Figure 3.12. The contact point on the cam (blue dot) at the engagement frame was defined at the center of the contact patch (yellow and red area) that existed on the predefined cam surface (green).

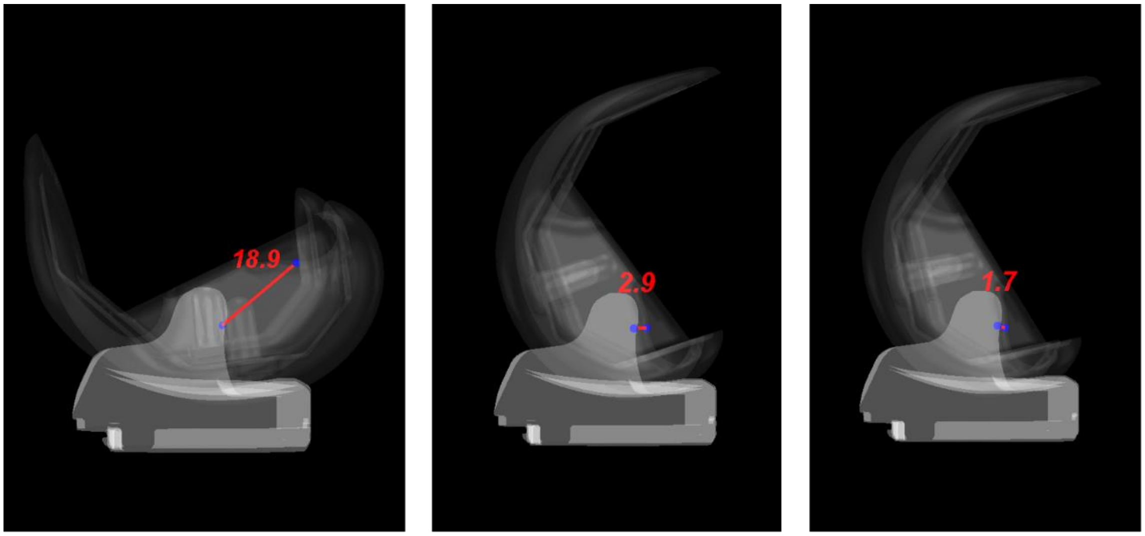

Maximum Extension Engagement Minus 15° Engagement Minus 10°

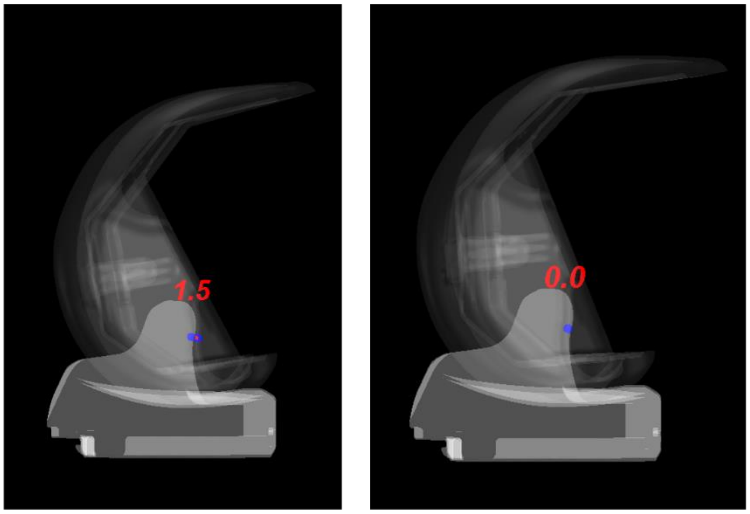

Engagement Minus 5° Engagement

Figure 3.13. The distance (mm) between the contact point on the cam and the contact point on the post was calculated for each overlaid frame up to the engagement frame.

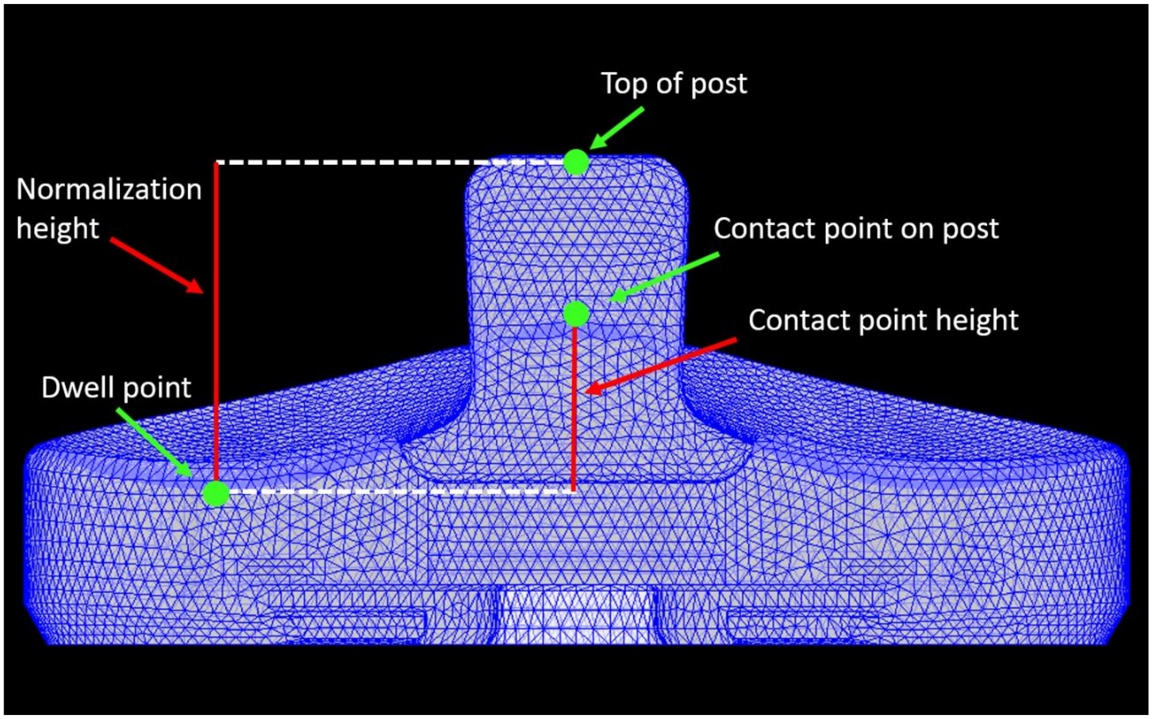

Figure 3.14. Contact point height was measured with respect to the dwell point along the superior/inferior axis. Contact point height was normalized by the distance between the dwell point and the top of the post along the superior/inferior axis.

then processed for feature extraction. First a cascade moving average filter was applied to all three accelerometer channels to estimate and remove the baseline wander present in the signals. This filter serves to remove non-stationary low frequency signals that are caused by patient movement and or trembling that will interfere with vibration signals of interest. The filter was constructed following an algorithm presented by Cai et al. [91]. This filter contains two layers. The first layer contains a *M*-order and a *N*-order moving average operator. The *K* inputs at the end of the *M*-order operator overlap the initial inputs of the *N*-order operator [91]. The second layer smooths the resulting piecewise linear trends obtained in the first layer. Both the *M* and *N* moving average operators were specified as 20th order operators. *K* was specified as 5 overlapping inputs. The final output as presented by Cai et al. is given as

$$y(i) = \frac{[o_1(i) + o_2(i)]}{2} = \frac{1}{2M}\sum_{m=1}^{M} x(i-m) + \frac{1}{2N}\sum_{n=1}^{N} x(i-M+K-n)$$

in which $o_1(i)$ and $o_2(i)$ are the *M* and *N* order moving average operators [91]. The transfer function $H(z)$ of this cascade moving average filter, similarly presented by Cai et al., is obtained by applying the *z*-transform to achieve

$$H(z) = \frac{Y(z)}{X(z)} = \frac{1}{2M}(z^{-1} + \cdots + z^{-M}) + \frac{1}{2N}(z^{-M+K-1} + \cdots + z^{-M+K-N})$$

Once filtered, the data was prepared for feature extraction. First the filtered data was segmented into nonoverlapping windows. Then nine features were calculated in each window to test for correlation with the time of cam-post engagement. Local features included 1) minimum, 2) maximum, 3) mean squared, 4) variance, 5) mobility, 6) form factor, 7) crest factor, and 8) peak-to-average power ratio. The first two local features (minimum and maximum) were used to calculate the envelope amplitude as described by Yang et al. [92]. In their research, the signal envelopes were defined by linear interpolation of the local minima and maxima. In the present work, Hermite interpolation (third order) was used to derive the upper envelope and lower envelope from the local maxima and local minima respectively (Figure 3.15A and Figure 3.15B). Then the envelope amplitude was calculated as the difference between the upper and lower envelope at each interpolated point in time (Figure 3.15C).

The third local feature, mean squared, is a simple statistical measurement in which all samples in a window are averaged. The average value is then squared to obtain an exaggerated representation of the local mean value.

Features 5, 6, and 7 are all related temporal metrics that were presented together in the 1970s as an alternative to the Fourier transform for characterizing the fluctuations associated with electroencephalography (EEG). Hjorth explains that together these three parameters have been shown to characterize patterns in terms of amplitude, time scale, and complexity [93, 94]. At the time he described variance as *activity* and form factor as *complexity.* Hjorth presents the parameters in the following fashion: *activity* is the squared standard deviation of the signal amplitude (also known as variance or mean power), *mobility* is the standard deviation of the signal slope with respect to the standard deviation of the signal amplitude, and *complexity* is the number of standard slopes generated during the average time required to generate one standard amplitude as defined by *mobility* [93]. Since Hjorth, these features have been adopted for the analysis of signals other than EEG. Rangayyan’s research group has tested the applicability of these temporal metrics in vibroarthrography [26]. In their work *complexity* is referred to as the signal *form factor*. They state that the form factor is an improved representation of a signal’s variability [26]. Mathematically the local mobility (M_x) and local form factor (FF) for the index window were derived from the standard deviation of the local signal (σ_x) and the and the standard deviation of the local

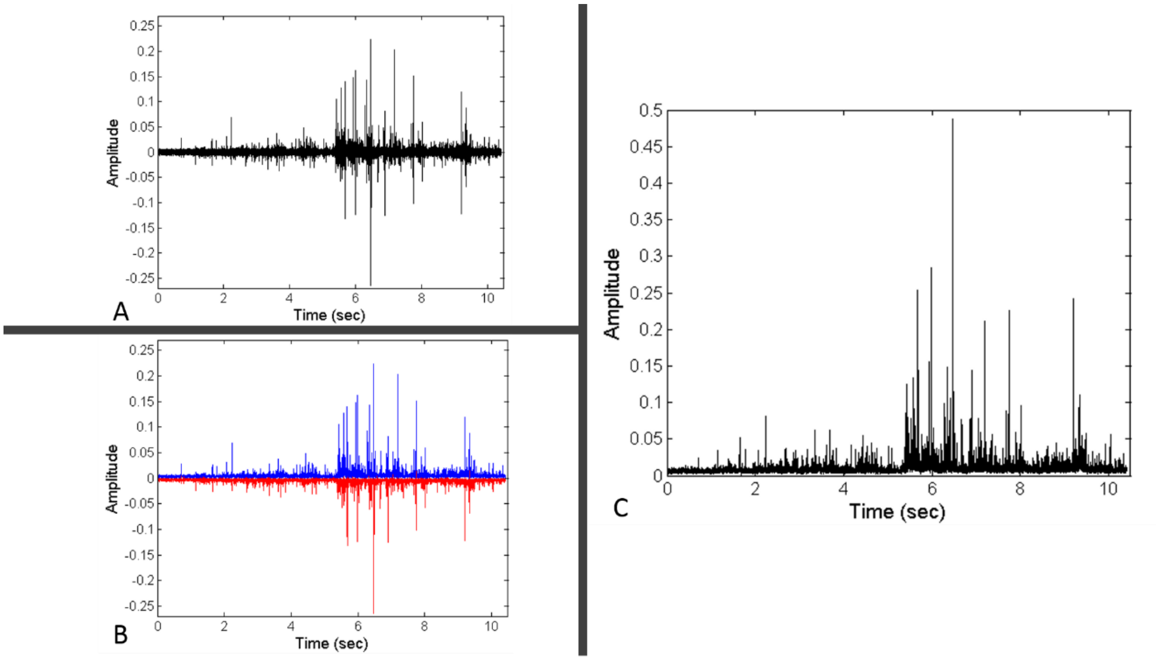

Figure 3.15. (A) The filtered summation signal. (B) The upper (blue) and lower (red) signal envelopes are calculated and subtracted to obtain (C) the envelope amplitude.

signal derivatives ($\sigma_{x'}$ and $\sigma_{x''}$) by following the algorithms presented by Rangayyan and Wu [26]

$$M_x = \left[\frac{\sigma_{x'}^2}{\sigma_x^2}\right]^{\frac{1}{2}} = \frac{\sigma_{x'}}{\sigma_x}$$

$$FF = \frac{M_{x'}}{M_x} = \frac{\sigma_{x''}/\sigma_{x'}}{\sigma_{x'}/\sigma_x}$$

The last two features, crest factor and peak-to-average power ratio (PAPR) served to quantify how extreme the peaks in each window were. The crest factor, C, is defined as

$$C = \frac{|x_{peak}|}{x_{rms}}$$

in which x_{peak} is the greatest amplitude present in the signal in the index window, and x_{rms} is the root-mean-square of the signal in the index window. x_{rms} is defined as

$$x_{rms} = \sqrt{\frac{1}{N}\sum_{n=1}^{N}|x_n^2|}$$

in which N is the number of data points in the index window. The local PAPR is then simply defined as

$$PAPR = \frac{|x_{peak}|^2}{{x_{rms}}^2} = C^2$$

in which the numerator is the peak power of the local signal and the denominator is the average power of the local signal.

3.3.7. Approximating Cam-Post Engagement Time With Maximum Features

The vibrations from nine DKBs were evaluated for the ability to approximate the cam-post engagement time. The seven local features were calculated in nonoverlapping windows for all three accelerometer signals as well as the summation of the three signals. The time associated with the end of the window in which the maximum of the local features existed was compared to the time associated with the *engagement* frame (Figure 3.16). It is important to describe this assessment in the context of the research activity. First, the deep knee bend was performed at a relatively slow pace. This had to be done to ensure the image quality was acceptable for overlaying CAD models. If a subject moved too quickly the possibility of motion blur and loss of anatomy within the field of view increased. These two types of image acquisition issues limit the ability to accurately conduct the analysis and therefore had to be mitigated at the time of data collection by tempering the speed of the research participants. Maximum extension and maximum flexion were used along with the start and end time of each DKB to approximate the global rate of tibiofemoral flexion in degrees/second (°/sec) (Table 3.1). The slowest DKB was performed at 6.94 °/sec, and the fastest DKB was performed at 12.13 °/sec. On average, deep knee bends were performed at a rate of 9.69 °/sec ± 2.05 °/sec. It is equally important to note that the time at which cam-post engagement occurs is not precisely known. In this analysis the time of engagement is the time at which engagement is first *definitively* identified via 3D-to-2D registration. It is logical to assume that engagement may have occurred sometime prior to this overlaid frame. In this context the duration of the *target* window in which engagement is known to occur should be considered when interpreting the results. In this window the tibiofemoral flexion changes by 5°. Across the nine deep knee bends analyzed, the duration of target windows ranged from 0.46 seconds to 0.90 seconds. The average *target* window was 0.66 sec ± 0.14 sec. The difference between the end time of the window in which the

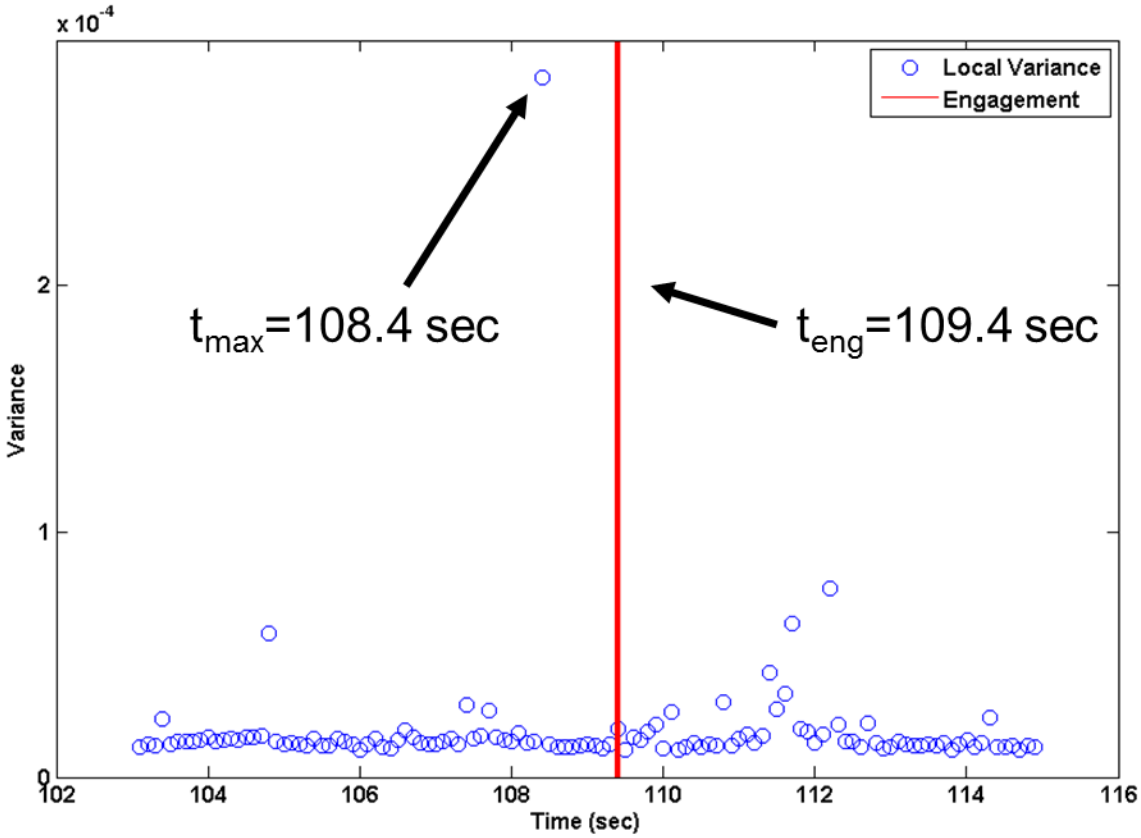

Figure 3.16. The time associated with the maximum local feature (t_{max}) was subtracted from the time of engagement (t_{eng}) to calculate the error in approximating the occurrence of cam-post engagement. In this example the maximum local variance (blue circles) underestimated the time of engagement (red line) by 1.0 second.

Table 3.1. Deep Knee Bend Range of Motion and Rate of Tibiofemoral Flexion

DKB ID	Maximum Extension (°)*	Maximum Flexion (°)	DKB Duration (sec)	Tibiofemoral Flexion Rate (°/sec)
001	-4	118	14.04	8.68
002	-8	119	11.91	10.66
003	-6	113	16.22	7.34
004	-4	120	10.41	11.91
005	-3	109	16.15	6.94
006	-7	113	11.01	10.90
007	-1	118	9.81	12.13
008	-5	105	14.45	7.61
009	-3	111	10.31	11.05

*Negative values of Maximum Extension indicate hyperextension of the tibiofemoral joint.

maximum local feature occurred, and the *engagement* frame time is described as the error. Negative error indicates that the maximum local feature occurred at a time prior to the *engagement* frame time, and a positive error indicates that the maximum local feature occurred at a time after the *engagement* frame time. This assessment was conducted for window lengths equal to 10 samples (0.001 seconds), 100 samples (0.01 seconds), and 1000 samples (0.1 seconds)

3.3.8. Correlating Vibrations to Cam-Post Engagement Mechanics

A second and third assessment was conducted using the same features to investigate feature correlation with engagement velocity and contact point height. For these assessments the features were only calculated for a single window of data – the *target* window. The start and end of the *target* window was the time associated with two overlaid frames. The start time corresponded to *engagement minus 5°* and the end time corresponded to *engagement*. In *engagement minus 5°* the cam-post mechanism is definitively not engaged, and conversely in the *engagement* frame the cam-post mechanism is definitively engaged. Therefore, it is known that engagement occurs between these two frames. In similar fashion to the first assessment, target features were derived from all three signals as well as the summation of the signals. The strength of the linear relationship between each target feature and the engagement velocity was measured by the Pearson Product-Moment Correlation which was calculated using JMP Statistical Discovery software (SAS Institute, Cary, NC).

3.4. Results

3.4.1. Cam-Post Engagement Time Approximation Errors

In the medial femoral epicondyle signal with a window length of 10 samples (0.001 seconds), the smallest error in determining engagement time was -0.050 seconds and was derived from the maximum local mean squared. The median of the maximum local mobility and the maximum local form factor were 0.429 seconds and -0.155 seconds respectively. The maximum local variance was the tightest set of data with a box height (75th percentile minus the 25th percentile) of 4.740 seconds (Figure 3.17). Given a window size of 10 samples, no feature derived from the medial femoral epicondyle signal stands out as a viable option for predicting cam-post engagement time with reasonable accuracy. Increasing the window size by a factor of 10 to 100 samples (0.01 seconds) significantly affected the calculated errors derived from the medial femoral epicondyle signal (Figure 3.18). The maximum local crest factor and PAPR features became relatively accurate features with a median error of -0.279 seconds and a box height of 3.506 seconds. Increasing the window size to 1000 samples (0.1 seconds) did not have a positive effect on most of the features (Figure 3.19).

The errors for the patella signal contained similarly gross magnitudes. For a window size of 10 samples (0.001 seconds), the maximum local envelope amplitude can be considered the most accurate feature with a median error of -0.364 seconds and a box height of 2.914 seconds (Figure 3.20). Increasing the window size to 100 samples (0.01 seconds), increased the median error in this feature to -1.005 seconds, but decreased the box height to 2.786 seconds. The maximum local crest factor and PAPR were significantly impacted by the increase in window size to 100 samples (Figure 3.21). The median error magnitude for these features was reduced from 0.998 seconds to -0.417 seconds and the box height was reduced from 3.971 seconds to 3.384 seconds. Increasing the window size to 1000 samples (0.1 seconds) further reduced the median error and box height of the maximum local crest factor and PAPR features, although not by a significant amount (Figure 3.22).

In the tibia signals, the maximum local variance and the maximum local envelope amplitude errors were identical for all subjects, when the window size was equal

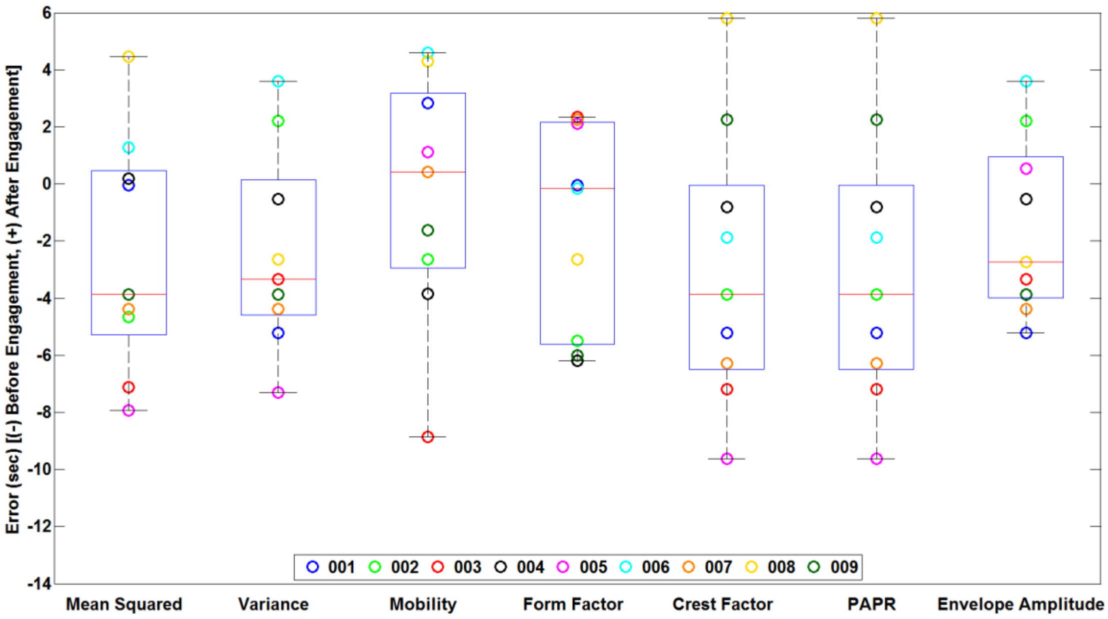

Figure 3.17. The cam-post engagement time error measured in the medial femoral epicondyle signal features for a window size of 10 samples (0.001 seconds). Color indicates DKB ID.

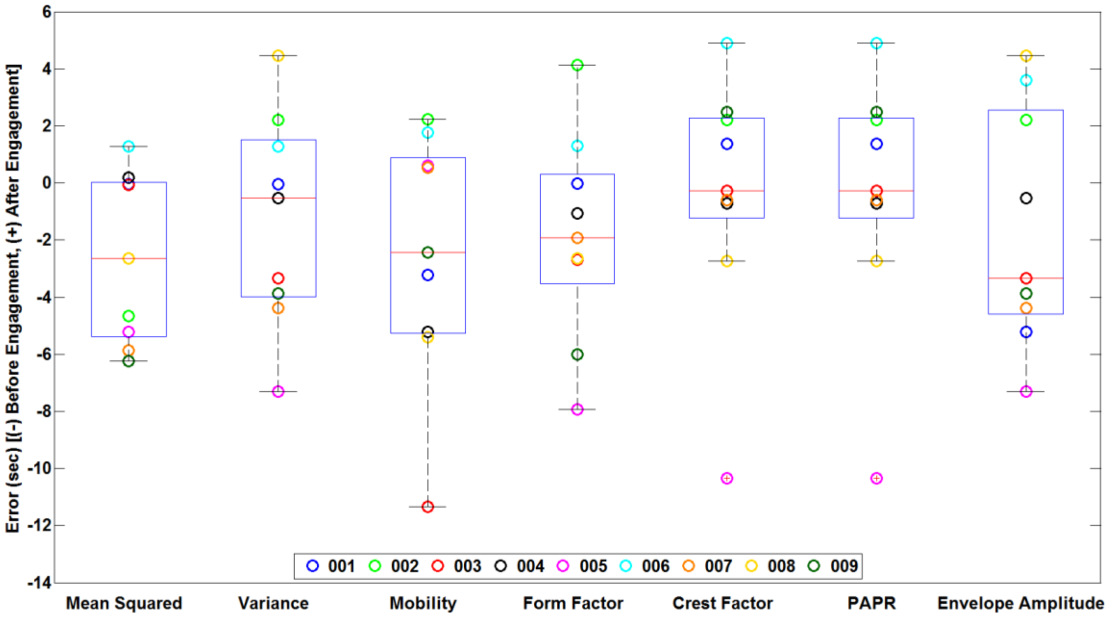

Figure 3.18. The cam-post engagement time error measured in the medial femoral epicondyle signal features for a window size of 100 samples (0.01 seconds). Color indicates DKB ID.

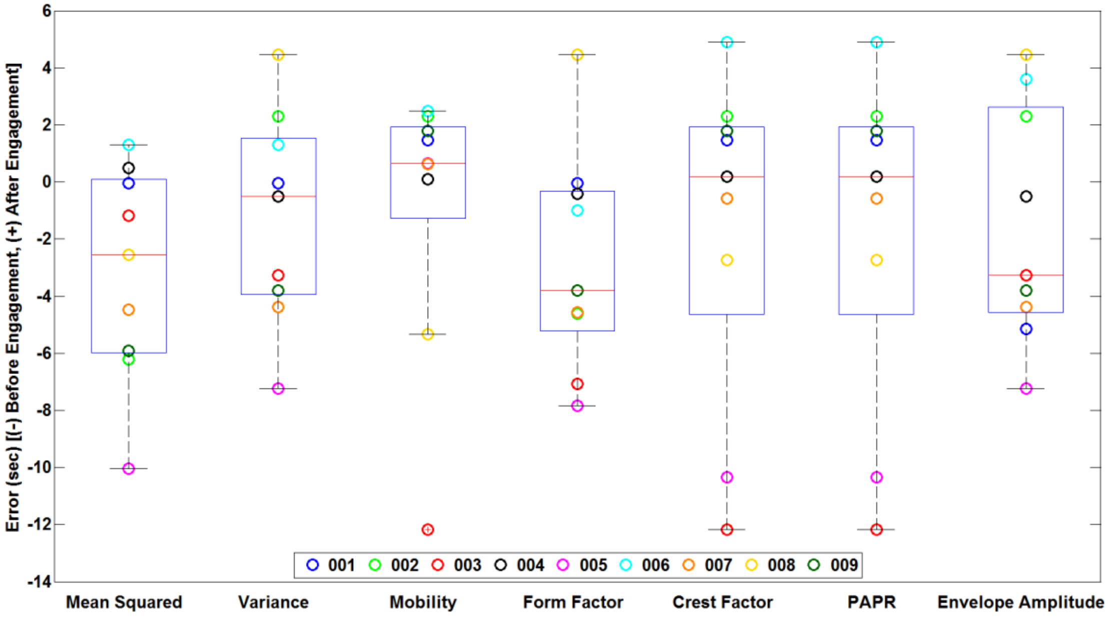

Figure 3.19. The cam-post engagement time error measured in the medial femoral epicondyle signal features for a window size of 1000 samples (0.1 seconds). Color indicates DKB ID.

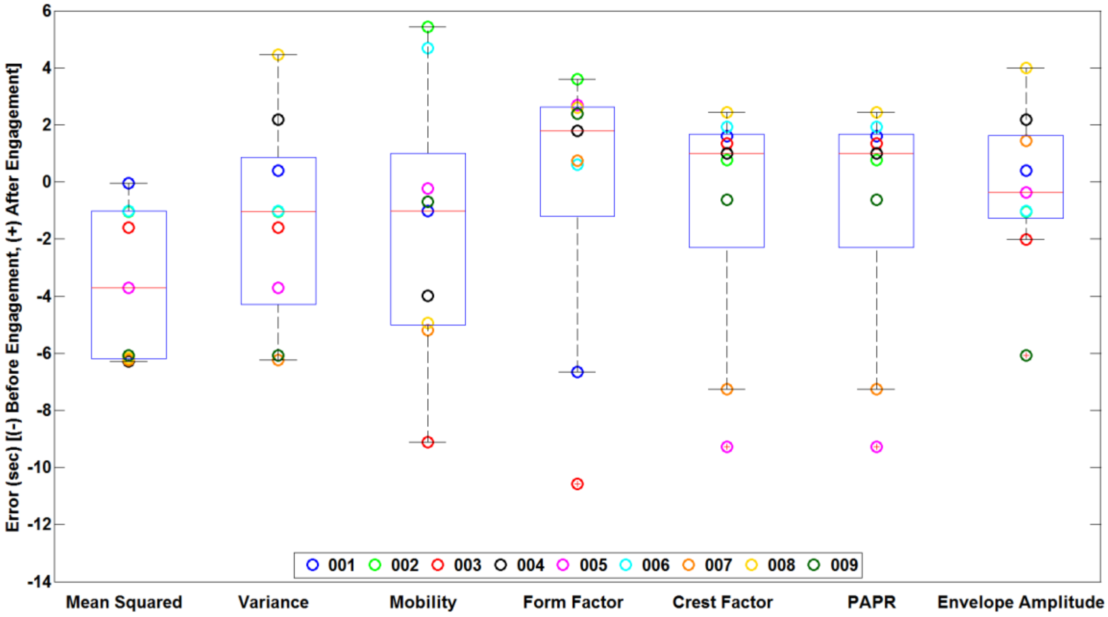

Figure 3.20. The cam-post engagement time error measured in the patella signal features for a window size of 10 samples (0.001 seconds). Color indicates DKB ID.

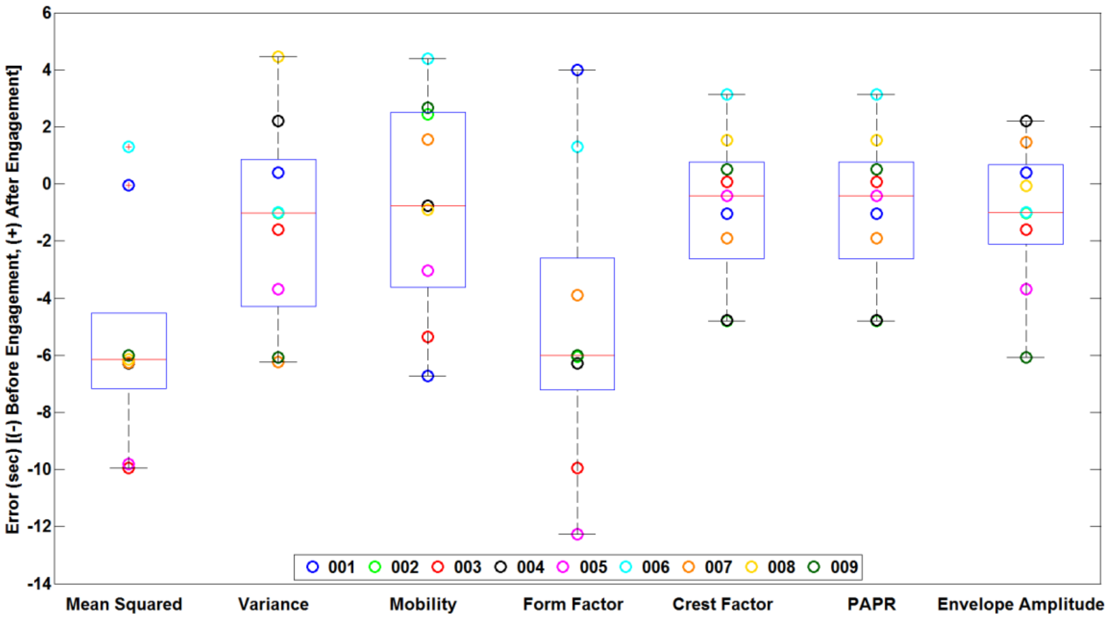

Figure 3.21. The cam-post engagement time error measured in the patella signal features for a window size of 100 samples (0.01 seconds). Color indicates DKB ID.

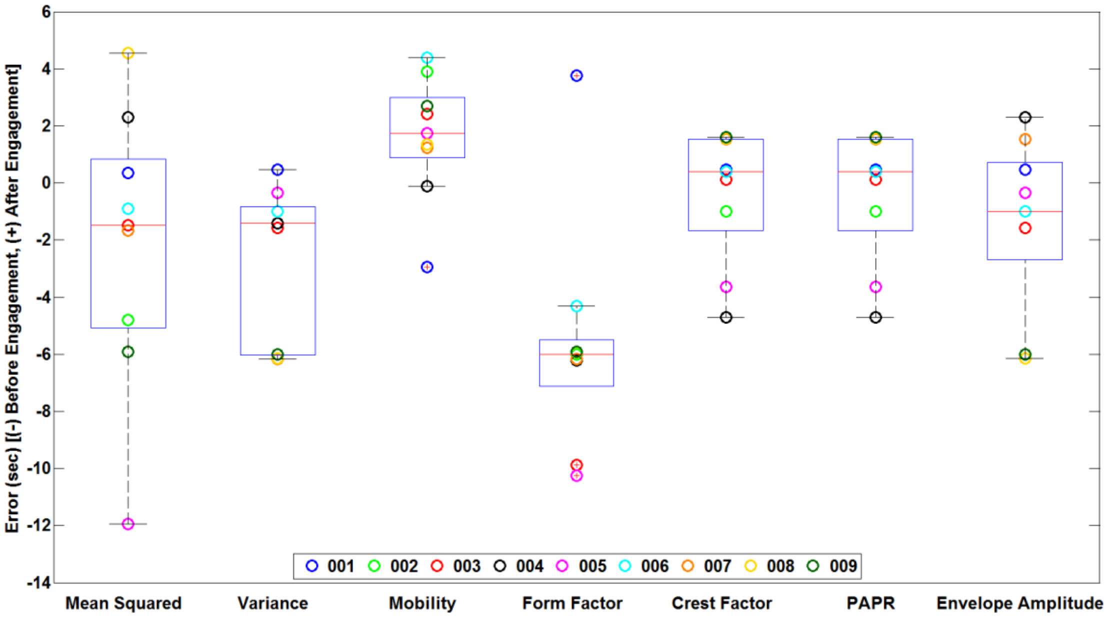

Figure 3.22. The cam-post engagement time error measured in the patella signal features for a window size of 1000 samples (0.1 seconds). Color indicates DKB ID.

to 10 samples (0.001 seconds). These two features had a median error of 0.092 seconds and a box height of 2.848 (Figure 3.23). Six of the nine DKB data points for these features had an error magnitude of less than 1.314 seconds. Increasing the window size to 100 and 1000 samples (0.01 and 0.1 seconds) did not positively affect the error of these features (Figure 3.24 and Figure 3.25). Additionally, the increase in window sizes did not result in any other features becoming stronger predictors of cam-post engagement when compared to variance and envelope amplitude.

In similar fashion to the tibia signals, the maximum local variance and envelope amplitude derived from the summation of signals consisted of identical errors for a window size of 10 samples (0.001 seconds). These two features with this window size can be considered the most accurate in their ability to predict cam-post engagement as the errors were consistently negative and tightly clustered (Figure 3.26). The median error for these two features was -0.630 seconds, and the box height was 0.880 seconds. Both features consistently underestimated cam-post engagement (negative error). Seven of the nine DKB data points had an error magnitude of less than 1.593 seconds. The other two DKB data points (008 and 009) are considered statistical outliers (noted by the red '+' symbol inside of the yellow and dark green data points in Figure 3.26). Increasing the window size to 100 samples (0.01 seconds) did not significantly affect the error associated with these two features (Figure 3.27). Increasing the window size to 1000 samples (0.1 seconds) compromised the accuracy of variance and envelope amplitude by the same amount. The median error increased in magnitude from -0.630 seconds to -1.005 seconds and the box height increased from 0.880 seconds to 2.187 seconds (Figure 3.28). This increase in window size did improve the error associated with the maximum local crest factor and PAPR features. The median error for these features decreased in magnitude from -1.052 seconds to 0.193 seconds and the

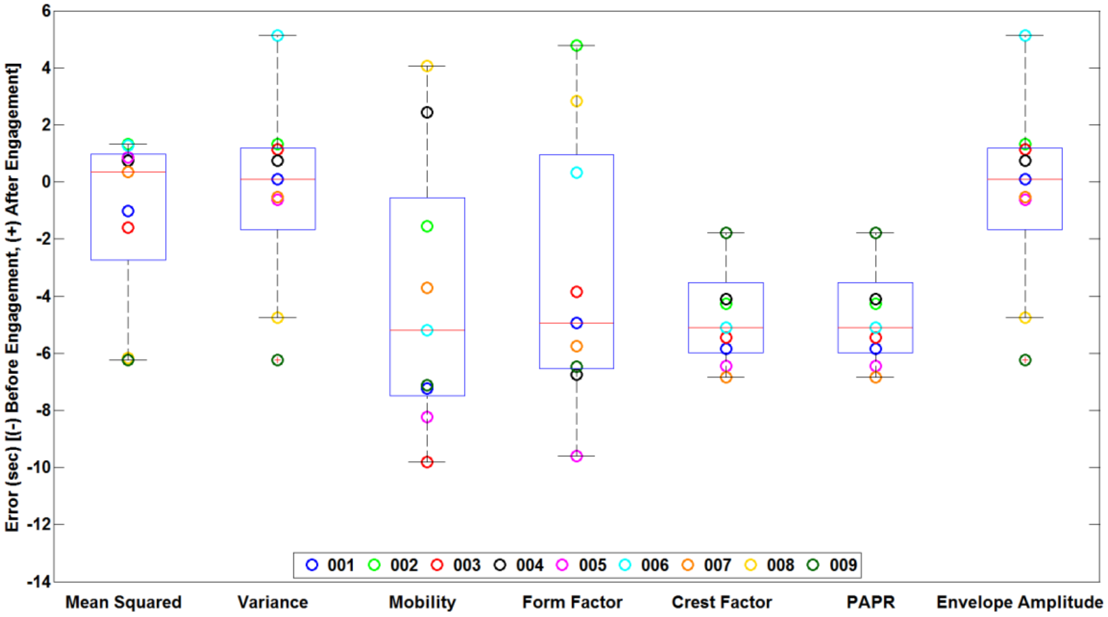

Figure 3.23. The cam-post engagement time error measured in the tibial tuberosity signal features for a window size of 10 samples (0.001 seconds). Color indicates DKB ID.

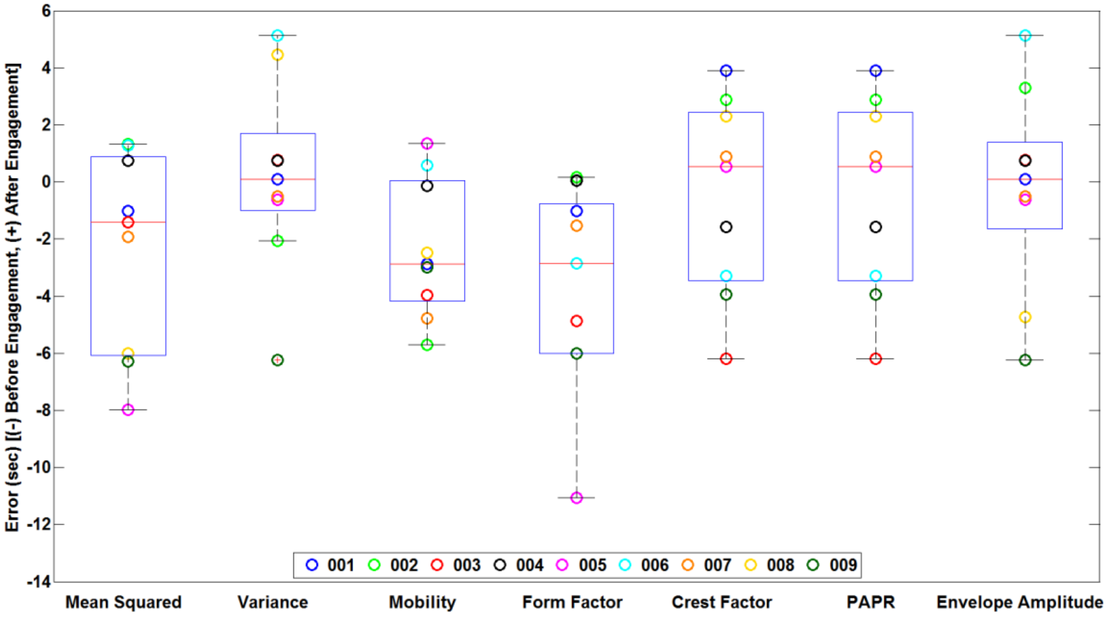

Figure 3.24. The cam-post engagement time error measured in the tibial tuberosity signal features for a window size of 100 samples (0.01 seconds). Color indicates DKB ID.

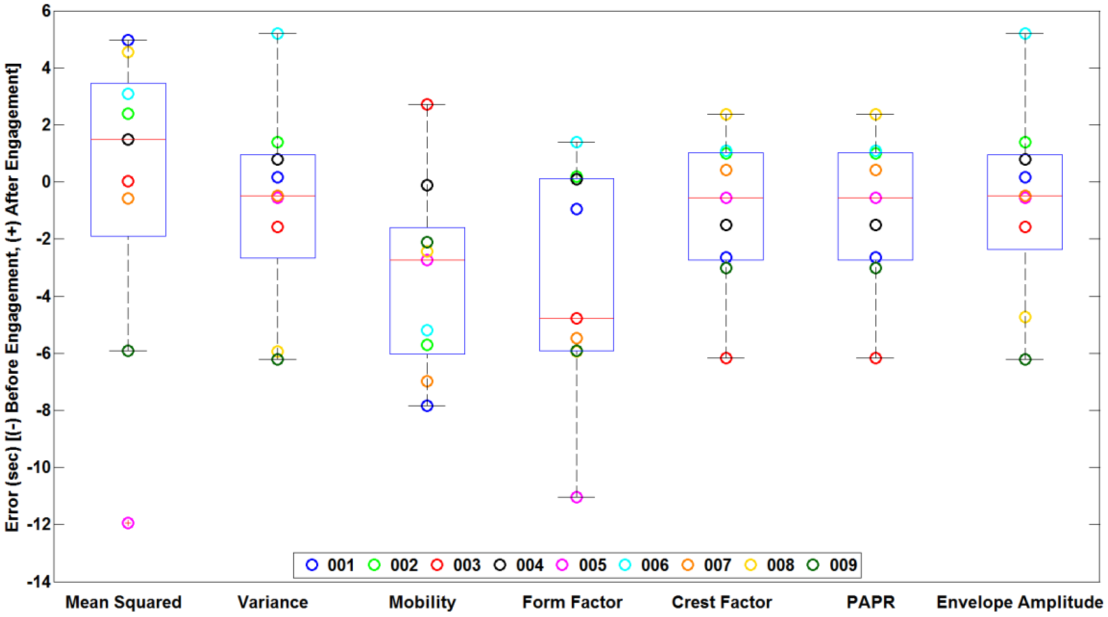

Figure 3.25. The cam-post engagement time error measured in the tibial tuberosity signal features for a window size of 1000 samples (0.1 seconds). Color indicates DKB ID.

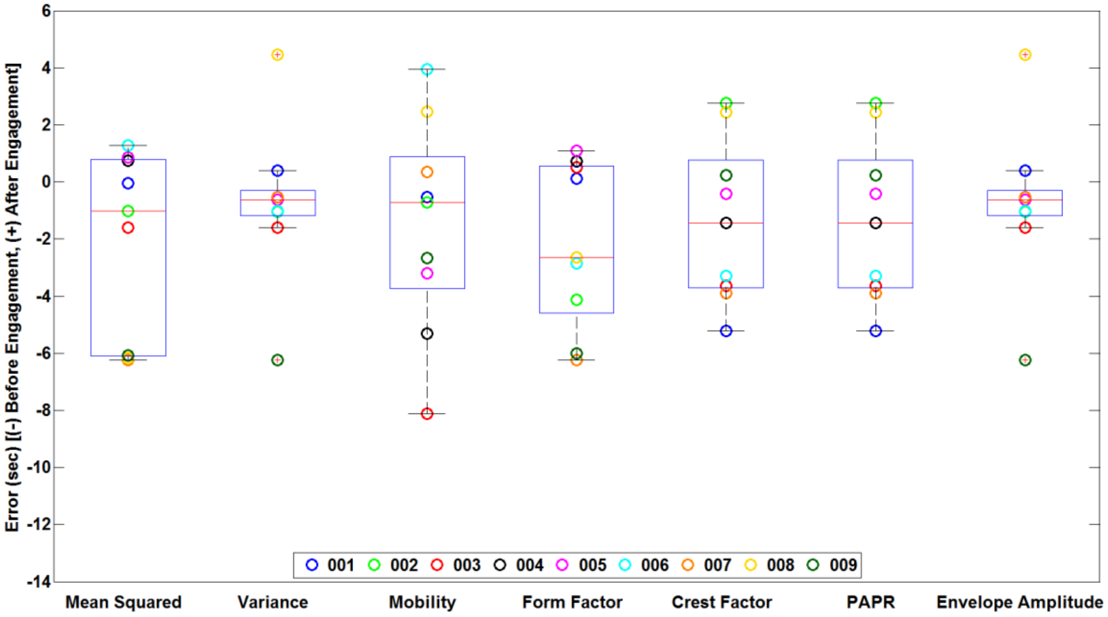

Figure 3.26. The cam-post engagement time error measured in the summation signal features for a window size of 10 samples (0.001 seconds). Color indicates DKB ID.

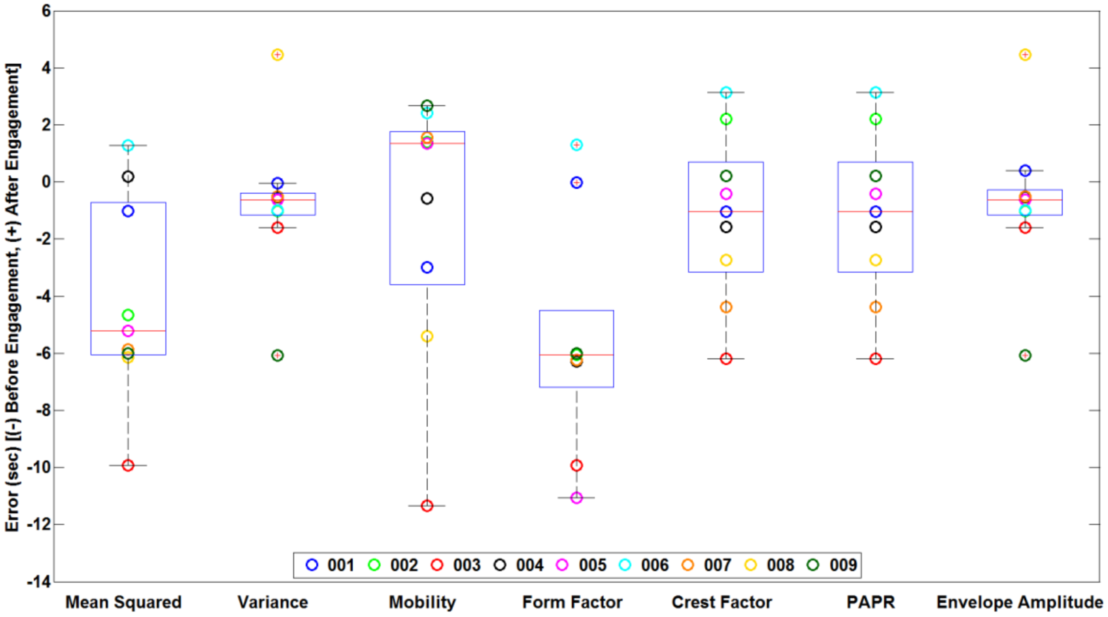

Figure 3.27. The cam-post engagement time error measured in the summation signal features for a window size of 100 samples (0.01 seconds). Color indicates DKB ID.

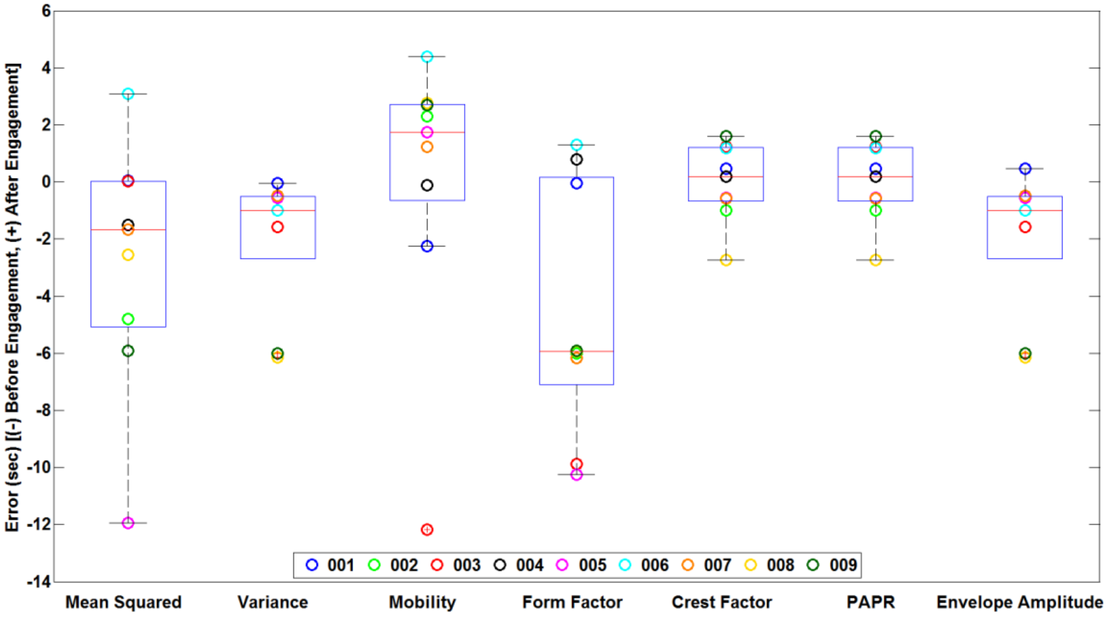

Figure 3.28. The cam-post engagement time error measured in the summation signal features for a window size of 1000 samples (0.1 seconds). Color indicates DKB ID.

box height decreased from 3.857 seconds to 2.187 seconds (Figure 3.27 and Figure 3.28).

3.4.2. Correlating Vibrations to Cam-Post Engagement Velocity

The Pearson Product-Moment Correlation coefficient between each target feature and the engagement velocity was also assessed to further study the relationship between vibrations emitted from a PS TKA and the dynamics of cam-post engagement. Coefficients were calculated for the absolute velocity measured in mm/sec (r_{abs}) (Table 3.2) and the normalized velocity measured in mm/deg (r_{norm}) (Table 3.3). For the medial femoral epicondyle signal, the mobility had the strongest correlation with engagement velocity ($r_{abs} = 0.6663$ and $r_{norm} = 0.7684$). Form factor also exhibited moderate correlation to the engagement velocity ($r_{abs} = -0.6452$ and $r_{norm} = -0.7112$). At the patella, mild correlation was present across all vibration features except mean squared (Table 3.2 and Table 3.3). For the tibia signal, only mean squared had a correlation magnitude greater than 0.5 ($r_{norm} = -0.5570$). In the summation signal, mobility and form factor had r_{abs} values of 0.6419 and -0.6930 respectively. No other correlations for the summation signal were greater than 0.5.

3.4.3. Correlating Vibration to the Contact Point Height on Tibial Post

The Pearson Product-Moment Correlation coefficient between each target feature and the height of the contact point on the tibial post was also assessed. Coefficients were calculated for the normalized height (Table 3.4). The crest factor, PAPR, and envelope amplitude exhibited mild negative correlations for the medial femoral epicondyle signal. No significant correlations existed for any features derived from the patella signal. For the tibial tuberosity signal, mean squared and PAPR had correlation magnitudes greater than 0.5 (Table 3.4). The strongest correlations between the contact point height and the vibrations existed in the

Table 3.2. Correlation Between Signal Features and Absolute Cam-Post Engagement Velocity

Feature	Medial Femoral Epicondyle	Patella	Tibial Tuberosity	Summation
Mean Squared	0.0270	0.0838	-0.4548	-0.0743
Variance	-0.4737	-0.4966	-0.0204	-0.4213
Mobility	0.6663	0.5516	0.3068	0.6419
Form Factor	-0.6452	-0.5742	-0.2853	-0.6930
Crest Factor	0.2808	-0.6622	0.0426	-0.3326
PAPR	0.2625	-0.6493	0.0313	-0.2634
Envelope Amplitude	0.0360	-0.5919	-0.0704	-0.4277

Red values indicate negative correlations that are less than or equal to -0.5. Blue values indicate positive correlations that are greater than or equal to 0.5.

Table 3.3. Correlation Between Signal Features and Normalized Cam-Post Engagement Velocity

Feature	Medial Femoral Epicondyle	Patella	Tibial Tuberosity	Summation
Mean Squared	-0.0869	0.0438	-0.5570	-0.3179
Variance	-0.6016	-0.6089	0.4426	-0.2582
Mobility	0.7684	0.5974	-0.1187	0.3631
Form Factor	-0.7112	-0.5711	0.0417	-0.4988
Crest Factor	0.5834	-0.5845	0.2007	0.0376
PAPR	0.6471	-0.6278	0.1236	0.1396
Envelope Amplitude	0.0226	-0.6580	0.4457	-0.1135

Red values indicate negative correlations that are less than or equal to -0.5. Blue values indicate positive correlations that are greater than or equal to 0.5.

Table 3.4. Correlation Between Signal Features and Normalized Cam-Post Contact Height

Feature	**Medial Femoral Epicondyle**	**Patella**	**Tibial tuberosity**	**Summation**
Mean Squared	-0.1802	0.4163	-0.5928	0.1210
Variance	-0.4360	-0.3640	0.0372	-0.6363
Mobility	0.1806	-0.0251	0.2895	0.2634
Form Factor	-0.2785	0.1330	-0.2496	-0.1228
Crest Factor	-0.5043	-0.3923	-0.2808	-0.6046
PAPR	-0.5040	-0.3521	-0.5742	-0.6243
Envelope Amplitude	-0.5306	-0.1862	0.4457	-0.6330

Red values indicate negative correlations that are less than or equal to -0.5.

summation signal – variance, crest factor, PAPR, and envelope amplitude all had correlation magnitudes greater than 0.6 (Table 3.4).

3.5. Discussion

The design of the cam-post mechanism in a posterior-stabilized TKA can significantly alter surgical outcomes and functional performance. Since its inception in the mid-1970s this mechanism has evolved as findings from cadaver experiments, mechanical simulations, and computer simulations presented valuable insight on the efficacy of varying design rationales [82, 84, 86, 89, 95]. Such experiments are extremely useful in the evaluation of cam-post contact location, areas, and stresses. During the last decade, multiple groups have utilized fluoroscopy and 3D-to-2D registration techniques to study cam-post design factors and resulting kinematics in vivo. Specifically, measurements have included the knee flexion angle at the time of cam-post engagement, the distance between the cam and post throughout a full range of motion, and the height of the contact point on the post [81, 83, 85, 87, 88]. Although this method has proven to be useful in a research environment, it does not transfer well to a clinical setting. Fluoroscopy is inconvenient, and it exposes subjects to ionizing radiation. In addition, the process of extracting kinematics via 3D-to-2D registration is a time-consuming technique. Thus, even though the method provides valuable information, it remains limited to academic use. Given this predicament, it is reasonable to investigate other technologies that may provide similarly useful information to that derived from fluoroscopic evaluation. Recently it was suggested that vibrations measured at the knee joint may correlate with the contact mechanics of the cam-post mechanism in a posterior-stabilized knee [38]. In this preliminary research, qualitative evaluation of selected cases was presented as evidence. In the present investigation, vibroarthrography is further considered for its ability to objectively describe cam-post mechanics in a modern posterior-stabilized TKA.

Three assessments were conducted to evaluate relationships between vibroarthrographic features and cam-post mechanics that were measured using fluoroscopy and 3D-to-2D registration. The first assessment sought to determine if the time of cam-post engagement could be reasonably approximated by vibrations. Although there was a small sample size, the presented methods resulted in evaluation of 756 data points (9 deep knee bends x 4 vibration signals x 7 features x 3 window lengths). From the boxplots it appears that cam-post engagement may be reasonably approximated from the envelope amplitude and/or the variance of the summation signal when a window size of 10 samples (0.001 seconds) it used. For this window size, both features had a median error of -0.630 seconds and an average error of -0.745 seconds. Perhaps more importantly, the data for these features and this window size was well concentrated. The box height (interquartile range) for these conditions was smaller than any other scenario. Additionally, when two data points that are statistical outliers are removed, all the data has an error magnitude less than or equal to 1.593 seconds. Another set of features worth highlighting is the crest factor and/or PAPR of the summation signal for a window size of 1000 samples (0.1 seconds). Under these conditions, these two features exhibited their lowest error (median error = 0.193 seconds) and smallest box height (2.187 seconds). When considering the entire set of data, the summation of the three signals outperforms its individual components in this assessment. With regards to window size, it is not clear if a smaller or larger window will yield better accuracy. Some features performed better with the smallest window size (i.e. envelope amplitude and variance) while others benefited from the increased window size (i.e. crest factor and PAPR).

Considering that the average speed at which the deep knee bend was performed in this investigation (9.69 °/sec ± 2.05 °/sec) was relatively slow, the error associated with some of the features relative to the knee flexion domain are tolerable. The duration of the 5° *target* window in which engagement was known to occur ranged from 0.467 seconds to 0.901 seconds. The median *target* window was 0.634 seconds and the average *target* window was 0.664 sec ± 0.138 sec. These are both greater than the median error associated with the variance and the envelope amplitude features for the summation signal with a window size of 0.001 seconds (0.630). Similarly, the median error for crest factor and PAPR in the summation signal with a window size of 0.1 seconds (0.193 seconds) is substantially smaller than both the median *target* window and the average *target* window. In this context it is plausible that under the proper conditions, these features may be able to predict cam-post engagement to within 5 degrees of its occurrence.

The second assessment investigated the correlation between vibration features and cam-post engagement velocity. Cam-post engagement velocity was first described by Fitzpatrick et al. and investigated during a squat activity in cadaver specimens and a finite element model [86]. Four fresh-frozen, healthy cadaveric knees were implanted with the Sigma TKA knee system (DePuy, Warsaw, IN, USA) by an experienced surgeon. A deep knee bend was mechanically simulated, and kinematics were tracked with a motion analysis system. The average experimental cam-post engagement velocity was reported as 0.27 ± 0.1 mm/° [86]. In the finite element model, Fitzpatrick et al. calculated the cam-post engagement velocity for eight different PS TKA designs, including the Attune®. Using this method, the reported cam-post engagement velocities ranged from 0.05 to 0.22 mm/° [86]. The engagement velocity reported for the Attune® was approximately 0.113 mm/°. Among the motivation for measuring cam-post engagement velocity is the clicking that is described by PS TKA subjects. Fitzpatrick et al. suggested that these clicking sensations may be due to excessive cam-post impact velocity.

In the present research the methods presented by Fitzpatrick et al. were adapted to explore in vivo cam-post engagement velocity for the first time. Once measured, the engagement velocity was correlated to vibrations measured at the joint surface to see if any relation existed that may further support this theory.

In line with Fitzpatrick et al. findings, the cam-post engagement velocity in the present work ranged from 0.076 mm/° to 0.364 mm/°. The average cam-post engagement velocity was 0.218 ± 0.092 mm/°. Mild correlations existed between some of the calculated vibration features and the cam-post engagement velocity. Considerable correlations (greater than 0.5 in magnitude) were most prevalent in the medial femoral epicondyle signal and the patella signal. Both mobility and form factor correlated well (greater than 0.7 in magnitude) with impact velocity. In the patella signal every feature except for mean squared had a correlation coefficient magnitude greater than 0.55. Interestingly, when looking at the velocity in millimeters per degree of flexion, none of the features in the summation signal had strong correlation coefficients. Similarly, the tibial tuberosity signal was lacking in relevant correlation when compared to the medial femoral epicondyle and/or the patella signal. The correlations at the medial femoral epicondyle and the patella do suggest that the impact velocity is related to the vibrations or sounds emitted from the joint. In these two signals, three features (variance, mobility, and form factor) exhibited consistent patterns. A positive correlation with impact velocity existed for variance and form factor in both signals, and a negative correlation existed for mobility in both signals. These three features describe variability or a derivative of variability in the signal. It is logical that an impact such as cam-post engagement would result in an impulse signal that would affect the magnitude of these features. Furthermore, it is reasonable to assume that increases in velocity would result in increased transfer of momentum within the system. This in turn may increase the magnitude of the impulse signal associated with the impact. Although none of the subjects in this investigation explicitly described the “clicking” sensations, the collision of two rigid bodies (cam and post) will emit characteristic vibrations that may be detected with proper techniques. These characteristic vibrations are expected to vary based on subject and TKA design. The Attune® has been designed to minimize instabilities and encourage seamless mechanics through a complete range of motion. The sagittal plane condylar geometry of the Attune® incorporates a gradually reducing radius that has been shown to reduce discrete discontinuities or abrupt changes in the helical axis [96]. This combined with the curvature and relative conformity of the cam-post mechanism promotes a theoretically smooth engagement. Therefore, it may be expected that the vibrations elicited by the highly optimized Attune® may be less than other legacy TKA devices.

The final assessment investigated the relationship between vibrations and the height of the contact point on the tibial post. In this assessment the only relevant correlations were negative. The strongest correlations were present in the summation signal. As the height of the contact point on the post increased variance, crest factor, PAPR, and envelope amplitude all decreased. In attempt to explain this the post is considered a highly rigid cantilever. As the point of contact moves away from the base of the post the primary frequencies of the resulting vibrations decrease. Depending on the wavelength of these vibrations it is possible that some components were removed from the signal by the cascade moving average filter. This would result in a more consistent waveform and less signal variance. Variance, crest factor, PAPR, and the envelope amplitude are well suited to detect abrupt high frequency transients that are distinguishably unique from the baseline signal. Thus, it is logical that these features decrease in magnitude if the resulting vibrations were relatively harmonic and/or locally stable in comparison to those that manifested from an impact near the base of the post.

3.6. Conclusion

All three of the assessments presented here were performed to investigate the usefulness of vibroarthrography in describing cam-post contact mechanics in a PS TKA. The methods described and tested in this pilot research had mild success and are repeatable. However, they can certainly be improved upon. The spread of data, presence of outliers, and absence of strong correlations is concerning. These shortcomings suggest that the methods may only be applicable to certain subjects or that the vibrations are significantly impacted by factors that were not accounted for. Some factors that may inhibit the ability of the methods presented here include attenuation of the signal from soft tissue and noise induced from other physiological mechanisms (muscle contractions, snapping tendons, crepitus, etc.). Ultimately a larger set of data consisting of various TKA designs is required to validate the methods presented here. Additionally, it would be optimal to study the applicability of these methods at more realistic activity speeds rather than the slow speeds that characterize the present data set. Lastly, this research only utilized the cascade moving average filter to post-process the raw signals. Additional research may focus on testing other signal processing techniques to optimize the assessments described here.

CHAPTER 4. MEASURING THE MECHANICAL EFFECTIVENESS OF VISCOSUPPLEMENTATION IN OSTEOARTHRITIC KNEES

Raw data for this research was collected at the OhioHealth Grant Medical Center (Columbus, Ohio) by Trevor Grieco. All final analyses were conducted by Trevor Grieco at the University of Tennessee.

4.1. Abstract

Viscosupplementation of the osteoarthritic knee via intra-articular injection of hyaluronic acid remains a controversial treatment for symptomatic patients. Currently, conflicting results and clinically irrelevant effects are a cause of uncertainty among major orthopaedic societies when it comes to recommending this treatment. This investigation was designed to investigate vibroarthrography's ability to provide unique metrics that may be used to supplement future evaluation of this treatment. It was expected that after injection vibroarthrographic features would be more normal like than their respective preoperative features.

Six osteoarthritic knees were evaluated at multiple time points prior to and after viscosupplementation. Vibroarthrography was used to measure signals at five anatomic locations during a chair rise activity. These locations included 1) tibial tuberosity, 2) medial tibial condyle, 3) patella, 4) medial femoral epicondyle, and 5) lateral femoral epicondyle. The variance of the means squared (VMS), form factor (FF), turns count adaptive threshold (TC-AT), turns count fixed threshold (TC-FT) and the envelope amplitude average (EAA) were derived from the vibration signals. These features were compared to clinically relevant information from electronic medical records to interpret changes within subjects and across the subject sample.

VMS and TC-AT exhibited the best agreement with clinical observations. Post-operative decreases in these two features often presented in the medial tibial condyle site and the medial femoral epicondyle site for subjects reported to have significant medial compartment degeneration. These features also decreased in the patellofemoral site for the one subject who was reported to have severe osteoarthritis at the patella.

Although some patterns of interest existed on a case by case basis, the sample size was too small, and the follow-up rate was insufficient to conclude that any definitive relationships existed between the vibration signals and the treatment.

4.2. Introduction

It has been estimated that knee osteoarthritis (OA) affects 14 million people in the United States and more than 250 million people worldwide [97, 98]. This disease can affect the entire synovial joint [98], and subjects may experience pain, aching, stiffness and functional loss due to soft tissue damage and the presence of bone on bone contact (Figure 4.1 and Figure 4.2) [97]. Muscle atrophy, bone remodeling and sclerosis, cartilage degeneration, synovial hypertrophy, ligament dysfunction, meniscal damage, and osteophytes all contribute to the debilitating symptoms associated with OA [98]. Current conservative treatment options such as knee braces, physical therapy and nonsteroidal anti-inflammatory drugs (NSAIDS) are limited in their ability to hinder disease progression and/or provide long term symptom relief [97]. If eventually all these traditional treatments fail to relieve OA symptoms, intra-articular hyaluronic acid (HA) injections may be considered [99].

HA, also known as hyaluronan or hyaluronate, is a naturally occurring substance found in the human body that is critical for cellular and tissue functions [98, 100]. Over the last thirty years it has been chemically modified to serve various clinical functions [100]. In synovial joints, endogenous HA enables synovial fluid to act as a lubricant or shock absorber [98, 101]. In the normal adult knee there is approximately 2 mL of synovial fluid with a hyaluronate concentration of 2.5 to 4.0 mg/mL [101]. One of the physiological mechanisms of OA is the depolymerization of hyaluronate [98, 101]. This depolymerization directly affects the intrasynovial half-life of hyaluronate. In a normal joint the average half-life has been reported to be approximately 20 hours, but in a diseased joint this may decrease by more than 40% (11 to 12 hours) [98]. Eventually this results in a significantly lower concentration of HA in the synovial fluid which ultimately reduces the fluid’s viscoelastic properties [98]. Therefore, as deficiencies in HA are responsible for the compromised rheological properties of synovial fluid, synthesizing it for

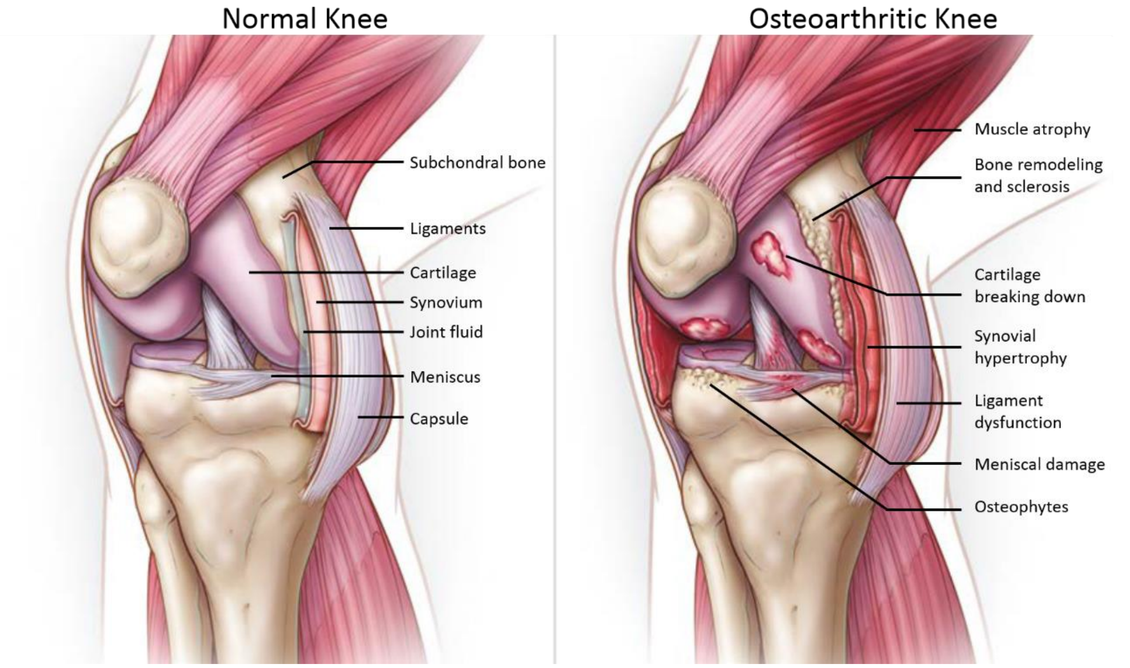

Figure 4.1. Osteoarthritis is a disease of the entire synovial joint. The schematic demonstrates how each structural part of the knee is affected by osteoarthritis (illustration courtesy of David J. Hunter [98]).

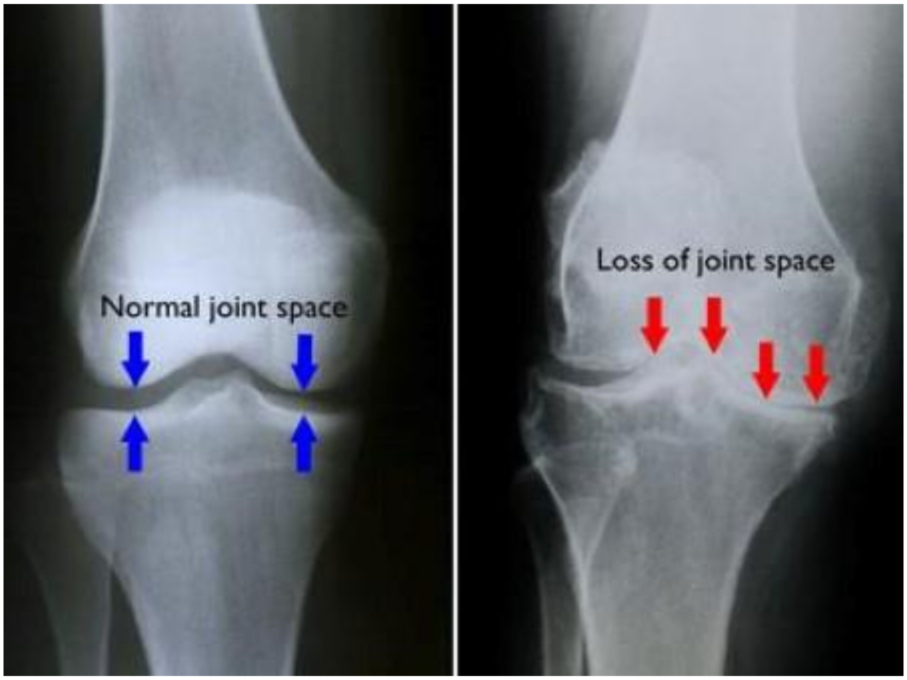

Figure 4.2. Anterior/Posterior X-rays illustrate the loss of joint space in an arthritic knee (right) compared to a normal knee (left) (illustration courtesy of OrthoInfo by the American Academy of Orthopaedic Surgeons [102]).

repeated injection may be considered a reasonable means of subsidizing an osteoarthritic knee.

Viscosupplementation via intra-articular HA injections has been in use in the United States since the late 1990’s [101]. This intra-articular injection of bioengineered HA may provide shock absorption, chondroprotection, and anti-inflammatory effects within the knee [98, 103]. Currently multiple formulations of these injections are commercially available and approved for use in the knee in the United States. Formulations range in molecular weight from 500 kDA to 6000 kDA [103], and manufacturing processes involve extraction of avian-derived molecules or bacterial processes of biological fermentation [103]. Initially the treatment was administered as a set of multiple injections over 3-5 weeks, but now it is commonly administered as a single injection. Studies have been conducted on the safety and efficacy of the intra-articular HA injections and findings suggest that certain characteristics of synthesized HA may result in more effective treatment than others [101, 103]. Some comparisons of viscosupplementation to corticosteroids, NSAIDS, and analgesics have reported that in the long term intra-articular HA provides better pain relief than conventional care, and that it is a cost-effective strategy [104, 105]. However, systematic reviews of the literature report conflicting results and clinically irrelevant effects [104, 106, 107]. Since 2013, the American Academy of Orthopaedic Surgeons (AAOS) has held the stance that they cannot recommend using HA for the treatment of knee OA due to the lack of clinically relevant evidence [108]. Similarly, the 2014 guidelines for the non-surgical treatment of knee OA presented by the Osteoarthritis Research Society International (OARSI) denote uncertainty in recommending intra-articular HA injections [109]. The healthcare economics associated with this treatment are equally questionable. It has been reported that HA injections account for 25% of treatment costs associated with nonoperative care for knee OA (greater percentage than any other treatment) [110], and in 2012 Medicare spent $207 million on HA products [111]. Accompanying the clinical and economic uncertainties is the fact that the ideal candidate for this treatment remains unclear [98, 99, 101]. Very recently it was reported that subjects with Kellgren-Lawrence (KL) grades of 1 or 2 were twice as likely to respond positively to the HA treatment compared to those with KL grade 3 OA [99]. Like other clinical investigations of this controversial treatment, these results were based on patient reported outcomes (Western Ontario and McMaster Universities Arthritis Index/Knee Injury and Osteoarthritis Outcome Score (WOMAC/KOOS) and a visual analogue scale were used to measure patient function and pain) [99].

To provide additional information of value regarding the use of intra-articular HA injections for the treatment of knee OA, the present research was proposed. In this research, instead of measuring the efficacy of the treatment by patient outcome scores, a mechanical approach was taken. Vibroarthrography has previously been utilized to noninvasively measure the mechanical interactions of healthy and diseased knees, but it has never been utilized to measure the effectiveness of a treatment. In these previous investigations various features demonstrated that normal knees exhibit less signal variance than diseased knees. Since the primary functions of viscosupplementation are mechanical in nature, it is a perfect candidate for the exploration of vibroarthrography’s application beyond screening. In accordance with the findings of normal and diseased knees, it was expected that the measurable differences in variance would exist between preoperative and postoperative signals measured in subjects undergoing intra-articular HA treatment.

4.3. Materials and Methods

4.3.1. Subject Recruitment

Vibroarthrography exams were conducted on a rolling basis as potential candidates were identified at initial and/or follow up visits to the Ohio Health Bone and Joint Center (Columbus, OH, USA). Symptomatic subjects who were between 18 and 85 years old and less than 250 pounds were informed of the opportunity to participate in this study. All interested subjects were consented by research personnel in accordance with the institutional review board approved clinical protocol. Once consented subjects were prepared for the Baseline vibroarthrographic exam.

4.3.2. Vibroarthrographic Exams and Treatment

Subjects were outfitted with an array of uniaxial accelerometers (352A24, PCB Piezotronics Inc., Depew, NY, USA) at the knee. These accelerometers are high sensitivity, miniature, integrated electronic piezoelectric (IEPE) accelerometers with a sensitivity of 100 mV/g, a measurement range of ±50 g pk, and a frequency range of 0.5 to 10000 Hz (±5%). The accelerometers were connected to a signal conditioner (482C05, PCB Piezotronics Inc., Depew, NY, USA) that provides constant-current power to connected sensors. The signal conditioner was configured to amplify all incoming signals by a factor of 10. Signal conditioner outputs were connected to a data acquisition device (DI-720-USB, DATAQ Instruments, Inc., Akron, OH, USA) that was used to log analogue inputs. Accelerometers were mounted to the tibial tuberosity, the medial tibial condyle, the medial femoral epicondyle, and the patella (Figure 4.3). Hypoallergenic medical tape was used to fix the accelerometers to the skin at these bony landmarks. The sensor cables were also taped above the knee prevent interference.

Subjects performed a sit-to-stand activity in which they steadily rose from a chair. Subjects started with the knee flexed to approximately 90° and subjects completed

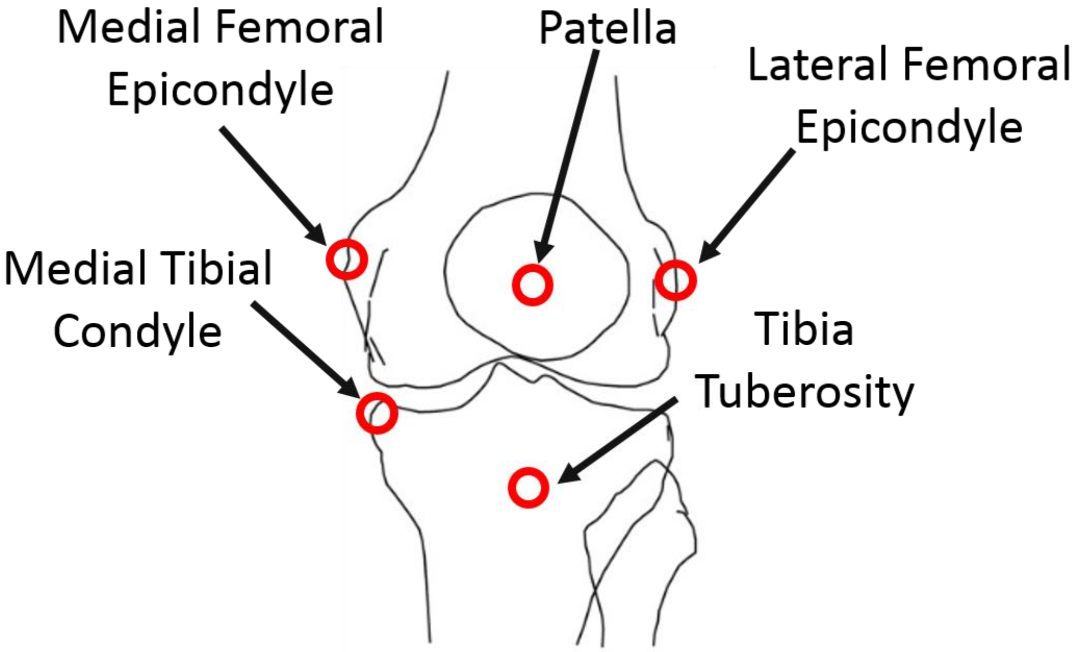

Figure 4.3. Accelerometers (denoted by red circles) were mounted at the medial femoral epicondyle, the medial tibial condyle, the patella, the lateral femoral epicondyle, and the tibial tuberosity.

the activity with the knee fully extended. Subjects were instructed to maintain their feet position during the activity to reduce signal artifact. If necessary, multiple trials were conducted to ensure the data was collected cleanly. All accelerometers were sampled at 10,000 Hz and the data was saved to a laptop hard drive for analysis. Six of the subjects enrolled in this study were scheduled to undergo viscosupplementation at the knee. All six of these subjects were diagnosed with medial tibiofemoral and/or patellofemoral compartment OA. Five subjects were treated with Synvisc-One® (Sanofi, Bridgewater NJ, USA) and one subject was treated with MONOVISC® (DePuy Mitek, Raynham, MA, USA). Treatment was conducted after the Baseline vibroarthrography exam. Aspiration of the joint was performed prior to the HA injection to remove any effusion that may have been present. Post injection (PostOp) vibroarthrography exams were conducted after the viscosupplementation treatment. The PostOp exam was conducted in identical fashion to the Baseline exam. Four subjects participated in PostOp exams on the same day of treatment. One subject returned for the PostOp exam one day after the Baseline exam, and one subject was unable to participate in the PostOp exam. An identical follow-up exam was conducted between Week 3 and Week 6. Only three of the six subjects returned for a follow-up exam during this visit window.

Although no clinical examination was performed per the study protocol, the medical history for all six subjects was thoroughly reviewed so that the state of each degenerative knee could be appropriately contextualized. Relevant clinical notes, imaging, physical exams, and joint evaluations provided valuable insight as to the location and severity of degeneration. This information was used to present vibroarthrographic results in a clinically relevant manner.

4.3.3. Vibration Signals Processing

First, extraneous data was cropped from the raw vibroarthrograms so that only the sit-to-stand activity was analyzed. Then the data was filtered using a cascade moving average filter (Figure 4.4). This filter serves to remove non-stationary low frequency signals that are caused by patient movement and or trembling that will interfere with vibration signals of interest (base-line wander) (Figure 4.5). The filter was constructed following an algorithm presented by Cai et al. [91]. This filter contains two layers. The first layer contains a *M*-order and a *N*-order moving average operator. The *K* inputs at the end of the *M*-order operator overlap the initial inputs of the *N*-order operator [91]. The second layer smooths the resulting piecewise linear trends obtained in the first layer. Both the *M* and *N* moving average operators were specified as 20th order operators. *K* was specified as 5 overlapping inputs. The final output as presented by Cai et al. is given as

$$y(i) = \frac{[o_1(i) + o_2(i)]}{2} = \frac{1}{2M}\sum_{m=1}^{M} x(i-m) + \frac{1}{2N}\sum_{n=1}^{N} x(i-M+K-n)$$

in which $o_1(i)$ and $o_2(i)$ are the *M* and *N* order moving average operators [91]. The transfer function $H(z)$ of this cascade moving average filter, similarly presented by Cai et al., is obtained by applying the *z*-transform to achieve

$$H(z) = \frac{Y(z)}{X(z)} = \frac{1}{2M}(z^{-1} + \cdots + z^{-M}) + \frac{1}{2N}(z^{-M+K-1} + \cdots + z^{-M+K-N})$$

Once filtered, the data was normalized from 0 to 1 (Figure 4.6A). Then the data was segmented into non-overlapping 5 millisecond windows (50 samples). The local maxima, local minima, and local mean squared were calculated for each window. The local maxima and local minima were used to calculate the envelope amplitude as described by Yang et al. [92]. In their research, the signal envelopes were defined by linear interpolation of the local minima and maxima. In the present work, Hermite interpolation (third order) was used to derive the upper envelope and lower envelope from the local maxima and local minima respectively (Figure 4.6B). Then the envelope amplitude was calculated as the difference between the

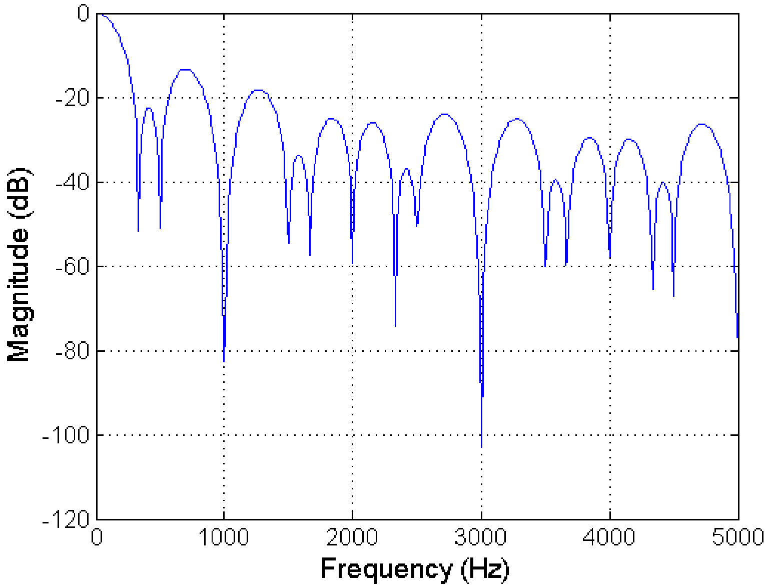

Figure 4.4 Cascade moving average filter frequency response.

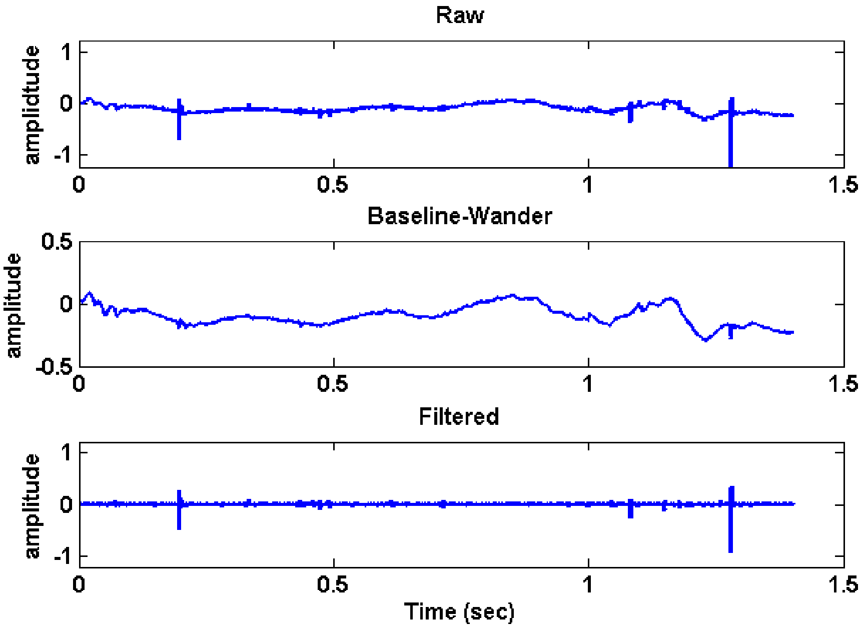

Figure 4.5. The raw signal (top) is passed through the cascade moving average filter to estimate and subtract the base-line wander (middle). Subtraction of base-line wander from the raw signal results in the filtered signal (bottom).

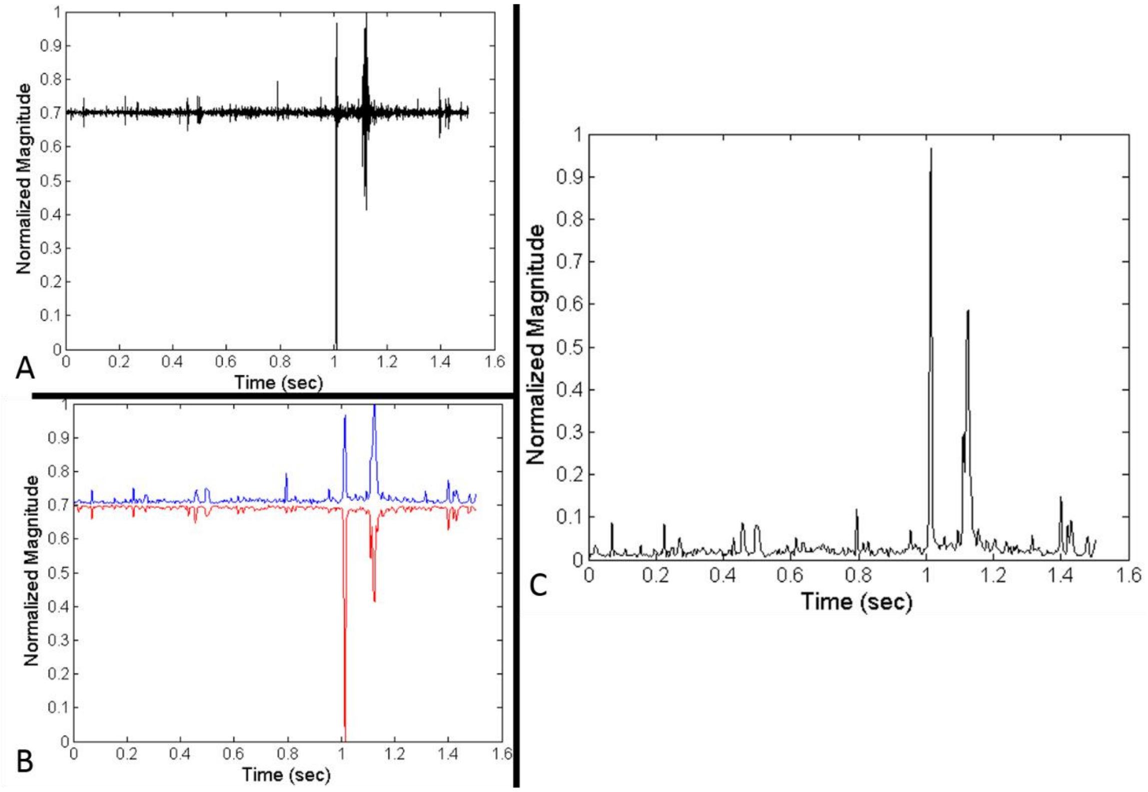

Figure 4.6. (A) The filtered signal is normalized from 0 to 1. (B) The upper (blue) and lower (red) signal envelopes are calculated and subtracted to obtain (C) the envelope amplitude.

upper and lower envelope at each interpolated point in time (Figure 4.6C). The average of the envelope amplitudes (EAA) was analyzed as a primary feature.

This feature describes the general fluctuation degree of a vibroarthrogram and was previously presented by Yang et al. for the screening of diseased knees [92]. The variance of the local means squared (VMS) was also analyzed. This parameter was first described as a feature for screening diseased knees by Rangayyan and Wu [27]. It effectively describes the degree of dispersion within the signal in a short time span [112].

Three other features were calculated for the duration of the activity. Form factor (FF) was calculated as described by Rangayyan and Wu [26]. FF describes the complexity or busyness of a signal and is derived from the standard deviations of the signal's first and second derivatives ($\sigma_{x'}$ and $\sigma_{x''}$)

$$FF = \frac{\sigma_{x''}/\sigma_{x'}}{\sigma_{x'}/\sigma_{x}}$$

The turns count was also calculated for the duration of each signal. The turns count is simply the number of times the difference between two consecutive samples is greater than a predefined threshold. This measure of variability was originally presented for the analysis of electromyography (EMG) by Willison [113]. More recently it has been used as a discriminant feature for classification of healthy and diseased knee vibroarthrograms [27, 114]. Rangayyan and Wu presented an adaptive threshold turns count based on the standard deviation of the signal. Using a threshold equal to one half of a signal's standard deviation (0.5σ), they demonstrated that the turns count of normal knees was greater than turns count of diseased knees. This is explained by the fact that normal knee signals were less variable than diseased knee signals. Less variance resulted in smaller thresholds which resulted in more counted turns. A few years later, Cai et al. tested the discriminant ability of a fixed threshold turns count on the basis that diseased knees should intuitively have more turns of significance (higher variability) than normal knees [114]. Using a fixed threshold equal to 0.2, this feature proved to be effective in discriminating normal from abnormal knee vibroarthrograms. Turns count with an adaptive threshold (TC-AT) and turns count with a fixed threshold (TC-FT) were calculated and analyzed in the present research. The adaptive threshold was defined as one half of a signal's standard deviation (Figure 4.7A). The fixed threshold was defined as 0.05 (Figure 4.7B).

Since only a small number of subjects were investigated in this pilot study, the results were presented on a case by case basis. Features derived from signals measured at the closest proximity to the diseased location(s) were assessed for change between Baseline and subsequent vibroarthrographic exams. The percent difference with respect to Baseline was reported as the primary endpoint for features of interest. The raw feature data derived from signals measured at each of the five anatomic locations is presented in Appendices A, B, C, D, and E.

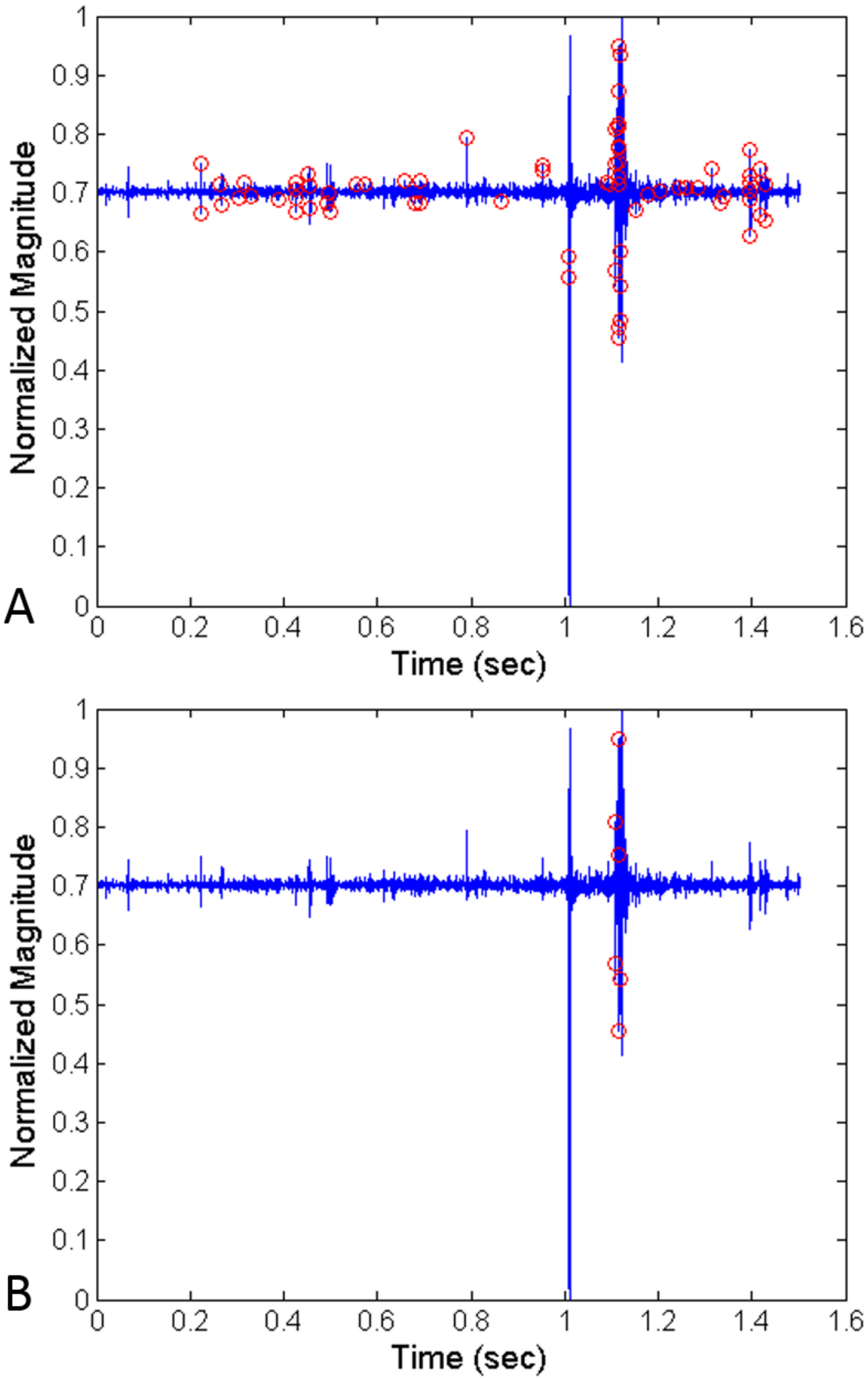

Figure 4.7. (A) Red circles denote turns greater than the adaptive threshold of 0.5σ. (B) Red circles denote turns greater than the fixed threshold of 0.05.

4.4. Results

4.4.1. Subject 001

Subject 001 experienced chronic knee pain and X-ray findings indicated prominent narrowing in the medial compartment. Vibrations for subject 001 were measured at Baseline and PostOp. The PostOp exam was conducted on the same day as the Baseline exam following injection of Synvisc-One®. All features derived from the accelerometer positioned at the medial tibial condyle exhibited a decrease in magnitude postoperatively. The VMS decreased by 94.57%, FF decreased by 35.96%, TC-AT decreased by 91.81%, TC-FT decreased by 80.00%, and the EAA decreased by 84.75%. All five features derived from the accelerometer positioned at the medial femoral epicondyle also exhibited decreases in magnitude from Baseline to PostOp. VMS decreased by 94.86%, FF decreased by 1.21%, TC-AT decreased by 57.62%, TC-FT decreased by 91.30%, and EAA decreased by 78.31%.

4.4.2. Subject 002

Subject 002 experienced chronic knee pain and X-ray findings indicated moderate medial cartilage loss. Vibrations for subject 002 were measured at Baseline and PostOp. The PostOp exam was conducted on the same day as the Baseline exam following injection of Synvisc-One®. Following treatment, four of the five features calculated from the accelerometer positioned at the medial tibial condyle decreased in magnitude. VMS decreased by 92.49%, FF decreased by 41.12%, TC-AT decreased by 23.56%, and EAA decreased by 38.97%. At the medial femoral epicondyle site, only VMS and TC-AT decreased postoperatively. VMS decreased by 7.91% and TC-AT decreased by 36.98%.

4.4.3. Subject 003

Subject 003 experienced medial joint line tenderness. Baseline X-ray findings indicated bone on bone contact and significant spurring in the medial tibiofemoral compartment. Vibrations for subject 003 were measured at Baseline and Week 3. Following the Baseline exam, the subject was treated with Synvisc-One®. No immediate PostOp exam was collected. The Week 3 follow up visit was scheduled due to increased pain since treatment. X-ray findings indicated tibiofemoral subluxation that was not previously reported at Baseline. At the medial tibial condyle site VMS, FF, TC-AT, TC-FT, and EAA all increased from Baseline to Week 3. VMS increased by 984.70%, FF increased by 7.51%, TC-AT increased by 7.11%, TC-FT increased by 114.16%, and EAA increased by 22.50%. At the medial femoral epicondyle site VMS, TC-AT, TC-FT, and EAA increased from Baseline to Week 3. VMS increased by 958.92%, TC-AT increased by 380.59%, TC-FT increased by 185.00%, and EAA increased by 34.27%.

4.4.4. Subject 004

Subject 004 experienced medial joint line tenderness, had a history of chronic medial knee pain, and reported loud popping noises. X-ray findings indicated degeneration of the medial tibiofemoral compartment and the patellofemoral compartment. Loud popping noises were suspected to be associated with locking and catching of menisci and/or ligaments. Observations from MR imaging included high-grade articular cartilage loss in the central weight-bearing surface of the medial femoral condyle as well as moderate to high-grade articular cartilage loss in the central trochlea. No evidence of meniscal or ligament tear was found.

Vibrations for subject 004 were collected at Baseline, PostOp, and Week 6. The PostOp exam was conducted on the same day as Baseline following injection of Synvisc-One®. Based on the medical history, signals of interest included those measured at the medial femoral epicondyle and the patella.

From Baseline to PostOp FF, TC-AT, and EAA decreased at the medial femoral epicondyle site by 32.22%, 54.15%, 78.10% and 38.72% respectively. All six features derived from the medial femoral epicondyle signal decreased from Baseline to Week 6. VMS decreased by 60.23%, FF decreased by 36.40%, TC-AT decreased by 29.13%, TC-FT decreased by 80.00%, and EAA decreased by 64.89%.

From Baseline to PostOp VMS, FF, and TC-AT decreased at the patella site. VMS decreased by 69.18%, FF decreased by 1.16%, and TC-AT decreased by 23.66%. From Baseline to Week 6, VMS decreased by 94.11%, FF decreased by 13.23%, TC-AT decreased by 76.33%, TC-FT decreased by 40%, and EAA decreased by 57.26%.

4.4.5. Subject 005

Subject 005 experienced years of chronic knee pain. The pain was reported to be constant, severe, aching pain. X-ray findings indicated a varus deformity and severe osteoarthritis with bone on bone contact in the medial compartment. The subject failed conservative measures and was prescribed viscosupplement treatment as a final measure before resorting to TKA. Vibrations were collected at Baseline, PostOp, and Week 6. The PostOp exam was conducted on the same day as Baseline following injection of MONOVISC®. Progression of the disease/symptoms was noted at Week 6, and the subject underwent total knee arthroplasty (TKA) approximately 16 weeks after the Baseline exam. Operative notes from TKA describe dissection of synovium scarring from the anterior femur and the removal of osteophytes from the femoral notch.

From Baseline to PostOp VMS, TC-AT, and TC-FT decreased at the medial tibial condyle site. VMS decreased by 89.78%, TC-AT decreased by 54.13%, and TC-FT decreased by 68.89%. From Baseline to Week 6 VMS, FF, TC-AT, and EAA decreased at the medial tibial condyle site. VMS decreased by 91.93%, FF decreased by 33.10%, TC-AT decreased by 54.32% and EAA decreased by 13.10%.

At the medial femoral epicondyle site most features increased in magnitude compared to their Baseline values. Only FF decreased from Baseline to PostOp (14.32%), and no features decreased from Baseline to Week 6. At the lateral femoral epicondyle site all features measured at PostOp and Week 6 were at higher levels than the respective Baseline values.

At the patella site, VMS, FF, TC-AT, and TC-FT decreased from Baseline to PostOp. VMS decreased by 81.55%, FF decreased by 12.84%, TC-AT decreased by 45.83% and TC-FT decreased by 28.57%. Only TC-FT decreased between PostOp and Week 6 at the patella site. All other features derived from the patella signal increased in magnitude between PostOp and Week 6. By Week 6, FF and TC-AT had increased to levels that surpassed their respective values calculated at Baseline (Week 6 FF increased by 62.10% with respect to Baseline and Week 6 TC-AT increased by 90.83% with respect to Baseline). Although VMS increased from PostOp to Week 6, it was still down compared to its Baseline value (52.75%).

4.4.6. Subject 006

Subject 006 experienced months of moderate joint pain and was nonresponsive to conservative pain management. X-ray findings indicated bone on bone contact in the medial tibiofemoral compartment and polar spurring on the patella. Vibrations for subject 006 were measured at Baseline and PostOp. Following the Baseline exam, the subject was treated with Synvisc-One®. The PostOp exam was conducted one day after treatment. At the medial tibial condyle site, only FF, TC-AT, and EAA decreased in magnitude from Baseline to PostOp. FF decreased by 6.63%, TC-AT decreased by 23.16%, and EAA decreased by 16.73%. At the medial femoral epicondyle site, no features decreased from Baseline to PostOp. At the patella site, only FF decreased from Baseline to PostOp (2.52%).

4.5. Discussion

Past vibroarthrographic investigations of the native knee have focused on the screening of subjects with known knee degeneration. The same data set has been tested extensively by multiple groups in working towards the development of a clinical grade classifier [19, 20, 23, 25-29, 91, 92, 112, 114, 115]. Pre-processing and post-processing techniques have been well documented, and the success of classification has increased as new discriminant features are derived and tested. Instead of expounding further in the same exact direction, methods discussed in this wealth of literature were adopted to investigate the effectiveness of a treatment. Viscosupplementation remains a controversial and expensive treatment for the management of pain associated with arthritis. Fundamentally this treatment is intended to supplement the diseased joint by increasing the viscosity of the compromised synovial fluid. Bioengineered HA is injected into the joint capsule to cushion and protect the diseased articular surfaces. From a vibroarthrographic perspective, it is known that diseased joints exhibit increased signal variance compared to a healthy joint. Among various reasons for this, is the fact that diseased joints do not articulate as smoothly as healthy joints. Decreases in synovial fluid viscosity as well as the presence of cartilage lesions, joint space narrowing, osteophytes, torn menisci, and other intraarticular damage introduce mechanical defects into the once virtually frictionless system. When the defects are involved in joint articulation, fluctuations in the energy emitted can be measured with vibroarthrographic techniques. The clinical success of traditional pain management for knee OA (NSAIDS, corticosteroids, etc.) can only really be measured by subjective patient feedback. Unlike conservative treatments, viscosupplementation seeks to reduce pain through a quasi-mechanical patch.

Therefore, it is reasonable to consider objectively evaluating its effectiveness by mechanical testing. This is not to say that patient feedback and outcomes scores are an inadequate means of testing the quality of a treatment; rather it is to point out the unique opportunity to provide additional information that may be used in the assessment of the treatment's value.

This pilot study details the novel application of vibroarthrography for the investigation of viscosupplement treatment in diseased knees. The methods presented here are scalable, and patterns in the data warrant further investigation. Unfortunately, the sample size and follow up rate were critical factors that reduced the power of this pilot investigation. One subject was unable to participate in a PostOp exam, and only three subjects returned for follow-up exams between Week 3 and Week 6. Given these limitations, the data had to be presented on a case by case basis. At this early phase of the research, no statistically valid conclusions can be made between vibration related features and the effectiveness of the treatment across subjects or longitudinally. Aside from increasing the sample size, a future investigation needs to collect data more frequently across a six-month timeline. In such an investigation it is recommended that vibroarthrography exams be conducted at two-week intervals for the first three months and then monthly after that. Additionally, it would be valuable to collect a validated outcome score, such as the Knee Injury Osteoarthritis Outcome Score (KOOS), at each visit. It would also be ideal if Baseline imaging was required and standardized for all subjects. At the very least, anterior/posterior and lateral weight bearing X-rays as well as a skyline X-ray should be collected just prior to treatment. MR imaging at Baseline would also be extremely useful in the interpretation of vibration signals. Lastly it is important to note that there was a chance for error when administering the injection. If the treatment is not injected into the intraarticular joint space, it is wasted. Although in this investigation the injection was performed by a highly experienced orthopedic surgeon, the chance of error still existed, and there was no way of knowing with absolute certainty that the injection was properly delivered. Therefore, one may consider using image guidance (ultrasound or fluoroscopy) for the purposes of future research to ensure the treatment reaches its target.

Despite these limitations there are some findings worth noting. The first is the apparent relevance of certain features. Previous vibroarthrographic investigations have demonstrated that VMS, FF, TC-AT, TC-FT, and EAA are useful features in discriminating the difference between normal and diseased knees [26, 27, 92, 112, 114-116]. In these studies, it was found that all of these features except for TC-AT were significantly less in normal knees than in diseased knees. TC-AT is dependent on the definition of the adaptive threshold. In previous research and the present research, the adaptive threshold was set at one half the standard deviation of the activity signal [27]. Mathematically it makes sense that if a normal vibroarthrogram has less variance than a diseased vibroarthrogram the adaptive threshold will decrease, and ultimately more turns of significance may exist. In the present work, it was hypothesized that the PostOp vibroarthrogram would be more “normal” like than the Baseline vibroarthrogram. In accordance with this, it was expected that postoperative values of VMS, FF, TC-FT, and EAA would be less than their respective values at Baseline and TC-AT would be greater than its Baseline value.

Seemingly correlated relationships between clinical data and multiple vibration features presented in four of the six subjects. Subjects 001, 002, and 004 exhibited decreases in similar features postoperatively. In these subjects, VMS and TC-AT decreased postoperatively at the medial femoral epicondyle and the medial tibial condyle sites. These two features also decreased at the patella for Subject 004 who, in addition to medial degeneration, was reported to have high grade articular cartilage loss in the trochlea. VMS and TC-AT also appeared to reflect the clinical data for Subject 003. Unlike Subjects 001, 002, and 004, Subject 003's features increased postoperatively. Although unexpected, the increases in VMS and TC-AT at the medial tibial condyle and the medial femoral epicondyle sites align with adverse reports (increased pain and subluxation) in the clinical data. Aside from VMS and TC-AT, EAA and FF may be worth considering for use in future evaluations as changes in both features reflected clinically relevant interactions in most of the cases previously discussed. Together these cases provide some evidence that certain vibration features related to the overall signal variance fluctuate proportionately to clinically relevant interactions.

The relationships between vibration features and clinical interactions for subjects 005 and 006 were less clear. The main problem being that unlike the other subjects with medial degeneration, there was not agreement between features measured at both medial sites (tibial and femoral). At the medial tibial condyle site both subjects exhibited decreases in TC-AT, FF, and EAA postoperatively, but at the medial femoral epicondyle site the subjects saw virtually no postoperative decreases in vibration features (FF for Subject 005 was the only feature to decrease postoperatively). Since the sensors located at these sites are relatively close to each other, this discrepancy raises concerns. Primarily, it begs the question "were the sensors appropriately fixated to the bony landmarks and did anything interfere with the signals?". Precautions taken during data collection and review of the video footage as well as the raw data suggests that the data was adequately captured with no interference. However, it is possible that noise existed at Baseline in the medial tibial condyle signal that was not present at later time points. If the noise made it through the filter, then it would artificially inflate the signal features at Baseline resulting in false decreases at later time points. Similarly, if noise affected the medial femoral epicondyle signal at postoperative time points the apparent increase from Baseline features would be marked as erroneous. For the sake of future investigations, it is important to emphasize the fact that the instrumentation used in this research is highly sensitive, and the utmost care must be taken when collecting data to ensure the integrity of the analysis is not compromised.

The final aspect of this investigation worth noting is the behavior of TC-AT. Previously Rangayyan and Wu demonstrated that normal knee signals have more turns than abnormal knee signals when using the adaptive threshold 0.5σ. In the present work TC-AT often decreased postoperatively. This seems to be in direct disagreement with Rangayyan and Wu's work. If the treatment is expected to result in more normal knee signals, then the TC-AT should decrease. However, calculations present otherwise. A positive correlation between the adaptive turns count and signal variance existed across the subjects tested in this pilot investigation. The only explanation is that the threshold of 0.5σ was inadequate for discouraging significant turns in this sample of data. Furthermore, unlike Rangayyan and Wu who used this feature to discriminate between distinctly different cohorts, the feature in this work is being used for intra-subject comparisons within a small sample. Aside from these details, no other reasonable explanations can be made without additional monitoring of this feature across more time points in a larger number of subjects. Ultimately turns count is intended to measure the randomness of the signal, and the relationship between TC-AT and clinical interactions in this work remains an encouraging result that deserves further investigation in future work.

4.6. Summary

A pilot investigation into the use of vibroarthrography for the monitoring of a nonsurgical OA treatment has been presented for the first time. Although the data was not powerful enough to make clinically relevant conclusions about the mechanical efficacy of viscosupplementation in the osteoarthritic knee, this work does present a valuable foundation and methodology that can be expounded on. Unfortunately, this study was hindered by enrollment and follow up rates. Nevertheless, the work provided preliminary insight and prompted multiple recommendations that may be reasonably incorporated into future work. Ultimately vibroarthrography provides a new tool for the analysis of this controversial treatment. If properly paired with patient outcomes and medical imaging this tool has potential to provide new evidence in the debate on the clinical efficacy of intra-articular HA injections for the treatment of knee osteoarthritis.

4.7. Appendices

4.7.1. Appendix A: Tibial Tuberosity Raw Feature Data

Subject ID	Visit Label	Tibial Tuberosity				
		VMS	FF	TC-AT	TC-FT	EAA
001	Baseline	1.905E-05	2.802	131	8	0.0817
001	PostOp	8.369E-06	2.659	116	7	0.0446
002	Baseline	4.755E-05	2.138	842	84	0.1242
002	PostOp	3.666E-05	2.599	488	20	0.1084
003	Baseline	2.427E-06	1.270	430	11	0.0318
003	Week 3	1.554E-06	1.567	152	3	0.0289
004	Baseline	7.577E-07	1.504	379	12	0.0289
004	PostOp	4.326E-05	2.566	304	23	0.0718
004	Week 6	2.541E-06	1.609	1099	17	0.0546
005	Baseline	5.341E-06	1.772	648	111	0.0804
005	PostOp	1.373E-05	2.991	470	1	0.0662
005	Week 6	2.882E-05	3.240	71	3	0.0353
006	Baseline	1.436E-04	2.611	791	99	0.1761
006	PostOp	2.535E-05	1.595	984	143	0.1404

VMS = Variance of Means Squared; FF = Form Factor; TC-AT = Turns Count Adaptive Threshold; TC-FT = Turns Count Fixed Threshold; EAA = Envelope Amplitude Average; PAPR = Peak-to-Average Power Ratio.

4.7.2. Appendix B: Medial Tibial Condyle Raw Feature Data

Subject ID	Visit Label	Medial Tibial Condyle				
		VMS	**FF**	**TC-AT**	**TC-FT**	**EAA**
001	Baseline	2.207E-04	2.787	635	30	0.112
001	PostOp	1.198E-05	1.785	52	6	0.017
002	Baseline	1.121E-04	3.159	416	16	0.067
002	PostOp	8.416E-06	1.860	318	17	0.041
003	Baseline	6.571E-06	1.644	2293	113	0.113
003	Week 3	7.127E-05	1.768	2456	242	0.138
004	Baseline	4.899E-06	2.267	864	6	0.054
004	PostOp	3.756E-08	1.278	49	8	0.011
004	Week 6	9.746E-06	1.835	2168	15	0.067
005	Baseline	1.110E-05	1.696	1550	45	0.056
005	PostOp	1.134E-06	1.787	711	14	0.089
005	Week 6	8.950E-07	1.135	708	72	0.049
006	Baseline	2.387E-05	1.595	2486	272	0.177
006	PostOp	4.476E-05	1.490	1910	426	0.147

VMS = Variance of Means Squared; FF = Form Factor; TC-AT = Turns Count Adaptive Threshold; TC-FT = Turns Count Fixed Threshold; EAA = Envelope Amplitude Average; PAPR = Peak-to-Average Power Ratio.

4.7.3. Appendix C: Patella Raw Feature Data

Subject ID	**Visit Label**	**Patella**				
		VMS	**FF**	**TC-AT**	**TC-FT**	**EAA**
001	Baseline	1.368E-05	1.260	5327	1099	0.333
001	PostOp	3.450E-06	1.722	128	6	0.031
002	Baseline	1.080E-05	1.251	5300	1294	0.359
002	PostOp	2.299E-06	1.523	386	6	0.029
003	Baseline	6.682E-07	1.252	410	13	0.034
003	Week 3	7.221E-07	1.243	187	26	0.030
004	Baseline	1.446E-06	1.583	169	5	0.023
004	PostOp	4.458E-07	1.565	129	6	0.024
004	Week 6	8.514E-08	1.374	40	3	0.010
005	Baseline	1.495E-06	1.726	120	7	0.018
005	PostOp	2.759E-07	1.504	65	5	0.023
005	Week 6	7.063E-07	2.798	229	2	0.033
006	Baseline	2.627E-06	1.591	154	14	0.056
006	PostOp	2.879E-06	1.551	291	22	0.059

VMS = Variance of Means Squared; FF = Form Factor; TC-AT = Turns Count Adaptive Threshold; TC-FT = Turns Count Fixed Threshold; EAA = Envelope Amplitude Average; PAPR = Peak-to-Average Power Ratio. Purple shaded rows indicate features from corrupt data signals that were not used in analysis.

4.7.4. Appendix D: Lateral Femoral Epicondyle Raw Feature Data

Subject ID	**Visit Label**	**Lateral Femoral Epicondyle**				
		VMS	**FF**	**TC-AT**	**TC-FT**	**EAA**
001	Baseline	7.167E-07	1.851	299	2	0.0259
001	PostOp	2.343E-05	2.253	537	38	0.115
002	Baseline	1.175E-04	3.506	217	4	0.056
002	PostOp	5.936E-06	1.512	924	7	0.039
003	Baseline	7.479E-07	1.701	359	13	0.036
003	Week 3	8.298E-06	2.567	881	30	0.060
004	Baseline	1.218E-05	1.239	6720	1752	0.400
004	PostOp	2.633E-06	1.809	217	13	0.035
004	Week 6	1.564E-06	1.747	1130	14	0.043
005	Baseline	1.220E-06	2.003	20	1	0.016
005	PostOp	9.010E-05	2.102	1381	85	0.140
005	Week 6	6.505E-05	2.271	1325	163	0.149
006	Baseline	2.292E-04	3.345	303	17	0.057
006	PostOp	1.245E-05	1.654	1419	61	0.092

VMS = Variance of Means Squared; FF = Form Factor; TC-AT = Turns Count Adaptive Threshold; TC-FT = Turns Count Fixed Threshold; EAA = Envelope Amplitude Average; PAPR = Peak-to-Average Power Ratio. Purple shaded rows indicate features from corrupt data signals that were not used in analysis.

4.7.5. Appendix E: Medial Femoral Epicondyle Raw Feature Data

Subject ID	**Visit Label**	**Medial Femoral Epicondyle**				
		VMS	**FF**	**TC-AT**	**TC-FT**	**EAA**
001	Baseline	5.222E-05	2.025	998	46	0.101
001	PostOp	2.686E-06	2.001	423	4	0.022
002	Baseline	1.221E-05	1.769	822	28	0.077
002	PostOp	1.124E-05	1.952	518	47	0.083
003	Baseline	5.001E-06	2.153	474	20	0.056
003	Week 3	5.296E-05	1.720	2278	57	0.076
004	Baseline	2.337E-06	2.519	975	10	0.054
004	PostOp	9.755E-06	1.707	447	14	0.033
004	Week 6	9.317E-07	1.602	691	2	0.019
005	Baseline	1.622E-06	1.857	203	19	0.032
005	PostOp	6.413E-05	1.591	2150	324	0.179
005	Week 6	1.000E-04	2.634	765	65	0.118
006	Baseline	3.736E-07	1.586	770	7	0.038
006	PostOp	9.492E-05	2.148	1129	52	0.114

VMS = Variance of Means Squared; FF = Form Factor; TC-AT = Turns Count Adaptive Threshold; TC-FT = Turns Count Fixed Threshold; EAA = Envelope Amplitude Average; PAPR = Peak-to-Average Power Ratio.

CHAPTER 5. CONCLUSION

The development of vibroarthrography as a clinically relevant diagnostic tool remains ongoing. Previous research endeavors have demonstrated its potential at the knee, hip, and spine using in vitro and in vivo methods. The dynamic, noninvasive, and mechanically objective nature of vibroarthrography positions it uniquely amongst other diagnostic modalities. Although at this point vibroarthrography is unable to provide the level of detail seen in medical imaging, it can provide supplemental information about dynamic instabilities that otherwise may have remained undiagnosed. In contribution to the further development of vibroarthrography, this work presented three novel investigations that explored the applications of vibroarthrography at the knee and hip.

In a total hip simulator, it was found that vibroarthrography could be effectively used to distinguish approximately 1 mm differences in the microseparation of the femoroacetabular joint. Similar simulations have demonstrated that edge loading and subsequent femoral head reduction associated with this instability can result in distinct wear patterns that compromise the longevity of a total hip arthroplasty. Therefore, it is of interest to be able to detect and/or monitor the presence of this microseparation in vivo. The methods presented in the present work, are currently being incorporated into in vivo fluoroscopy investigations of healthy, diseased, and replaced hip kinematics to better understand the characteristic features of joint vibrations in relation to microseparation.

An in vivo investigation of cam-post contact mechanics and vibroarthrography demonstrated that features derived from the vibrations measured at the joint surface may be used to approximate the occurrence and nature of cam-post engagement. Various features were tested for their ability to identify a window in which cam-post engagement occurred as seen via 3D-to-2D registration. Additionally, vibration features were correlated to the velocity and height of cam-post engagement. Future investigations aimed at developing increased understanding of in vivo cam-post contact mechanics may adopt the methods presented here to evaluate the differences in cam-post design variables, dynamic variables, and resultant vibroarthrographic features.

Also, in this work, vibroarthrography was used to evaluate the mechanical efficacy of intra-articular HA injections for the treatment of knee OA. To the author’s knowledge, this is the first time any attempts have been made at utilizing vibroarthrography for the evaluation of a non-surgical treatment of knee OA. Ultimately, the results were inconclusive due to small sample size and poor follow-up rates. However, given the controversy that currently surrounds this treatment, the methods presented within should be used in future investigations of larger scale. Preliminary results suggest that patterns may exist between vibroarthrographic features and the treatment. Moving forward these vibroarthrographic features need to be investigated in relation to standardized outcome assessments and standardized imaging assessments at systematic time points over the course of six months to best demonstrate the merit of this application in vibroarthrography.

Vibroarthrography has potential to be a viable diagnostic tool for various musculoskeletal applications. Although it may never stand alone, its dynamic nature is unquestionably well suited for additional observation and/or monitoring of instabilities. Ongoing investigations seeking to define the accuracy and potential of vibroarthrography remain well justified as preventative medicine and accessible automated diagnostic systems continue to shape the healthcare landscape.

REFERENCES

[1] Chu M, Gradisar I, Mostardi R. Noninvasive electro-acoustical evaluation technique of cartilage damage in pathological knee joints. Medical & Biological Engineering & Computing 16(4): 437-42, 1978

[2] Chu M, Gradisar I, Bowling G, Zavodney LD. Computer aided acoustical correlation of pathological cartilage generated noise. 1977

[3] Kernohan WG, Mollan RAB. Microcomputer analysis of joint vibration. Journal of Microcomputer Applications 5(4): 287-96, 1982

[4] Kernohan WG, Beverland DE, McCoy GF, Hamilton A, Watson P, Mollan R. Vibration arthrometry - a preview. Acta Orthopaedica Scandinavica 61(1): 70-9, 1990

[5] Kernohan W, Barr D, McCoy G, Mollan R. Vibration arthrometry in assessment of knee disorders: The problem of angular velocity. Journal of biomedical engineering 13(1): 35-8, 1991

[6] McCoy GF, McCrea JD, Beverland DE, Kernohan WG, Mollan RAB. Vibration arthrography as a diagnostic-aid in diseases of the knee - a preliminary-report. Journal of Bone and Joint Surgery-British Volume 69(2): 288-93, 1987

[7] Kernohan WG, Trainor BP, Haugh PE, Johnston AF, Mollan RAB. The belfast hip screener - from infancy to maturity. Ulster Medical Journal 61(2): 151-6, 1992

[8] Kernohan WG, Trainor BP, Mollan RA, Normand CE. Cost-benefit appraisal of screening for congenital dislocation of the hip. Journal of Management in Medicine 4(4): 230-5, 1990

[9] Imrie M, Scott V, Stearns P, Bastrom T, Mubarak SJ. Is ultrasound screening for ddh in babies born breech sufficient? Journal of children's orthopaedics 4(1): 3-8, 2010

[10] Pediatrics AAo. Committee on quality improvement, subcommittee on developmental dysplasia of the hip. Clinical practice guideline: Early detection of developmental dysplasia of the hip. Pediatrics 105(4 pt 1): 896-905, 2000

[11] Schwend RM, Schoenecker P, Richards BS, Flynn JM, Vitale M. Screening the newborn for developmental dysplasia of the hip: Now what do we do? Journal of Pediatric Orthopaedics 27(6): 607-10, 2007

[12] Rangayyan RM, Frank CB, Bell GD, Smith R. Analysis of knee-joint sound signals. Proceedings of the Annual International Conference of the Ieee Engineering in Medicine and Biology Society, Pts 1-4: 712-3, 1988

[13] Frank CB, Rangayyan RM, Bell GD. Analysis of knee-joint sound signals for noninvasive diagnosis of cartilage pathology. Ieee Engineering in Medicine and Biology Magazine 9(1): 65-8, 1990

[14] Tavathia S, Rangayyan RM, Frank CB, Bell GD, Ladly KO, Zhang YT. Analysis of knee vibration signals using linear prediction. Ieee Transactions on Biomedical Engineering 39(9): 959-70, 1992

[15] Ladly K, Frank C, Bell G, Zhang Y, Rangayyan R. The effect of external loads and cyclic loading on normal patellofemoral joint signals. Defence Science Journal 43(3): 201, 1993

[16] Zhang YT, Rangayyan RM, Frank CB, Bell GD. Adaptive cancellation of muscle-contraction interference in vibroarthrographic signals. Ieee Transactions on Biomedical Engineering 41(2): 181-91, 1994

[17] Shen Y, Rangayyan RM, Bell GD, Frank CB, Zhang YT, Ladly KO. Localization of knee-joint cartilage pathology by multichannel vibroarthrography. Medical Engineering & Physics 17(8): 583-94, 1995

[18] Moussavi ZM, Rangayyan RM, Bell GD, Frank CB, Ladly K. Screening of vibroarthrographic signals via adaptive segmentation and linear prediction modeling. IEEE transactions on biomedical engineering 43(1): 15, 1996

[19] Krishnan S, Rangayyan RM, Bell GD, Frank CB, Ladly KO. Adaptive filtering, modelling and classification of knee joint vibroarthrographic signals for non-invasive diagnosis of articular cartilage pathology. Medical & Biological Engineering & Computing 35(6): 677-84, 1997

[20] Rangayyan RW, Krishnan S, Bell GD, Frank CB, Ladly KO. Parametric representation and screening of knee joint vibroarthrographic signals. Ieee Transactions on Biomedical Engineering 44(11): 1068-74, 1997

[21] Krishnan S, Rangayyan RM. Automatic de-noising of knee-joint vibration signals using adaptive time-frequency representations. Medical & Biological Engineering & Computing 38(1): 2-8, 2000

[22] Krishnan S, Rangayyan RM, Bell GD, Frank CB. Sonification of knee-joint vibration signals. In: Enderle JD, ed. Proceedings of the 22nd annual international conference of the ieee engineering in medicine and biology society, vols 1-4. 1995-8. 2000

[23] Krishnan S, Rangayyan RM, Bell GD, Frank CB. Adaptive time-frequency analysis of knee joint vibroarthrographic signals for noninvasive screening of articular cartilage pathology. Ieee Transactions on Biomedical Engineering 47(6): 773-83, 2000

[24] Krishnan S, Rangayyan RM, Bell GD, Frank CB. Auditory display of knee joint vibration signals. Journal of the Acoustical Society of America 110(6): 3292-304, 2001

[25] Umapathy K, Krishnan S. Modified local discriminant bases algorithm and its application in analysis of human knee joint vibration signals. Ieee Transactions on Biomedical Engineering 53(3): 517-23, 2006

[26] Rangayyan RM, Wu YF. Screening of knee-joint vibroarthrographic signals using statistical parameters and radial basis functions. Medical & Biological Engineering & Computing 46(3): 223-32, 2008

[27] Rangayyan RM, Wu Y. Analysis of vibroarthrographic signals with features related to signal variability and radial-basis functions. Annals of Biomedical Engineering 37(1): 156-63, 2009

[28] Rangayyan RM, Wu YF. Screening of knee joint vibroarthrographic signals using probability density functions estimated with parzen windows. Biomedical Signal Processing and Control 5(1): 53-8, 2010

[29] Rangayyan RM, Oloumi F, Wu YF, Cai SX. Fractal analysis of knee-joint vibroarthrographic signals via power spectral analysis. Biomedical Signal Processing and Control 8(1): 23-9, 2013

[30] Reddy NP, Rothschild BM, Mandal M, Gupta V, Suryanarayanan S. Noninvasive acceleration measurements to characterize knee arthritis and chondromalacia. Annals of biomedical engineering 23(1): 78-84, 1995

[31] Reddy NP, Rothschild BM, Verrall E, Joshi A. Noninvasive measurement of acceleration at the knee joint in patients with rheumatoid arthritis and spondyloarthropathy of the knee. Annals of Biomedical Engineering 29(12): 1106-11, 2001

[32] Kawchuk GN, Decker C, Dolan R, Fernando N, Carey J. The feasibility of vibration as a tool to assess spinal integrity. Journal of Biomechanics 41(10): 2319-23, 2008

[33] Kawchuk GN, Decker C, Dolan R, Carey J. Structural health monitoring to detect the presence, location and magnitude of structural damage in cadaveric porcine spines. Journal of Biomechanics 42(2): 109-15, 2009

[34] Decker C, Prasad N, Kawchuk GN. The reproducibility of signals from skin-mounted accelerometers following removal and replacement. Gait & Posture 34(3): 432-4, 2011

[35] Kawchuk GN, Hartvigsen J, Edgecombe T, Prasad N, van Dieen JH. Structural health monitoring (vibration) as a tool for identifying structural alterations of the lumbar spine: A twin control study. Scientific Reports 6, 2016

[36] Glaser D, Komistek RD, Cates HE, Mahfouz MR. Clicking and squeaking: In vivo correlation of sound and separation for different bearing surfaces. Journal of Bone and Joint Surgery-American Volume 90A: 112-20, 2008

[37] Glaser DA. Development and implementation of mathematical modeling, vibration and acoustic emission technique to correlate in vivo kinematics, kinetics and sound in total hip arthroplasty with different bearing surfaces. In.: University of Tennessee. 2008

[38] Zingde SM. In vivo mechanics of cam-post engagement in fixed and mobile bearing tka and vibroarthrography of the knee joint. In.: University of Tennessee. 2015

[39] Leszko F. Dynamics, electromyography and vibroarthrography as non-invasive diagnostic tools: Investigation of the patellofemoral joint. In.: University of Tennessee. 2011

[40] Gomez PF, Morcuende JA. A historical and economic perspective on sir john charnley, chas f. Thackray limited, and the early arthroplasty industry. The Iowa orthopaedic journal 25: 30, 2005

[41] Hua X, Li J, Wang L, Jin Z, Wilcox R, Fisher J. Contact mechanics of modular metal-on-polyethylene total hip replacement under adverse edge loading conditions. Journal of biomechanics 47(13): 3303-9, 2014

[42] Yoon Y-S, Hodgson AJ, Tonetti J, Masri BA, Duncan CP. Resolving inconsistencies in defining the target orientation for the acetabular cup angles in total hip arthroplasty. Clinical Biomechanics 23(3): 253-9, 2008

[43] Abdel MP, von Roth P, Jennings MT, Hanssen AD, Pagnano MW. What safe zone? The vast majority of dislocated thas are within the lewinnek safe zone for acetabular component position. Clinical Orthopaedics and Related Research® 474(2): 386-91, 2016

[44] Dennis DA, Komistek RD, Northcut EJ, Ochoa JA, Ritchie A. “In vivo” determination of hip joint separation and the forces generated due to impact loading conditions. Journal of biomechanics 34(5): 623-9, 2001

[45] Howie DW, Holubowycz OT, Middleton R, Group LAS. Large femoral heads decrease the incidence of dislocation after total hip arthroplasty. J Bone Joint Surg Am 94(12): 1095-102, 2012

[46] Van Sikes C, Lai LP, Schreiber M, Mont MA, Jinnah RH, Seyler TM. Instability after total hip arthroplasty: Treatment with large femoral heads vs constrained liners. the Journal of Arthroplasty 23(7): 59-63, 2008

[47] Netter JD, Hermida JC, Chen PC, Nevelos JE, D'Lima DD. Effect of microseparation and third-body particles on dual-mobility crosslinked hip liner wear. The Journal of arthroplasty 29(9): 1849-53, 2014

[48] Lewinnek GE, Lewis JL, Tarr R, Compere CL, Zimmerman JR. Dislocations after total hip-replacement arthroplasties. Journal of Bone and Joint Surgery-American Volume 60(2): 217-20, 1978

[49] Hua X, Li J, Jin Z, Fisher J. The contact mechanics and occurrence of edge loading in modular metal-on-polyethylene total hip replacement during daily activities. Medical engineering & physics 38(6): 518-25, 2016

[50] Murray D. The definition and measurement of acetabular orientation. Bone & Joint Journal 75(2): 228-32, 1993

[51] Maratt JD, Esposito CI, McLawhorn AS, Jerabek SA, Padgett DE, Mayman DJ. Pelvic tilt in patients undergoing total hip arthroplasty: When does it matter? The Journal of arthroplasty 30(3): 387-91, 2015

[52] Pierrepont J, Hawdon G, Miles B, O’Connor B, Baré J, Walter L, Marel E, Solomon M, McMahon S, Shimmin A. Variation in functional pelvic tilt in patients undergoing total hip arthroplasty. Bone Joint J 99(2): 184-91, 2017

[53] Pierrepont JW, Stambouzou CZ, Miles BP, O'Connor PB, Walter L, Ellis A, Molnar R, Baré JV, Solomon M, McMahon S. Patient specific component alignment in total hip arthroplasty. Reconstructive Review 6(4), 2016

[54] Chan FW, Bobyn JD, Medley JB, Krygier JJ, Tanzer M. The otto aufranc award - wear and lubrication of metal-on-metal hip implants. Clinical Orthopaedics and Related Research (369): 10-24, 1999

[55] Liu F, Jin ZM, Hirt F, Rieker C, Roberts P, Grigoris P. Effect of wear of bearing surfaces on elastohydrodynamic lubrication of metal-on-metal hip implants. Proceedings of the Institution of Mechanical Engineers Part H-Journal of Engineering in Medicine 219(H5): 319-28, 2005

[56] Langton D, Sprowson A, Joyce T, Reed M, Carluke I, Partington P, Nargol A. Blood metal ion concentrations after hip resurfacing arthroplasty. Bone & Joint Journal 91(10): 1287-95, 2009

[57] Yoon JP, Le Duff MJ, Johnson AJ, Takamura KM, Ebramzadeh E, Amstutz HC. Contact patch to rim distance predicts metal ion levels in hip resurfacing. Clinical Orthopaedics and Related Research® 471(5): 1615-21, 2013

[58] Amstutz HC, Le Duff MJ. Hip resurfacing: History, current status, and future. Hip International 25(4), 2015

[59] Bergmann G, Deuretzbacher G, Heller M, Graichen F, Rohlmann A, Strauss J, Duda G. Hip contact forces and gait patterns from routine activities. Journal of biomechanics 34(7): 859-71, 2001

[60] Lombardi AV, Mallory TH, Dennis DA, Komistek RD, Fada RA, Northcut EJ. An in vivo determination of total hip arthroplasty pistoning during activity. The Journal of Arthroplasty 15(6): 702-9, 2000

[61] Glaser D, Dennis DA, Komistek RD, Miner TM. In vivo comparison of hip mechanics for minimally invasive versus traditional total hip arthroplasty. Clinical Biomechanics 23(2): 127-34, 2008

[62] Nevelos J, Ingham E, Doyle C, Streicher R, Nevelos A, Walter W, Fisher J. Microseparation of the centers of alumina-alumina artificial hip joints during simulator testing produces clinically relevant wear rates and patterns. The Journal of arthroplasty 15(6): 793-5, 2000

[63] Al-Hajjar M, Leslie IJ, Tipper J, Williams S, Fisher J, Jennings LM. Effect of cup inclination angle during microseparation and rim loading on the wear of biolox® delta ceramic-on-ceramic total hip replacement. Journal of Biomedical Materials Research Part B: Applied Biomaterials 95(2): 263-8, 2010

[64] Stewart T, Tipper J, Streicher R, Ingham E, Fisher J. Long-term wear of hiped alumina on alumina bearings for thr under microseparation conditions. Journal of Materials Science: Materials in Medicine 12(10): 1053-6, 2001

[65] Stewart TD, Tipper JL, Insley G, Streicher RM, Ingham E, Fisher J. Long-term wear of ceramic matrix composite materials for hip prostheses under severe swing phase microseparation. Journal of Biomedical Materials Research Part B: Applied Biomaterials 66(2): 567-73, 2003

[66] Al-Hajjar M. Wear of hard-on-hard hip prostheses: Influence of head size, surgical position, material and function: University of Leeds, 2012

[67] Sariali E, Stewart T, Jin Z, Fisher J. Three-dimensional modeling of in vitro hip kinematics under micro-separation regime for ceramic on ceramic total hip prosthesis: An analysis of vibration and noise. Journal of biomechanics 43(2): 326-33, 2010
[68] Singh SP, Urooj S. Wavelets: Biomedical applications. International Journal of Biomedical Engineering and Technology 19(1): 1-25, 2015
[69] Misiti M, Misiti Y, Oppenheim G, Poggi J-M. Wavelets and their applications: John Wiley & Sons, 2013
[70] Mallat S. A wavelet tour of signal processing: The sparse way: Academic press, 2008
[71] Nalband S, Sundar A, Prince AA, Agarwal A. Feature selection and classification methodology for the detection of knee-joint disorders. Computer methods and programs in biomedicine 127: 94-104, 2016
[72] Markwardt K. Wavelet analysis and frequency band decompositions. 2006
[73] Misiti M, Misiti Y, Oppenheim G, Poggi J-M. Wavelet toolbox-user's guide r2013b. MATLAB version 7, 2014
[74] Rajagopalan V, Ray A. Symbolic time series analysis via wavelet-based partitioning. Signal Processing 86(11): 3309-20, 2006
[75] Parameswariah C, Cox M. Frequency characteristics of wavelets. IEEE Transactions on Power Delivery 17(3): 800-4, 2002
[76] Neumann DA. Kinesiology of the musculoskeletal system-e-book: Foundations for rehabilitation: Elsevier Health Sciences, 2013
[77] Komistek RD, Dennis DA, Ochoa JA, Haas BD, Hammill C. In vivo comparison of hip separation after metal-on-metal or metal-on-polyethylene total hip arthroplasty. J Bone Joint Surg Am 84(10): 1836-41, 2002
[78] Barba D, Barker L, Chhabra A. Anatomy and biomechanics of the posterior cruciate ligament and posterolateral corner. Operative Techniques in Sports Medicine 23(4): 256-68, 2015
[79] William J. Long JBJ, Michael P. Nett, Gregory J. Roehrig, Giles R. Scuderi, W. Norman Scott. Posterior cruciate ligament—substituting total knee arthroplasty. In: Scott WN, ed. Insall & scott surgery of the knee. Philadelphia, PA: Elsevier. 1529-44. 2018
[80] Aaron A. Hofmann BPD. Posterior cruciate sacrificing total knee arthroplasty. In: Scott WN, ed. Insall & scott surgery of the knee. Philadelphia, PA: Elsevier. 1526-8. 2018
[81] Banks SA, Markovich GD, Hodge WA. In vivo kinematics of cruciate-retaining and-substituting knee arthroplasties. The Journal of arthroplasty 12(3): 297-304, 1997
[82] Nakayama K, Matsuda S, Miura H, Higaki H, Otsuka K, Iwamoto Y. Contact stress at the post-cam mechanism in posterior-stabilised total knee arthroplasty. Bone & Joint Journal 87(4): 483-8, 2005

[83] Suggs JF, Hanson GR, Park SE, Moynihan AL, Li G. Patient function after a posterior stabilizing total knee arthroplasty: Cam–post engagement and knee kinematics. Knee Surgery, Sports Traumatology, Arthroscopy 16(3): 290-6, 2008

[84] Catani F, Innocenti B, Belvedere C, Labey L, Ensini A, Leardini A. The mark coventry award articular: Contact estimation in tka using in vivo kinematics and finite element analysis. Clinical Orthopaedics and Related Research® 468(1): 19-28, 2010

[85] Shimizu N, Tomita T, Yamazaki T, Yoshikawa H, Sugamoto K. The effect of weight-bearing condition on kinematics of a high-flexion, posterior-stabilized knee prosthesis. The Journal of arthroplasty 26(7): 1031-7, 2011

[86] Fitzpatrick CK, Clary CW, Cyr AJ, Maletsky LP, Rullkoetter PJ. Mechanics of post-cam engagement during simulated dynamic activity. Journal of Orthopaedic Research 31(9): 1438-46, 2013

[87] Nakamura S, Sharma A, Nakamura K, Ikeda N, Zingde SM, Komistek RD. Can post-cam function be replaced by addition of a third condyle in ps tka? The Journal of arthroplasty 29(9): 1871-6, 2014

[88] Zingde SM, Leszko F, Sharma A, Mahfouz MR, Komistek RD, Dennis DA. In vivo determination of cam-post engagement in fixed and mobile-bearing tka. Clinical Orthopaedics and Related Research® 472(1): 254-62, 2014

[89] Arnout N, Vanlommel L, Vanlommel J, Luyckx J, Labey L, Innocenti B, Victor J, Bellemans J. Post-cam mechanics and tibiofemoral kinematics: A dynamic in vitro analysis of eight posterior-stabilized total knee designs. Knee Surgery, Sports Traumatology, Arthroscopy 23(11): 3343-53, 2015

[90] Mahfouz MR, Hoff WA, Komistek RD, Dennis DA. A robust method for registration of three-dimensional knee implant models to two-dimensional fluoroscopy images. IEEE transactions on medical imaging 22(12): 1561-74, 2003

[91] Cai SX, Wu YF, Xiang N, Zhong ZT, He J, Shi L, Xu F, Ieee. Detrending knee joint vibration signals with a cascade moving average filter. In: 34th Annual International Conference of the IEEE Engineering-in-Medicine-and-Biology-Society (EMBS). San Diego, CA. 4357-60. 2012

[92] Yang S, Cai S, Zheng F, Wu Y, Liu K, Wu M, Zou Q, Chen J. Representation of fluctuation features in pathological knee joint vibroarthrographic signals using kernel density modeling method. Medical engineering & physics 36(10): 1305-11, 2014

[93] Hjorth B. Eeg analysis based on time domain properties. Electroencephalography and clinical neurophysiology 29(3): 306-10, 1970

[94] Hjorth B. The physical significance of time domain descriptors in eeg analysis. Electroencephalography and clinical neurophysiology 34(3): 321-5, 1973

[95] Watanabe T, Koga H, Horie M, Katagiri H, Sekiya I, Muneta T. Post-cam design and contact stress on tibial posts in posterior-stabilized total knee prostheses: Comparison between a rounded and a squared design. The Journal of Arthroplasty 32(12): 3757-62, 2017

[96] Clary CW, Fitzpatrick CK, Maletsky LP, Rullkoetter PJ. The influence of total knee arthroplasty geometry on mid-flexion stability: An experimental and finite element study. Journal of biomechanics 46(7): 1351-7, 2013

[97] Deshpande BR, Katz JN, Solomon DH, Yelin EH, Hunter DJ, Messier SP, Suter LG, Losina E. Number of persons with symptomatic knee osteoarthritis in the us: Impact of race and ethnicity, age, sex, and obesity. Arthritis care & research 68(12): 1743-50, 2016

[98] Hunter DJ. Viscosupplementation for osteoarthritis of the knee. New England Journal of Medicine 372(11): 1040-7, 2015

[99] Bowman EN, Hallock JD, Throckmorton TW, Azar FM. Hyaluronic acid injections for osteoarthritis of the knee: Predictors of successful treatment. International orthopaedics: 1-8, 2018

[100] Burdick JA, Prestwich GD. Hyaluronic acid hydrogels for biomedical applications. Advanced Materials 23(12): H41-H56, 2011

[101] Strauss EJ, Hart JA, Miller MD, Altman RD, Rosen JE. Hyaluronic acid viscosupplementation and osteoarthritis: Current uses and future directions. American Journal of Sports Medicine 37(8): 1636-44, 2009

[102] OrthoInfo. Diseases & conditions: Arthritis of the knee. AAOS. 2014. https://orthoinfo.aaos.org/en/diseases--conditions/arthritis-of-the-knee/

[103] Altman RD, Bedi A, Karlsson J, Sancheti P, Schemitsch E. Product differences in intra-articular hyaluronic acids for osteoarthritis of the knee. American Journal of Sports Medicine 44(8): 2158-65, 2016

[104] Bannuru RR, Natov NS, Obadan IE, Price LL, Schmid CH, McAlindon TE. Therapeutic trajectory of hyaluronic acid versus corticosteroids in the treatment of knee osteoarthritis: A systematic review and meta-analysis. Arthritis & Rheumatism-Arthritis Care & Research 61(12): 1704-11, 2009

[105] Hatoum HT, Fierlinger AL, Lin S-J, Altman RD. Cost-effectiveness analysis of intra-articular injections of a high molecular weight bioengineered hyaluronic acid for the treatment of osteoarthritis knee pain. Journal of medical economics 17(5): 326-37, 2014

[106] Bannuru R, Natov N, Dasi U, Schmid C, McAlindon T. Therapeutic trajectory following intra-articular hyaluronic acid injection in knee osteoarthritis–meta-analysis. Osteoarthritis and cartilage 19(6): 611-9, 2011

[107] Rutjes AW, Jüni P, da Costa BR, Trelle S, Nüesch E, Reichenbach S. Viscosupplementation for osteoarthritis of the knee: A systematic review and meta-analysis. Annals of internal medicine 157(3): 180-91, 2012

[108] Jevsevar DS, Brown GA, Jones DL, Matzkin EG, Manner PA, Mooar P, Schousboe JT, Stovitz S, Sanders JO, Bozic KJ. The american academy of

orthopaedic surgeons evidence-based guideline on: Treatment of osteoarthritis of the knee. JBJS 95(20): 1885-6, 2013

[109] McAlindon TE, Bannuru RR, Sullivan M, Arden N, Berenbaum F, Bierma-Zeinstra S, Hawker G, Henrotin Y, Hunter D, Kawaguchi H. Oarsi guidelines for the non-surgical management of knee osteoarthritis. Osteoarthritis and cartilage 22(3): 363-88, 2014

[110] Weick JW, Bawa HS, Dirschl DR. Hyaluronic acid injections for treatment of advanced osteoarthritis of the knee: Utilization and cost in a national population sample. JBJS 98(17): 1429-35, 2016

[111] Schmajuk G, Bozic KJ, Yazdany J. Using medicare data to understand low-value health care: The case of intra-articular hyaluronic acid injections. JAMA internal medicine 174(10): 1702-4, 2014

[112] Wu YF, Cai SX, Yang SS, Zheng F, Xiang N. Classification of knee joint vibration signals using bivariate feature distribution estimation and maximal posterior probability decision criterion. Entropy 15(4): 1375-87, 2013

[113] Willison R. Analysis of electrical activity in healthy and dystrophic muscle in man. Journal of neurology, neurosurgery, and psychiatry 27(5): 386, 1964

[114] Cai SX, Yang SS, Zheng F, Lu M, Wu YF, Krishnan S. Knee joint vibration signal analysis with matching pursuit decomposition and dynamic weighted classifier fusion. Computational and Mathematical Methods in Medicine, 2013

[115] Wu Y, Krishnan S. Combining least-squares support vector machines for classification of biomedical signals: A case study with knee-joint vibroarthrographic signals. Journal of Experimental & Theoretical Artificial Intelligence 23(1): 63-77, 2011

[116] Wu Y, Chen P, Luo X, Huang H, Liao L, Yao Y, Wu M, Rangayyan RM. Quantification of knee vibroarthrographic signal irregularity associated with patellofemoral joint cartilage pathology based on entropy and envelope amplitude measures. Computer methods and programs in biomedicine 130: 1-12, 2016

VITA

Trevor Ferdinand Grieco was born in 1990 in Whitestone, New York. He moved to Knoxville, Tennessee in 1996 and grew up playing soccer and piano with three brothers. Sprains, breaks, and tears found Trevor in the orthopaedic clinic often and gave him a unique appreciation for the musculoskeletal system. This led Trevor to pursue a biomedical engineering degree at the University of Tennessee. At the start of his third year, Trevor started working as an undergraduate research assistant at the Center for Musculoskeletal Research (CMR). Trevor continued working at CMR in pursuit of his master's and doctoral degrees in mechanical engineering. During his graduate research Trevor led multiple in vivo investigations of joint replacement kinematics. This work has been published in various journals and presented at conferences internationally. Trevor was also invited to write a book chapter on patellofemoral kinematics for the Insall & Scott "Surgery of the Knee" textbook.

During his final year of undergraduate studies at the University of Tennessee, Trevor launched a software company aimed at serving physical therapy. Trevor pitched the company at multiple business plan competitions and was awarded grants for company development. Although the venture eventually folded, Trevor found a new passion in innovation and entrepreneurship. Since then Trevor has participated in medical device and digital health hackathons while closely following medical innovation. Today, Trevor lives in Houston, Texas and works as a biomedical engineer in the clinical trials industry. In his work Trevor continues to pursue his passions in orthopaedics and medical innovation through evaluation of treatments undergoing clinical trials and post market research.